

## ABSTRACT

Title of dissertation:                    **BROADBAND PHOTODETECTION IN GRAPHENE**

Xinghan Cai, Doctor of Philosophy, 2015

Dissertation directed by:            Professor, Michael S. Fuhrer,  
Department of Physics

Graphene, a single-atom-thick plane of carbon, has unique optoelectronic properties that result in a variety of potential photonic applications, such as optical modulators, plasmonic devices and THz emitters. In this thesis, the light-matter interaction in monolayer graphene and the subsequent photoexcited charge carrier transport are studied, and it is found that graphene has unique advantages for hot-electron photothermoelectric detection. Particularly promising is detection of terahertz (THz) radiation, in which graphene devices may offer significant advantages over existing technology in terms of speed and sensitivity.

By using a tilted angle shadow evaporation technique, bi-metal contacted graphene photodetectors are realized experimentally. Efficient photodetection via the hot-electron photothermoelectric effect is demonstrated at room temperature across a broad frequency range (THz to near infrared). For THz detection, the best device shows sensitivity exceeding 10 V/W (700 V/W) and noise equivalent power less than 1100 pW/Hz<sup>1/2</sup> (20 pW/Hz<sup>1/2</sup>), referenced to the incident (absorbed) power, implying

a performance competitive with the best room-temperature THz detectors for an optimally absorbing device, while time-resolved measurements indicate that the graphene detector is eight to nine orders of magnitude faster than those.

To increase the absorption and quantum efficiency, large area epitaxial graphene micro-ribbon array photodetectors are designed for resonant plasmon excitation in the THz range. By tailoring the orientation of the graphene ribbons with respect to an array of sub-wavelength bimetallic electrodes, a condition is achieved in which the plasmonic mode can be efficiently excited by an incident wave polarized perpendicular to the electrode array. The sensitivity of the detector is enhanced when the plasmon resonance frequency, which is tunable by adjusting the gate voltage, matches with the frequency of the incident radiation.

BROADBAND PHOTODETECTION IN GRAPHENE

By

Xinghan Cai

Dissertation submitted to the Faculty of the Graduate School of the  
University of Maryland, College Park, in partial fulfillment  
of the requirements for the degree of  
Doctor of Philosophy  
2015

Advisory Committee:  
Professor Michael S. Fuhrer, Chair  
Professor H. Dennis Drew  
Professor Thomas E. Murphy  
Associate Professor Min Ouyang  
Assistant Professor Jay Deep Sau

© Copyright by  
Xinghan Cai  
2015

## Dedication

To my parents Renxiang Cai (蔡仁祥), Shicui Gong (龚世翠)

## Acknowledgements

First and foremost, I would like to express my deepest gratitude to my advisor, Prof. Michael S. Fuhrer, who has been always supportive, attentive, kind and patient to me since I joined his group five years ago. Dr. Fuhrer is a very insightful scientist with comprehensive knowledge in condensed matter physics and is always open to discussing with people to share his ideas. I recall every time when I entered his office with difficulties in the project, Dr. Fuhrer would put aside his work and talk to me. He always quickly penetrated the key point of the issue and provided useful suggestions, guiding me to the correct direction. I also learnt from Dr. Fuhrer how to write academic papers with succinct language and conformed style, how to prepare nice Power Point slides for presentations, and how to effectively express the ideas to people. In a word, it is Dr. Fuhrer who enlightened me on the research of two dimensional materials, motivated and encouraged me when I faced difficulties in my Ph.D. studies. I am greatly indebted to him for giving me the opportunity working with him and I could not ask for better guidance.

I would like to express my sincere gratitude to Prof. Dennis Drew, from whom I learnt most of my knowledge of optics, especially THz technologies and plasmonic properties of metallic and semi-metallic systems. Dr. Drew is a prime example of being hardworking and rigorous. He is always open to talk and answer my questions. If an issue is not solved immediately, Dr. Drew would continue to work afterwards and get me back as soon as possible. Sometimes he sent me emails late at night to show detailed explanation to the issue discussed earlier that day. In addition, I admire that Prof. Drew gives me the greatest freedom to use the facilities in his lab, without which I will never be able to complete my Ph. D. studies.

I would like to thank Prof. Thomas Murphy, the perfect leader of the graphene photonics project. He organizes most of the meetings for a big group consisting of

researchers from four different institutions. I also benefited a lot from his hacking of the text I wrote (and the much higher quality text he put in) when we were co-authoring papers. I also would like to thank the other members of my dissertation committee, Prof. Jay Deep Sau and Prof. Min Ouyang, for their guidance that leads to the completion of this thesis.

When organizing my past works in Ph. D. study, I cannot stop to recall my growing up and my journey to the academic world. I feel to be very grateful to my parents who give me life and bring me up. They taught me how to become an honest and diligent person. I inherited from them the ability of rational thinking. Without their support, I will not be able to study abroad and finish my Ph. D. work. I also would like to thank my girlfriend, Qing Lu, a girl I met ten years ago. Similar to me, she is a researcher working in the scientific world. She is always patient to me and understands me very well. She encouraged me and made me feel better every time when my experiment did not go well. It would be hard for me to overcome many difficulties without her.

I would like to extend my gratitude to my collaborators and friends. Thanks to Dr. Kurt Gaskill for providing me high quality samples and offering me opportunities to take part in academic activities. Thanks to Dr. Andrei Sushkov for spending a lot of time to assist me in performing the far infrared experiments, even on Christmas Eve. Thanks to Ryan Suess for performing the intense measurements with me when we have a deadline to respond to referees. Thanks to Prof. Jun Yan for teaching me a lot of theoretical knowledge and experimental skills when I just started with research on graphene optoelectronics. Thanks to Dr. Wenzhong Bao, who invited me to join many interesting projects and always shared useful information with me. Thanks to Dr. Yilin Wang for many useful discussions. Thanks to Prof. Steve Anlage and Dr. Behnood Ghamsari for the assistance in experiments. Thanks to Liang Li for being not only a good colleague, but a trustworthy roommate as well. Thanks to

Mohammad Jadidi, Dr. Gregory Jenkins, Prof. Luke Nyakiti, Rachael Myers-Ward and Shanshan Li for co-authoring papers. I apologize that my acknowledgement to the rest of the people will be unfairly shortened, in order to be able to finish my thesis on time. I would like to thank Fuhrer group members, including Dr. William Cullen, Dr. Jianhao Chen, Dr. Shudong Xiao, Dr. Dohun Kim, Dr. Chaun Jang, Dr. Mahito Yamamoto, Dr. Alexandra Curtin, Dr. Kristen Burson, Dr. Michelle Zimmermann, Dr. Claudia Ojeda, Dr. Enrique Cobas, Dr. SungJae Cho, Dr. Jinglei Ping, Jacob Tosado and Jack Hellerstedt.

Last but not least, I am grateful to my friends Tengfei Miao, Kai He, Xiang Gao, Da Huang and Tung-Chung Liu, who, like me, are doing research now in United States. Life is like a fight. I would say that with you together, I do not feel alone and will continue on my way to the future.

2015.02.20

Xinghan Cai



# Table of Contents

List of Tables .....	ix
List of Figures .....	x
Chapter 1 Introduction .....	1
1.1 Introduction to photodetectors .....	1
1.1.1 The electromagnetic spectrum .....	1
1.1.2 Photodetection .....	3
1.2 Introduction to graphene .....	7
1.2.1 The band structure of graphene .....	8
1.2.2 Charge scattering in graphene .....	11
1.2.3 Electron-electron interaction in graphene .....	14
Chapter 2 Light-matter interaction in graphene .....	18
2.1 Light absorption in graphene .....	18
2.1.1 Optical absorption due to interband transitions .....	19
2.1.2 Optical absorption due to intraband transitions .....	22
2.2 Plasmon excitation in finite-sized graphene .....	26
2.3 Photo detection mechanisms in graphene .....	30
2.3.1 Photovoltaic effect .....	30
2.3.2 Hot electron photothermoelectric effect .....	32
2.3.3 Bolometric effect .....	36
Chapter 3 Experimental techniques .....	39
3.1 Graphene photodetector fabrication .....	39
3.1.1 Preparation and characterization of monolayer graphene .....	39
3.1.2 Photodetector fabrication – shadow evaporation technique .....	43
3.2 Transport measurement set-up .....	48
3.3 DC photoresponse measurement set-up .....	50
3.4 Time-domain photoresponse measurement set-up .....	51
3.4.1 Experimental set-up for pulse coincidence measurement .....	52
3.4.2 Broadband direct-time-domain-readout photoresponse measurement set-up .....	53
3.5 Scanning photocurrent measurement set-up .....	55
3.6 Fourier transform infrared spectroscopy set-up .....	56
Chapter 4 Broadband photoresponse characterization of bi-metal contacted graphene photodetectors (CW excitation) .....	59
4.1 Scanning photocurrent measurement .....	59

3.6 Fourier transform infrared spectroscopy set-up .....	56
Chapter 4 Broadband photoresponse characterization of bi-metal contacted graphene photodetectors (CW excitation) .....	59
4.1 Scanning photocurrent measurement .....	59
4.2 Broadband room-temperature photothermoelectric response .....	63
4.2.1 Thermoelectric effect in graphene contacted with dissimilar metals .....	63
4.2.2 Broadband room-temperature photodetection .....	67
4.2.3 Power dependence of the thermoelectric response .....	70
4.3 Noise-equivalent power of the graphene photodetector .....	72
4.3.1 Incident power and absorbed power .....	72
4.3.2 Noise source and NEP measurement .....	76
4.4 Photothermoelectric model for a diffusive device .....	80
4.5 Discussion and conclusion .....	85
4.5.1 Improving device performance .....	85
4.5.2 Summary and conclusion .....	86
Chapter 5 Response of graphene photodetectors to pulsed laser excitations .....	88
5.1 Response time in optical and THz range .....	89
5.1.1 Time domain characterization for optical excitations .....	89
5.1.2 Time domain characterization for THz excitations .....	90
5.2 Intrinsic response time characterization .....	94
5.3 Conclusion .....	99
Chapter 6 Photoresponse to near-IR pulsed laser: further study and contact effects .....	102
6.1 Gate dependent pump-probe measurement .....	102
6.2 Power dependent dc photoresponse to pulsed laser excitation .....	104
6.3 Temperature dependent dc photoresponse to pulsed laser excitation .....	105
6.4 Decoupling of the linear and nonlinear signals .....	108
6.5 Conclusion .....	111
Chapter 7 Plasmon-enhanced THz detection in graphene .....	112
7.1 Plasmon mode in a graphene microribbon array .....	113
7.2 Drude response and standing wave plasmons in graphene-metal microstructures .....	119
7.3 Transmission of graphene ribbon array tilted to metal electrodes .....	123
7.3.1 Device with large electrode spacing .....	123
7.3.2 Device with small electrode spacing .....	126
7.4 Plasmon enhanced THz photoresponse .....	130
7.5 Conclusion and outlook .....	132
Chapter 8 Conclusion and outlook .....	137

8.1 Conclusion .....	137
8.2 Future outlook .....	139
Appendix A .....	145
Appendix B .....	147
Bibliography .....	150

## List of Tables

<b>Table 5.1</b> Comparison of the characteristics between our device and commercially available room-temperature THz detectors.....	
<b>Table 5.2</b> Comparison of the characteristics between our device and other high speed THz detectors.....	
<b>Table A.1</b> Bi-metal contacted exfoliated graphene photodetector fabrication process..	
<b>Table A.2</b> Bi-metal contacted large graphene photodetector fabrication process.....	

## List of Figures

- Figure 1.1** Electromagnetic spectrum with visible light highlighted. ....
- Figure 1.2** Schematic of a Golay cell. Figure from Ref. [13] .....
- Figure 1.3** (a) Honeycomb lattice of monolayer graphene consisting of  $A$ ,  $B$  sublattices. (b) Brillouin zone of graphene in momentum space.  $\mathbf{K}$  and  $\mathbf{K}'$  are Dirac points. Figure from Ref. [28] .....
- Figure 1.4** (a) Graphene band structure. (b) Band diagram close to the  $\mathbf{K}$  and  $\mathbf{K}'$  points showing the Dirac cones. Figure adapted from Ref. [29, 31] .....
- Figure 1.5** Residual resistivity (solid lines), LA phonon resistivity (blue and red dots from two samples, brown dotted line based on Eqn. (1.6)), and SiO<sub>2</sub> remote interfacial phonon resistivity (black, red and blue dashed lines from three samples, and green dashed line based on (Eqn. 1.8)) as a function of gate voltages. Figure adapted from Ref. [32] .....
- Figure 1.6** Spectrally integrated differential transmission as a function of pump-probe delay: experiment (open circles) and numerical fit (solid line). Dash-dotted line: Cross correlation of pump and probe pulses. Inset: Linear dependence of the maximum transmission change on the absorbed pump fluence. Figure from Ref. [44].
- Figure 1.7** (a) Experimental observation of carrier dynamics. (b) Time-resolved carrier dynamics for two different photon energies. Insets show a schematic representation of the carrier distribution as a function of the time. (c) Scaling of the differential transmission signal peak values for six photon energies as a function of absorbed photon density. (d) A schematic illustrating the impact ionization induced carrier multiplication for two different photon energies. Figure from Ref. [49] .....
- Figure 2.1** (A) Photograph of a 50- $\mu\text{m}$  aperture partially covered by graphene and its bilayer. The line scan profile shows the intensity of transmitted white light along the yellow line. (B) Transmittance spectrum of monolayer graphene (open circles) and theoretical prediction (red line) and correction (green line). (Inset) Transmittance of white light as a function of the number of graphene layers. Figure from Ref. [56] .....
- Figure 2.2** (a) An illustration of Pauli blocking in hole-doped graphene. (b) The gate-induced change of transmission in hole-doped graphene as a function of the photon energy of the incident radiation. The values of the gate voltage referenced to that for charge neutrality, for the curves -0.75, -1.75, -2.75 and -3.5V, from left to right. Figure from Ref. [59] .....
- Figure 2.3** Change in the optical sheet conductivity of graphene in the infrared range induced by electrostatic doping. Figure from Ref. [61] .....
- Figure 2.4** Real part of the infrared conductivity including the effect of phonons, unitary scatterers and charged impurities. Solid lines: Theoretical curves. Dashed lines: Experimental data. Blue dotted lines show the boundaries (for the spectrum at  $V_g = 71$  V) between Drude response (I), Pauli blocking (II) and the interband transition (III) dominant ranges. Figure adapted from Ref. [63] .....
- Figure 2.5** Schematic of a piece of graphene flake with pancake geometry ( $d = 2a$ ,  $h = 2c$ ) and dielectric constant  $\xi^i$ . The environment dielectric constant is  $\xi^e$ . .....
- Figure 2.6** Schematic shown the real part of the ac conductivity as a function of the frequency for a Drude response (black line) and a plasmon response (Red line) .....

**Figure 2.7** (a) Optical image of a graphene device. (b) Four-probe resistance of the device. (c) Combined light reflection and photo-current image ( $I_{\text{CFA}}$ ). (d) Schematic of the photocurrent generation in the device. Figure from Ref. [76].....

**Figure 2.8** Schematic of the Seebeck effect in a uniform metal bar. ....

**Figure 2.9** Monolayer graphene's Seebeck coefficient as a function of the gate voltage at different temperatures. The curves cross at the charge neutral point. Figure from Ref. [87] .....

**Figure 2.10** (a) Schematic of a dual-gated bilayer graphene device and electric-field-effect gating. (b) Optical (blue) and electrical (red) responses as a function of dc current at  $T = 5.16\text{K}$ . Figure from Ref. [94] .....

**Figure 3.1** (a) Optical micrograph of an exfoliated graphene sample. (b) Raman spectrum of monolayer graphene. Inset: Lorentzian fit (red line) to the 2D peak (black line) of the Raman spectrum of monolayer graphene. ....

**Figure 3.2** (a) Optical micrograph of CVD-grown monolayer graphene on  $\text{SiO}_2$ . (b) Raman spectrum of CVD-grown monolayer graphene. ....

**Figure 3.3** (a) Raman spectrum of a monolayer epitaxial graphene on SiC. (b) Raman spectrum of the same device shown in (a) with the background response subtracted. Inset: Lorentzian fit to 2D peak. ....

**Figure 3.4** Optical micrograph of an exfoliated graphene photodetector device with three different metallic probes (Cr, Au and Au/Cr). ....

**Figure 3.5** (a-e) Lithographic steps of the shadow evaporation technique, as described in text. (f) Optical micrograph of the device. Inset: AFM image of the graphene flake contacted with dissimilar metal electrodes.....

**Figure 3.6** (a) A photodetector based on CVD-grown graphene on  $\text{SiO}_2$  substrate. (b) A photodetector based on epitaxial grown graphene on SiC substrate.....

**Figure 3.7** Schematic of the transport measurement set-up of a bi-metal contacted graphene photodetector on  $\text{SiO}_2/\text{Si}$  substrate.....

**Figure 3.8** Experimental set-up for broadband dc photoresponse characterization.....

**Figure 3.9** (a) Experimental set-up for the pulse coincidence measurement. (b) Schematic showing the power dependence of a linear (red dashed line) and a sublinear (blue solid line) response.....

**Figure 3.10** Experimental set-up for time-domain photoresponse characterization. ....

**Figure 3.11** Experimental set-up for scanning photocurrent measurement. ....

**Figure 3.12** (a) Experimental set-up of a FTIR system. (b) Photograph of two copper plate sample holders, one with a sample on top (left) and another used as reference (right). (c) Transmission spectrum of a  $\text{SiO}_2/\text{Si}$  substrate. ....

**Figure 4.1** (a) Optical micrograph of a bi-metal contacted graphene photodetector. (b) Reflectivity image of the device taken by the LSM system. ....

**Figure 4.2** (a) Zoomed-in reflectivity image of the device. (b) Two dimensional magnitude map of the photocurrent signal taken at  $V_g = 0\text{ V}$ . (c) The photocurrent signal as a function of gate voltage with the beam position fixed at four different points, numbered in (a) and (b). (d) Two dimensional phase map of the photocurrent signal taken at  $V_g = 0\text{ V}$  corresponding to (b). ....

**Figure 4.3** Two-probe electrical conductivity (a) and photocurrent with uniform illumination (b) as a function of the gate voltage. (c) The summation of signals shown in the black and red curve of Fig. 4.2c.....

**Figure 4.4** (a) Cross-sectional view of the device. (b-e) Profiles across the device of (b) electron temperature  $T(x)$ , (c) Fermi level  $E_F(x)$ , (d) Seebeck coefficient  $S(x)$  and (e) potential gradient  $\nabla V(x) = -S\nabla T(x)$ . The photoresponse is the integral of  $\nabla V(x)$  over the length of the device, or area under the curve in (e). .....

**Figure 4.5** The thermoelectric response measured using dc rectification (black dots) and ac second harmonics (red line) technique on another similar device.....

**Figure 4.6** Broadband thermoelectric responsivity of graphene photothermoelectric detector. (a,d) Electrical conductance, (b,e) responsivity to Joule heating, and (c,f) responsivity to radiation as a function of gate voltage for the device shown in Fig. 3.5f at room temperature and in ambient environment. Responsivity to Joule heating was measured at dc in (b) and at 15.7 Hz using the second harmonic technique in (e). Panel (c) shows responsivity to 119  $\mu\text{m}$  wavelength THz radiation and panel (f) shows response to 1.54  $\mu\text{m}$  infrared radiation. ....

**Figure 4.7** Power dependence of the thermoelectric signal to (a) Joule heating, (b) near infrared excitation, and (c) THz excitation at selected gate voltages. Gate dependent responsivity for different excitation powers are shown in (d) and (e) for Joule heating and near infrared excitation, respectively. ....

**Figure 4.8** Photovoltage as a function of distance measured as the far infrared laser is scanned across the device (black dots) and Gaussian fit to the experimental data (red curve). Inset: Optical micrograph of the device. The device active area (graphene flake) is between two metal electrodes. ....

**Figure 4.9** Schematic shown the propagation of a polarized near infrared radiation in a air-Graphene-SiO<sub>2</sub>-Si layered structure. ....

**Figure 4.10** Frequency dependent noise floor of a bi-metal contacted graphene photodetector.....

**Figure 4.11** Noise equivalent power of graphene photothermoelectric detector. (a) Responsivity to 119  $\mu\text{m}$  wavelength THz radiation, (b) measured noise (black dotted line) and calculated Johnson-Nyquist noise (red dotted line), and (c) measured noise equivalent power (NEP) as a function of gate voltage for the device shown in the inset of Fig. 4.8. The blue line corresponds to  $\text{NEP} = 16 \text{ pW/Hz}^{1/2}$ . NEP is plotted in log scale .....

**Figure 4.12** Schematic shown the asymmetrical Seebeck coefficient profile across the device due to (a) chemical potential pinning by the metal contacts and (b) extra contact resistance caused by addition scattering in graphene. ....

**Figure 4.13** Electrical conductance as a function of gate voltage (black curve) for the device shown in Fig. 3.5f. Red solid line is a fit to Eqn. (4.11). ....

**Figure 4.14** Simulated responsivity of graphene photothermoelectric detector. The assumed asymmetry of the device is (a) induced by the work function difference of Cr and Au and different chemical potential pinning near both contacts, (b) purely induced by an additional contact resistance near the Au electrode, (c) induced by the asymmetries shown in (a) and (b) together. (d) Measured responsivity of the device to 119  $\mu\text{m}$  wavelength THz radiation (replotted from Fig. 4.6c).....

**Figure 5.1** Time domain photoresponse to pulsed laser excitation at 800 nm wavelength recorded by a 40 GHz sampling oscilloscope for device fabricated on SiC (shown in Fig. 3.9). The FWHM is  $\sim 30$  ps. ....

**Figure 5.2** (a) Time domain photoresponse to pulsed THz excitation with different power intensities. 10 mV offset is added to each curve for clarity. (b) Peak response as a function of the absorbed power (blue dots) and a linear fit (red line). .....

**Figure 5.3** (a) Time domain photoresponse to pulsed THz excitation at different gate voltages. (b) Electrical resistance of the device as a function of the gate voltage. ....

**Figure 5.4** Differential response at  $V_g = -40$  V subtracted from the response at  $V_g = -20$  V (black curve) and  $V_g = 0$  V (Red curve). The FWHM is  $\sim 110$  ps. ....

**Figure 5.5** (a) Optical micrograph of the device for the pulse coincidence measurement. (b) Photoresponse from pump-probe laser pulses as a function of delay time at 150K. Red solid line shows a best fit assuming exponential decay of hot-electron temperature. ....

**Figure 6.1** (a) Two-probe conductance as a function of the gate voltage. (b) Photoresponse measured using the pulse-coincidence technique as a function of the delay time at different gate voltages. The temperature is fixed at  $T = 50$  K for both (a) and (b). ....

**Figure 6.2** Photovoltage excited by two near-IR pulsed excitations as a function of the gate voltages. At each gate voltage the photovoltage as a function of time delay is shown for a time-delay window of  $\pm 150$  ps. ....

**Figure 6.3** (a) Photovoltage as a function of the gate voltage to one pulsed near-IR excitation with different incident powers. (b) Photoresponse shown in (a) normalized by the incident power as a function of the gate voltage. ....

**Figure 6.4** (a) Photovoltage as a function of the gate voltage due to one pulsed near-IR excitation with different average incident powers as shown in legend. (b) Zoomed-in plot of (a) showing the response from  $V_g = 55$  V to  $V_g = 75$  V. ....

**Figure 6.5** (a) Photovoltage as a function of the gate voltage to one pulsed near-IR excitation at different temperatures. (b) Photovoltage as a function of the temperature to one pulsed near-IR excitation at different gate voltages. ....

**Figure 6.6** (a) Optical micrograph of a Cr (bottom) - Au (top) thermocouple device. (b) Photoresponse to a CW near-IR excitation as a function of the temperature. Data is shown for the beam focused on the gold pad (red line), the chromium pad (blue line), and the junction (black line). ....

**Figure 6.7** (a) Nonlinear component of the photovoltage as a function of the gate voltage to a pulsed near-IR excitation with different incident powers.  $T = 120 \pm 2$  K. (b) Linear component of the photovoltage as a function to the incident laser power (black dots) with a linear fits (red line). (c) Extrapolated  $\alpha$  at different gate voltages. ...

**Figure 6.8** Comparison between the nonlinear response extrapolated from the power dependence measurement at  $T \sim 120$  K (top) and the pump-probe response characterized at  $T \sim 50$  K (bottom). ....

**Figure 7.1** (a) Optical micrograph of a graphene ribbon array with no metal. The inset shows the corresponding schematics. Attenuation spectra at different gate voltages  $V_g$  are shown with incident electric field polarized vertical (b) and horizontal (c). Spectra are normalized by the spectrum at  $V_g = V_{g, min} + 2.2$  V (b) and  $V_g = V_{g, min}$  (c). ....

**Figure 7.2** Plasmonic resonance frequency  $f_p$  as a function of carrier density  $n$  for the device shown in Fig. 7.1. Black points are extracted from fits of the data in Fig. 7.1c



as described in text. Fits to data in Fig. 7.1c are shown as solid lines in inset. Red line: fit to Eqn. (7.3) in text.

**Figure 7.3** (a) Carrier density  $n$ , mobility  $\mu$ , and plasmonic resonance frequency  $f_p$  extracted from fits as a function of the gate voltage for the device shown in Fig. 7.1. (b, c, d) Plasmonic resonance frequency  $f_p$  as a function of carrier density  $n$  for the device shown in Fig. 7.1. Black points are extracted from fits of the data in Fig. 7.1c by assuming  $n_{\text{puddle}} = 0 \text{ cm}^{-2}$  (b),  $n_{\text{puddle}} = 0.75 \times 10^{12} \text{ cm}^{-2}$  (c) and  $n_{\text{puddle}} = 1.75 \times 10^{12} \text{ cm}^{-2}$  (d). Red line: fit to Eqn. (7.3) in text.

**Figure 7.4** (a) Optical micrograph of unpatterned graphene sheet on SiC substrate with metal grating on top. Inset: Schematic of the device. (b) Attenuation spectra at different gate voltages normalized by the spectrum at  $V_g = V_{g, \text{min}}$  with incident electric field polarized vertical.

**Figure 7.5** (a) Optical micrograph of a graphene ribbon array oriented orthogonal to a metal electrode grating. The inset shows the corresponding schematics. Attenuation spectra at different gate voltages  $V_g$  are shown with incident electric field polarized vertical (b) and horizontal (c). Spectra are normalized by the spectrum at  $V_g = V_{g, \text{min}}$ .

**Figure 7.6** (a) Optical micrograph of a graphene ribbon array tilted to a metal electrode grating. Inset: Schematic of the device. (b) Attenuation spectra at different gate voltages normalized by the spectrum at  $V_g = V_{g, \text{min}}$  with incident electric field polarized vertical.

**Figure 7.7** The attenuation at  $V_g = V_{g, \text{min}} + 5.4 \text{ V}$  is shown as a function of the frequency (radial axis) and the incident polarization (azimuthal axis). Inset: A scanning electron micrograph of a similar device (left) and the schematic of the device with the defined polarized angle  $\theta$  of the incident light (right). Graphene ribbon is tilted  $45^\circ$  to the metal electrodes.

**Figure 7.8** Simulated charge density profile in the graphene/metal microstructure at the plasmon resonance frequency. The polarization of the incident plane-wave (7.4 THz) is perpendicular to the graphene ribbons in (a) and parallel in (b), corresponding to the points marked with red and blue “+” symbols in Fig. 7.7, respectively. The same color scale is used for both figures.

**Figure 7.9** The attenuation at different  $V_g$  normalized by the spectrum at  $V_{g, \text{min}}$  as a function of frequency shown for the incident polarized angle:  $\theta = 60^\circ$  (Drude response) (a),  $0^\circ$  (combined response) (b),  $-60^\circ$  (Plasmon response) (c). The right column shows schematics of the device and the polarization of the incident light for each measurement, respectively.

**Figure 7.10** (a) Experimental attenuation at  $V_g = V_{g, \text{min}} + 6.5 \text{ V}$  as a function of frequency (radial axis) and the incident polarization (azimuthal axis). (b) Simulated attenuation of the device shown in (a) using the model discussed in the text. The inset of (a) shows a schematic of the device and defines the polarization angle  $\theta$ .

**Figure 7.11** (a) Measured magnitude of the photovoltage for a tilted graphene ribbon array photodetector as a function of  $V_g$  (radial axis) and the incident polarization (azimuthal axis). The device is the same as in Fig. 7.10a and the frequency of the laser excitation is 5.3 THz ( $175 \text{ cm}^{-1}$ ). (b) Simulated photoresponse of the same device using the model discussed in the text.

**Figure 8.1** Zoomed-out (a) and zoomed-in (b) optical micrograph of a graphene  $pn$ -junction photodetector.

**Figure 8.2** (a) Atomic force micrograph of a graphene nanoribbon array device. (b) Conductance (black dotted line) and second harmonic responsivity (red dotted line) as a function of the gate voltage measured at  $T = 85.5$  K. ....

**Figure 8.3** Schematics of a graphene *pn*-junction device. (a) Side view of the device. The graphene flake is sandwiched between two boron nitride layers and connected to the metal electrodes through 1D side contacts. (b) Top view of the device. Yellow pads serve as the ground and the signal output. The green pad is connected to the top gate. The graphene flake is etched to a ribbon tilted to the electrodes. ....

# Chapter 1: Introduction

## *1.1 Introduction to photodetectors*

In this section, I will introduce the classification, properties and some applications of electromagnetic radiation. Then I will briefly review the history and development of the photodetector. By classifying photodetectors into two main categories (those based on photon effects and thermal effects) and understanding the working mechanism of each type of the detector, I argue that the current technology supports the high energy photon (visible and near IR) detection well, but lacks the capability of making sensitive and fast low energy photon detectors at room temperature, especially in THz range. Therefore, a fast room-temperature broadband photodetector, which operates with high responsivity in far-IR range, is urgently needed for filling this blank and for THz technology applications.

### 1.1.1 The electromagnetic spectrum

“Darkness cannot drive out darkness: only light can do that,” said Martin Luther King, Jr. Light emitted by the sun is essential to all living things in our planet since the onset of evolution, especially to human beings, since they not only sense and feel the light, but also take advantage of it to change their life.

From the perspective of physics, visible light is one member of the family of electromagnetic (EM) waves (visible light has wavelengths in the range from  $\sim 390$  nm to  $\sim 700$  nm), which can transmit in free space and some media. Electromagnetic radiation is classified by wavelength into radio, microwave, infrared, visible, ultraviolet, X-rays and gamma rays, as shown in Fig. 1.1. Electromagnetic radiation carries energy and the quantization of this energy gives electromagnetic radiation wave-particle duality: Each quantized portion of energy  $E = h\nu$  is carried by a

particle, the photon, where  $h = 6.63 \times 10^{-34} \text{ J} \cdot \text{s}$  is the Planck constant and  $\nu$  is the frequency of the wave. Roughly speaking, above the submillimeter wavelength range (frequencies below 0.3 THz or photon energies below 1.2 meV), the apparatus to detect and study EM waves typically relies on their wave-like aspects, such as antennas, waveguides etc., where the electric field (wave amplitude) is the quantity which is guided, manipulated, and ultimately detected. Whereas at higher frequencies (higher photon energies), the particle nature of EM waves is evident, leading to ray-optics techniques for treating their propagation, and detection mechanisms often involve the photon energy.

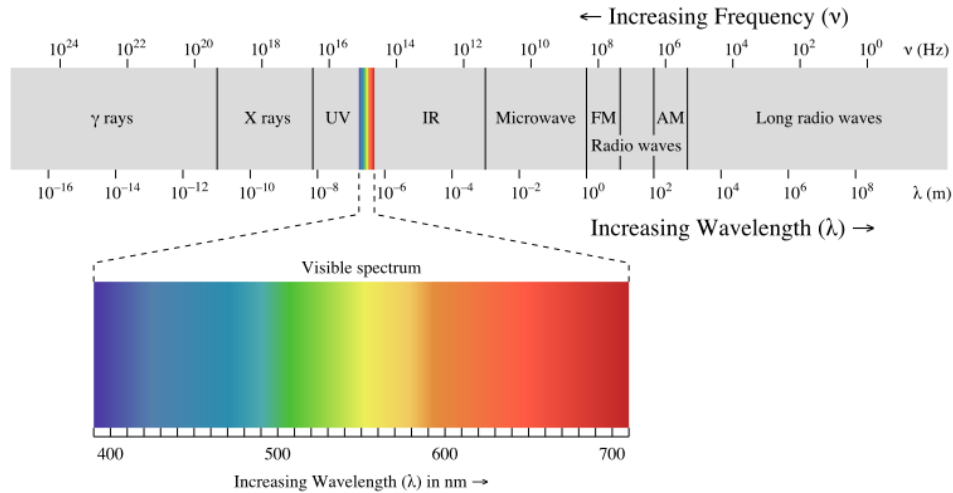


**Figure 1.1** Electromagnetic spectrum with visible light highlighted.

Electromagnetic radiation has applications across an enormous range of frequencies. As their wave nature dominates, radio waves (frequency up to 300 MHz) and microwaves (300 MHz – 300 GHz) are used mostly for antenna-coupled signal transmission and communication. For the range where the particle nature dominates, gamma rays (above 30 EHz) and X-rays (30 PHz – 30 EHz) are not commonly used in daily life, since their high energy photons can ionize atoms and are harmful to living tissues, however they have applications in medical imaging and radiation therapy. Visible light has a wide range of applications, since it is the only

electromagnetic wave that can be sensed by human eyes. Near infrared (30 THz – 300 THz) radiation is commonly used in fiber optic telecommunication because of low attenuation losses in silica medium.

Interesting to point out is the application of far infrared radiation, which is often called THz technology. The terahertz region of electromagnetic spectrum occupies a middle ground between microwave and infrared light waves, which makes it special and important in both physics research and technological applications. Terahertz technology has uses ranging from sensing to communications [1]. In biology and medicine, THz-TDS (terahertz time-domain spectroscopy) has been applied to study biomolecules [2] such as DNA, glucose and bacteria, with the ability to observe the intermolecular vibrations in some organic materials [3], which helps to study the dynamics of large biomolecules better than infrared spectroscopy. The distinct absorption spectra of different molecular species in the THz has inspired security applications, where THz technology helps to detect e.g. illegal drugs or explosives without opening the mail, box etc. [4] due to its ability to pass through many insulating materials. Although THz technology has a large potential market, it is still in its infant period, partly because there is a lack of powerful THz sources and highly efficient room-temperature THz detectors. [5]

### 1.1.2 Photodetection

The application of electromagnetic radiation generally requires three aspects of technology – its generation, transmission and detection. This thesis will mainly focus on the detection of the EM radiation covering a broad range from optical to far infrared and will especially pay attention to sensitive and fast room-temperature THz detection.

Photodetectors are sensors of electromagnetic energy. A natural example of photodetectors is the human eye retina, which is an array of optical detectors capable

of sensing photons. In practical applications, a photodetector usually transforms the radiation energy to an electrical signal, which can be quantitatively characterized or digitized. One example is the charge coupled devices (CCD) invented by Boyle and Smith [6] in 1970, which is usually a metal-oxide-semiconductor structure operating in the inversion mode. The photoactive region is a capacitor array based on an epitaxial layer of silicon. Charge coupled devices can collect and transfer localized charge carriers along the oxide-semiconductor surface. Once exposed to an image, each element of the capacitor array starts to transfer its charges to the neighbor. The last capacitor will put the charges into a charge amplifier, in order to generate a voltage signal for the following processing.

Traditional optical and infrared detectors can be classified into two main categories: Detectors based on photon effects and on thermal effects [7]. The photon effects are defined as a direct interaction between photons and electrons in the light sensitive material. A typical example is the photoconductive detector, in which the absorption of a photon with enough energy will promote an electron across the bandgap or out of a localized state into the conduction band, changing the electrical conductivity, and therefore generating a response when illuminated with light. Many semiconductors are photoconductive materials, such as silicon, germanium, GaAs, CdS and InAs. In these materials the electrical conductivity changes when the electron in the valence band absorbs an incident photon and transits to the conduction band, generating electron-hole pairs, which is called intrinsic photoconductivity [8]. Sometimes the photon energy is not high enough to induce an interband transition, but can ionize an impurity center that has the form of a free electron-bound hole (or free hole-bound electron). The conductivity change due to this process is called extrinsic photoconductivity [8, 9]. Compared to the photoconductive detector, another type of detector, which also requires electron-hole pair generation in the material, is more widely used, namely the photovoltaic detector, which will be discussed more in

detail in Chapter 2.3. The third type of photon effect used in photodetectors is the photoemissive effect. In this kind of device, electrons are emitted from the surface of the material (photocathode), when it is exposed to incident radiation. These electrons are then collected by the anode as an electrical signal output. Other photon effects include the Dember effect [9], Photon drag effect [10], etc. Detectors based on photon effects have been commercialized for years. A silicon photodetector can work at room-temperature with quite good sensitivity (responsivity  $\sim 1$  A/W) and fast speed (bandwidth  $> 1$  GHz) [11]. However, all photon effects are energy dependent and hence frequency dependent; in most cases, there is a threshold photon energy below which the detector does not work. For instance, in a photoconductive or photovoltaic detector, this photon energy corresponds to the band gap of the semiconductor. Therefore, most photodetectors in this category are limited to detect visible and near infrared radiation. Photodetectors based on photon effects also typically must operate at temperatures  $kT \ll h\nu$ , which limits room temperature operation to near infrared and higher energy photons.

Compared to detectors based on photon effects, thermal detectors have the advantage that they are applicable in low frequency (THz) photon detection, since thermal effects do not have a discrete energy cutoff. The generic working mechanism of a thermal detector is described as following: The incident radiation induce a temperature increase in the material. Subsequently, the material's properties change according to the temperature increase. The signal is generated via these property changes and is usually only related to the intensity (power) of the incident radiation, rather than electric field amplitude, or photon number (as in a photon effect detector). Commercially available THz photodetectors work mostly according to thermal effects. Commonly used thermal detectors involve the thermopile, the bolometer, the Golay cell and the pyroelectric detector. The thermopile is made based on the thermoelectric Seebeck effect of the material and the bolometer works according to the bolometric

effect. I will discuss these two effects in Chapter 2.3. The Golay cell [12] is a good IR detector, consisting of an absorber, a closed capsule of gas, a membrane and the optical read-out system, as shown in Fig. 1.2. The absorber gets heated when exposing to the incident radiation and results in an expansion of the encapsulated gas. The increased pressure induces the deformation of the membrane on which a mirror is mounted. The optical read-out system shines light to the mirror and the reflected beam is detected by a photodiode. The deflection of mirror will change the signal output from the photodiode and thus characterize the power of the IR radiation.

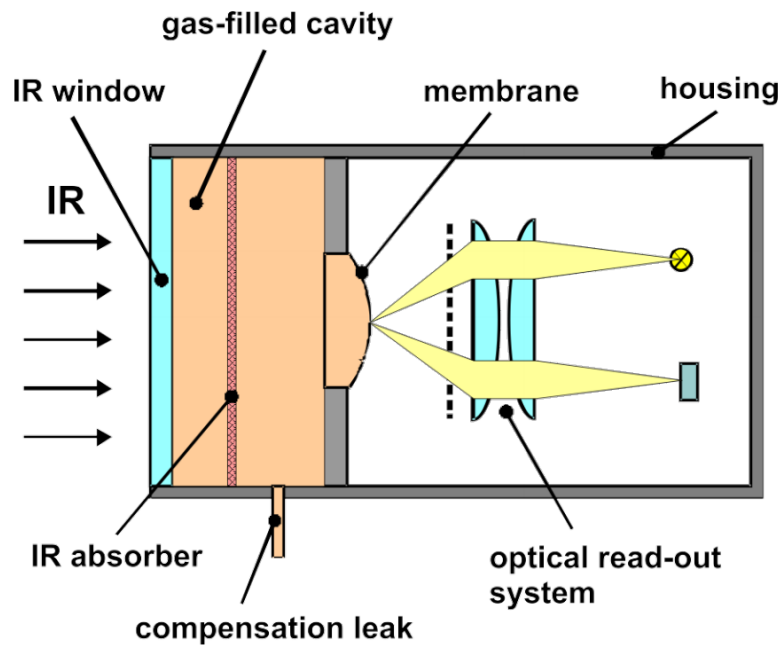


**Figure 1.2** Schematic of a Golay cell. Figure from Ref. [13]

A pyroelectric photodetector [14] employs the pyroelectric effect [15]: Certain materials slightly change their crystal structures by modifying the positions of the atoms when getting heated or cooled, which contributes to a temporary voltage if the polarizability of the material changes according to the structure change. The voltage will disappear due to the leaking current if the temperature gets stabilized at some value. However, if the incident radiation is chopped at some moderate frequency, the device can generate an alternating voltage output and thus be used for photo detection.



Golay Cell and pyroelectric detectors are nowadays widely used room-temperature photodetectors in the far infrared (THz) range. However, they only show a sensitivity to be  $\sim 10^{-8} \text{pW}/\sqrt{\text{Hz}}$  and bandwidth 10~100 Hz [16], which is neither sensitive enough for low power radiation detection, nor fast enough for high speed technology.

In recent years, great efforts have been made in searching for new materials for photon detection, and for new mechanisms to improve the sensitivity and speed of the detection. Some typical representatives are summarized here: The superconducting nanowire single-photon detector [17] and other cryogenic particle detectors [18], which operate at very low temperature; detectors based on nanostructured materials, such as colloidal quantum dots (CQD) and metal nanoparticles [19]; detectors based on small molecular weight organic thin-film [20]; detectors based on low dimensional materials, such as the carbon nanotube [21]; and room-temperature THz detectors based on semiconductor nanowire field-effect transistors [22], etc. These newly developed techniques and materials have improved the performance of the photodetector from different aspects. However, none of them realizes high sensitivity, ultrafast speed, broadband detection range and little dependence on the environment (vacuum, temperature and so on) at the same time.

## 1.2 Introduction to graphene

Graphene is a novel material, which consists of only one carbon atom layer. It can be thought of as a monolayer of graphite in which carbon atoms form a hexagonal lattice structure in a two dimensional (2D) plane. Its discovery in 2004 by Novoselov et al. [23] has surprised the scientific society since it was the first time to realize a freestanding 2D material experimentally. Graphene shows many novel properties, such as the exceptional charge carrier mobility [24], extremely high thermal conductivity [25], high intrinsic mechanical strength [26], and the strong interaction with incident photons [27]. In this section I will introduce the electrical properties of

graphene, including its band structure, the electron-phonon interaction, and the electron-electron interaction, which are closely related to the research of graphene optoelectronics when considering graphene as a choice of a photodetector.

### 1.2.1 The band structure of graphene

Graphene is unique since it consists of only one carbon atom layer and can be thus regarded as a perfectly two-dimensional electron gas system up to very high energies on order of the  $\pi$  to  $\sigma$  orbital energy difference (several eV). Fig. 1.3 shows graphene's lattice structure and the corresponding Brillouin zone. There are two triangular sublattices A and B in this honeycomb lattice structure with carbon-carbon spacing  $c_0 = 0.142$  nm.

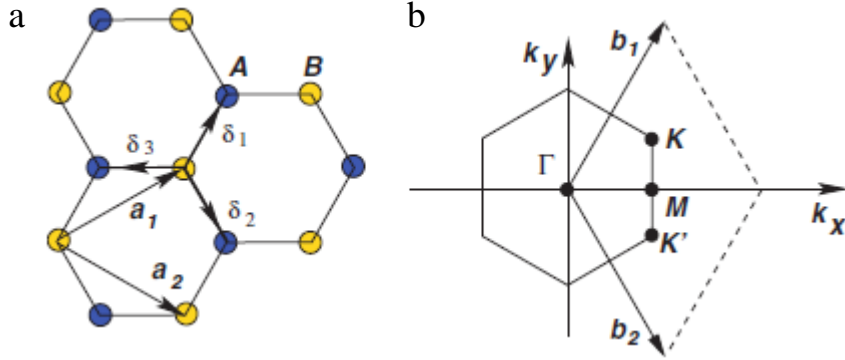


**Figure 1.3** (a) Honeycomb lattice of monolayer graphene consisting of A, B sublattices. (b) Brillouin zone of graphene in momentum space.  $\mathbf{K}$  and  $\mathbf{K}'$  are Dirac points. Figure from Ref. [28]

Lattice constants and other related parameters shown in Fig. 1.3a can be written as

$$\mathbf{a}_1 = \left(\frac{\sqrt{3}}{2}a_0, \frac{1}{2}a_0\right), \mathbf{a}_2 = \left(\frac{\sqrt{3}}{2}a_0, -\frac{1}{2}a_0\right), \delta_1 = \left(\frac{1}{2\sqrt{3}}a_0, \frac{1}{2}a_0\right), \delta_2 = \left(\frac{1}{2\sqrt{3}}a_0, -\frac{1}{2}a_0\right),$$

$$\delta_3 = \left(-\frac{\sqrt{3}}{3}a_0, 0\right). \text{ And the reciprocal lattice vector } \mathbf{b}_1 = \frac{2\pi}{a_0}\left(\frac{1}{\sqrt{3}}, 1\right), \mathbf{b}_2 = \frac{2\pi}{a_0}\left(\frac{1}{\sqrt{3}}, -1\right).$$

Here the coordinate system is chosen where  $|\mathbf{a}_1| = |\mathbf{a}_2| = \sqrt{3}c_0 = a_0$ , where  $c_0$  is the carbon-carbon bond length, equal to  $1.42 \text{ \AA}$ .

Using tight bonding approximation, the Hamiltonian of  $\pi$  electrons hopping between neighboring  $p_z$  orbitals can be expressed as [29]:

$$H_0 = -t \sum_{\langle i,j \rangle, \sigma} (a_{\sigma,i}^+ b_{\sigma,j} + \text{H.C.}) \quad (1.1)$$

where  $a^+(a)$  is the creation (annihilation) operator of the A sublattice electrons (an equivalent definition is used for B sublattice.). The subscript  $\sigma$  refers to the spin of the electron. The nearest-neighbor hopping energy is  $t \approx 2.8$  eV. By doing the Fourier transformation, the operators can be written in the reciprocal space as:  $a_{n,\sigma} = \frac{1}{N} \sum_{\vec{k}} e^{i\vec{k}\cdot\vec{n}} a(\vec{k})$  and  $b_{n,\sigma} = \frac{1}{N} \sum_{\vec{k}} e^{i\vec{k}\cdot\vec{n}} b(\vec{k})$ , where  $N^2$  is the number of primitive unit cells. Then the Hamiltonian in  $k$ -space is expressed as:

$$H_0 = -t \sum_{\vec{k}} \begin{pmatrix} a^+(\vec{k}) & b^+(\vec{k}) \end{pmatrix} \begin{pmatrix} 0 & \varphi^*(\vec{k}) \\ \varphi(\vec{k}) & 0 \end{pmatrix} \begin{pmatrix} a(\vec{k}) \\ b(\vec{k}) \end{pmatrix} \quad (1.2)$$

where  $\varphi(\vec{k}) = e^{ik_x a_0/\sqrt{3}} + 2e^{-ik_x a_0/2\sqrt{3}} \cos(\frac{k_y a_0}{2})$  and  $\varphi^*(\vec{k})$  is its complex conjugate. By diagonalizing this Hamiltonian, the equation can be analytically solved and the energy eigenvalue is expressed in the dispersion relation of the electrons as [30]:

$$E(\vec{k}) = \pm t \sqrt{1 + \cos^2(\frac{k_y a_0}{2}) + 4 \cos(\frac{k_y a_0}{2}) \cos(\frac{\sqrt{3} k_x a_0}{2})} \quad (1.3)$$

It vanishes at six  $\mathbf{K}$  points:  $\pm \frac{2\pi}{a_0} (\frac{1}{\sqrt{3}}, \frac{1}{3})$ ,  $\pm \frac{2\pi}{a_0} (0, \frac{2}{3})$ ,  $\pm \frac{2\pi}{a_0} (-\frac{1}{\sqrt{3}}, \frac{1}{3})$ . One can show that only two of these points are inequivalent in the reciprocal lattice, denoted by  $\mathbf{K}$  and  $\mathbf{K}'$ , known as Dirac points. The complete band diagram of graphene is shown in Fig. 1.4a. However, Eqn. (1.3) can be expanded in powers of  $k$  near  $\mathbf{K}$  and  $\mathbf{K}'$ , i.e. the region near the Dirac points. The first term in the expansion is linear:

$$E(\vec{k}) = \pm \hbar v_F |\vec{k}| \quad (1.4)$$

where  $v_F = \frac{\sqrt{3}}{2\hbar} t a_0$  is the Fermi velocity of monolayer graphene and equals to  $\sim 10^6$  m/s. This linear approximation for graphene's band structure is usually acceptable up to energies of 1-2 eV, thus covering the range of interband transitions up to a few eV,

corresponding to photons from the visible to THz range. The linear dispersion relation denotes a constant group velocity  $d\omega/dk$ . The Hamiltonian of  $\pi$  electrons has a spinor wavefunction, similar to Dirac particles. Therefore, low energy excitations in graphene are regarded as massless Dirac fermions. Considering that the carrier density  $n = g_s g_v \frac{\pi k_F^2}{(2\pi)^2}$ , where  $g_s = g_v = 2$  in graphene corresponding to the spin and valley degeneracy, one can calculate the density of states (DOS) of graphene near the Dirac point:  $D(E) = \frac{dn}{dE} = \frac{2E_F}{\pi \hbar^2 v_F^2}$ . The  $D(E)$  linear in energy in a Dirac system such as graphene contrasts with a massive electron system in which  $D(E)$  is constant up to the band edge, suggesting that graphene can have a much lower density of states than other 2D materials. As a result of this, the electron specific heat  $C$  of graphene is also very small, since it is proportional to the density of states:

$$C = \frac{\pi^2}{3} k_B^2 T \cdot D(E) \quad (1.5)$$

where  $k_B$  is the Boltzmann constant and  $T$  is the electron temperature. This is a useful property when considering graphene as a photodetector based on thermal effects: First of all, for the same heat injection, a small electron specific heat implies a large temperature increase in the electron system. Furthermore, the response time of a thermal system is characterized by the thermal  $RC$  time constant, where  $R$  is the thermal resistivity and  $C$  is the specific heat. A small specific heat helps to reduce the thermal response time of the device. In addition, being different from traditional semiconductors, graphene is a zero band gap material, implying that the charge carrier vertical transitions due to photon absorption can happen at any low frequency. All of these are associated with the realization of an effective photodetector based on graphene. Detailed discussions will be shown in following chapters.

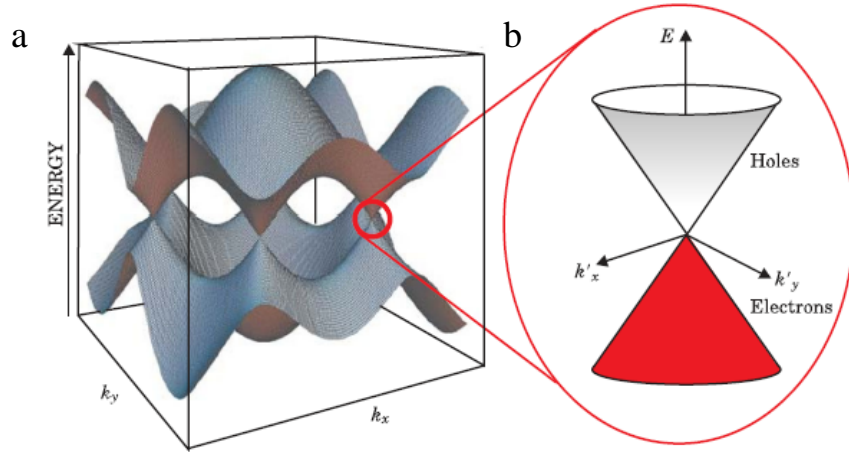


**Figure 1.4** (a) Graphene band structure. (b) Band diagram close to the  $\mathbf{K}$  and  $\mathbf{K}'$  points showing the Dirac cones. Figure adapted from Ref. [29, 31]

### 1.2.2 Charge scattering in graphene

A striking aspect of graphene charge transport is to study the interaction between carriers, lattice and the environment. Moving charge carriers are scattered by phonons (quantized thermal vibrations) of the graphene lattice, substrate phonons, and disorder in graphene (nearby charged impurities, point defects, etc.), which is not only essential for the carrier transport, but also relevant to the photodetection in graphene, since the photo excited carriers will be scattered as well, when they move in the device to generate an electrical signal.

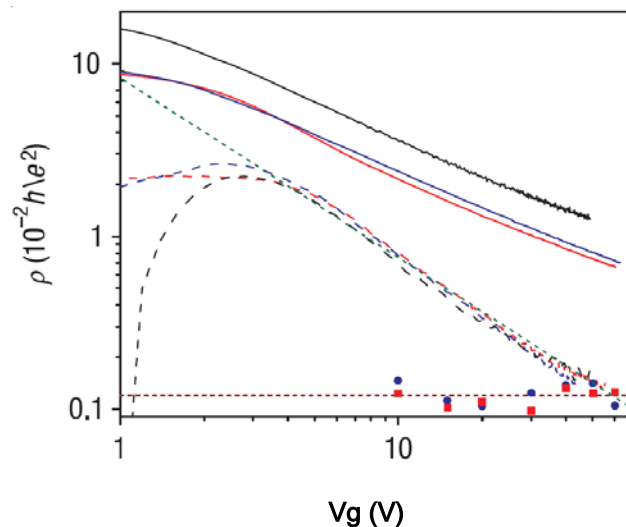


**Figure 1.5** Residual resistivity (solid lines), LA phonon resistivity (blue and red dots from two samples, brown dotted line based on Eqn. (1.6)), and  $\text{SiO}_2$  remote

interfacial phonon resistivity (black, red and blue dashed lines from three samples, and green dashed line based on (Eqn. 1.8)) as a function of gate voltages. Figure adapted from Ref. [32]

Fig. 1.5 plots graphene's resistivity as a function of the gate voltage (proportional to the carrier density), sketching the effects of different scattering types on the resistivity. The first scattering effect shown here is the interaction between carriers and the longitudinal acoustic (LA) phonon in graphene. This scattering effect is essential since it is inevitable in the device. It limits the device's performance intrinsically. LA phonon scattering is expected to induce resistivity in graphene, which can be expressed as [33, 34]:

$$\rho_{LA} = \left(\frac{\hbar}{e^2}\right) \frac{\pi^2 D_A^2 k_B T}{2h^2 \rho_s v_s^2 v_F^2} \quad (1.6)$$

where  $\rho_s = 7.6 \times 10^{-7} \text{kg/m}^2$  is the 2D mass density of graphene,  $v_s = 2.1 \times 10^4 \text{m/s}$  is the sound velocity for LA phonons, and  $D_A$  is the acoustic deformation potential. According to Eqn. (1.6), LA phonon induced resistivity is proportional to the temperature and independent of the carrier density. Chen et al. (Univ. of Maryland) characterized LA phonon scattering experimentally. As shown in Fig. 1.5, LA phonon scattering only contributes  $30 \Omega$  to graphene's resistivity at room temperature, suggesting a weak electron-phonon coupling. The mean free path corresponding to this intrinsic scattering can also be calculated:  $l = v_F \tau$ , where  $\tau$  is the scattering time, which can be written as:

$$\tau = \frac{\mu \hbar \sqrt{\pi n}}{e v_F} \quad (1.7)$$

where  $\mu$  is the mobility and  $n$  is the carrier density. Assuming a technologically relevant carrier density of  $10^{12} \text{cm}^{-2}$ , the mean free path is estimated to be  $> 2 \mu\text{m}$ .

For graphene on  $\text{SiO}_2$  substrate, charge carriers are also scattered by the polar optical phonons of the substrate through remote interfacial phonon (RIP) scattering [35, 36]. The two strongest surface optical phonon modes in  $\text{SiO}_2$  are calculated to

have energy 59 meV and 155 meV [35, 36]. The surface phonon contributed resistivity is then expressed as [32]:

$$\rho_{PO}(V_g, T) = C_{PO} V_g^{-\alpha} \left( \frac{1}{e^{(59\text{meV})/k_B T} - 1} + \frac{6.5}{e^{(155\text{meV})/k_B T} - 1} \right) \quad (1.8)$$

where  $C_{PO}$  is a constant defining the strength of the scattering and  $\alpha$  is the exponent on the density dependence. The number 6.5 in the second numerator describes the ratio of coupling to the carriers in these two scattering process. The measurement of the surface phonon contributed resistivity as a function of the gate voltage is plotted in Fig. 1.5 with dashed lines.  $\rho_{PO}$  is determined to be inversely proportional to the carrier density and is predicted to contribute less to the total resistivity than the LA phonon of graphene in highly doped samples.

Some other scattering centers other than the phonon also exist in graphene devices, such as the charged impurities [37], point defects [38], and corrugations of the graphene sheet [39]. The resistivity induced by these scattering centers is called the residual resistivity, which has a power-law dependence on the carrier density and the prefactor varies from sample to sample. The data shown in Ref. [32] indicates that  $\rho_{\text{residue}} \sim n^{-0.7}$ .

In a word, the intrinsic phonon scattering in graphene is weak at room temperature and independent of the carrier density, implying very slow thermalization of electrons in graphene. The extrinsic phonon scattering and the residue scattering depend on the carrier density. They determine the transport of charge carriers in low doped graphene. However, by using novel fabrication techniques such as suspending graphene between the contacts [40, 41] or putting graphene on boron nitride substrate [42], these effects can be largely reduced.

### 1.2.3 Electron-electron interaction in graphene

Lastly I briefly review the electron-electron interaction and the carrier multiplication in graphene to conclude this chapter. In considering graphene for photodetection, it is important to note that photo excited carriers are not only scattered by the lattice and the scattering centers in the environment, but interact with other charge carriers as well. This is a notable effect in graphene. Tse et al. [43] showed theoretically that the Coulomb scattering rate exceeds the optical phonon emission rate, suggesting a strong electron-electron interaction in graphene. This is confirmed experimentally in ultra-fast hot carrier dynamics studies [44-47]. As shown in Fig. 1.6, the hot carrier scattering time is characterized by measuring the differential transmission as a function of the delay time between the pump and the probe pulses. It is observed in Fig. 1.6 that the signal drops fast at the first  $\sim 20$  fs and then slowly drops down. A numerical fit convoluted with the cross correlation gives time constants  $\tau_1 = 13 \pm 3$  fs, which is identified as the electron-electron scattering rate, and  $\tau_2 \approx 100$  fs, which corresponds to the optical phonon emission rate. The fact that  $\tau_1$  is one order less than  $\tau_2$  suggests that photo excited electrons first thermalize through the electron-electron interaction and then hot electrons emit optical (if hot enough) and acoustic phonons.

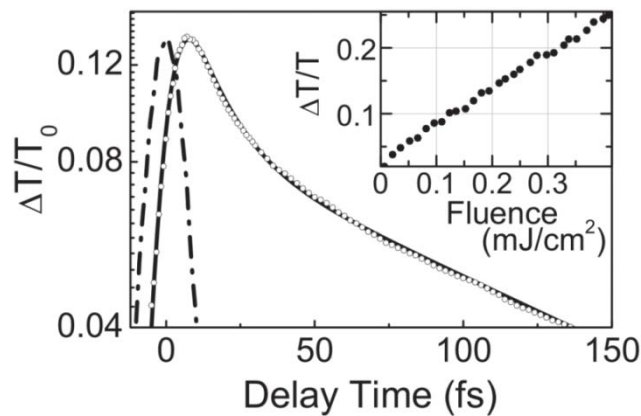


**Figure 1.6** Spectrally integrated differential transmission as a function of pump-probe delay: experiment (open circles) and numerical fit (solid line). Dash-dotted line:



Cross correlation of pump and probe pulses. Inset: Linear dependence of the maximum transmission change on the absorbed pump fluence. Figure from Ref. [44]

Another interesting phenomenon in graphene that is potentially useful for photodetection is carrier multiplication based on the electron-electron interaction. Carrier multiplication is defined as the generation of multiple charge carriers due to the absorption of a single photon [48]. For example, in *p*-doped graphene, the photoexcited hot electron can be scattered by the low-energy electrons and cause the interband transition of those electrons, which is called impact ionization (inverse Auger recombination). Thus, more electron-hole pairs are generated in the material. As a zero-bandgap semiconductor, graphene is an ideal model structure to study this process, which is usually inefficient in large gap semiconductors. It was found in Ref. [48] that there is a strong asymmetry between impact ionization and Auger recombination in graphene, leading to a significant multiplication of charge carriers. Especially for small optical excitations, the carrier multiplication factor was shown to be 4.3, excluding the electron-phonon relaxation.

Carrier multiplication in graphene has been observed experimentally by Tielrooij et al. (ICFO) using a pump-probe technique [49]: As shown in Fig. 1.7a, electrons in a monolayer graphene are excited by an optical pump-pulse. After some delay time  $t$ , a terahertz probe-pulse is illuminated on the sample and transmission as a function of the delay time is measured. Fig. 1.7d shows the schematic of the inverse Auger recombination. The hot electron is scattered by charge carriers near the Fermi surface, which can interact with the terahertz probe-pulse and change the transmission intensity of the beam correspondingly. The differential transmission as a function the delay time is plotted in Fig. 1.7b: The Coulomb scattering gives a rise of  $\Delta T$  at the first  $\sim 0.2$  ps and then charge carriers are scattered by phonons relaxing the system back into equilibrium. The carrier multiplication is confirmed by varying the photon density of the pump-pulse and its frequency. Fig. 1.7c plots the peak  $\Delta T$  as a function

of the absorbed photon density for several different photon energies. The linear dependence of  $\Delta T$  on the fluence indicates that in this regime each photoexcited carrier acts independently from the other photoexcited carriers. Interestingly, the differential transmission at the peak is enhanced by increasing the photon energy. Further analysis shows that there is an approximately linear relation between the photon energy and the differential transmission normalized by the fluence, suggesting carrier multiplication as depicted in Fig. 1.7d (The phonon emission should be independent of the photon energy.).

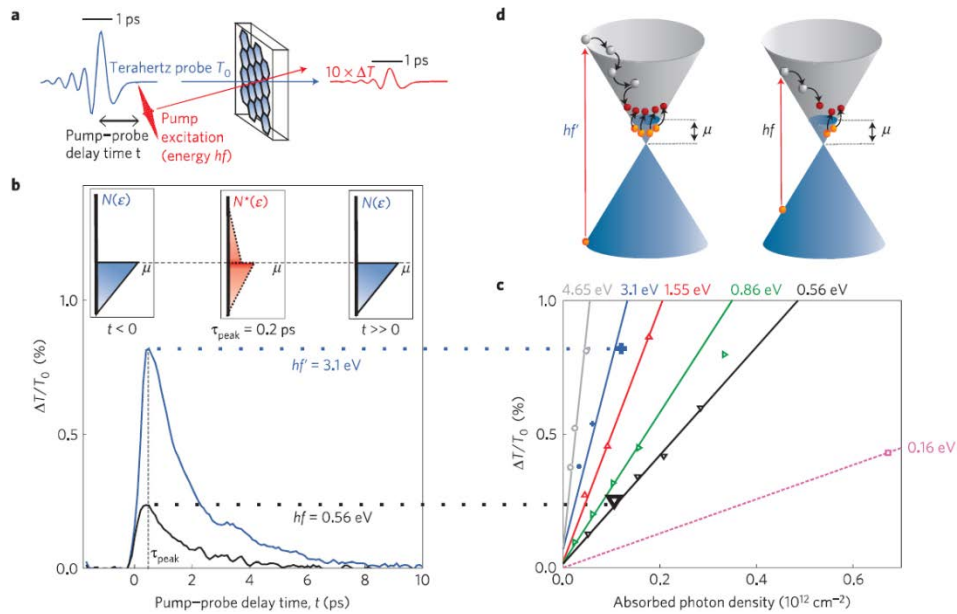


**Figure 1.7** (a) Experimental observation of carrier dynamics. (b) Time-resolved carrier dynamics for two different photon energies. Insets show a schematic representation of the carrier distribution as a function of the time. (c) Scaling of the differential transmission signal peak values for six photon energies as a function of absorbed photon density. (d) A schematic illustrating the impact ionization induced carrier multiplication for two different photon energies. Figure from Ref. [49]

In this chapter I have reviewed the band structure and transport properties of single layer graphene, focusing on properties which are advantageous for photodetection. The electron specific heat of graphene is extremely small due to the low density of states induced by graphene's unique band structure, which makes sensitive and fast thermally based photodetection possible. Graphene shows a strong

electron-electron interaction, which, combined with its zero band gap nature, efficiently induces the carrier multiplication for optical excitation. In addition, the electron-acoustic phonon coupling in graphene is weak, resulting in a slow energy relaxation of hot electrons to the lattice and helping to store the energy in the electron system.

## Chapter 2: Light-matter interaction in graphene

### 2.1 Light absorption in graphene

Eqn. (1.4) suggests that the charge carriers in graphene behave like relativistic particles. Graphene's Fermi energy  $E_F$  can be expressed as a function of the carrier density  $n$ :  $E_F = \hbar v_F \sqrt{\pi n}$ . For a perfect undoped graphene sheet without impurities and disorder, the Fermi energy should be zero since the carrier density vanishes. Practically, inevitable disorder always introduces local fluctuations in  $n$ , termed “electron and hole puddles”, in the system, resulting in a non-zero carrier density and electrical conductivity even when the average Fermi energy is at the Dirac point. The puddle density contributes a local Fermi energy, which has an *rms* value around 50 meV [50] for a graphene sheet on SiO<sub>2</sub>.

While perfectly intrinsic graphene is difficult to realize due to disorder-induced puddling, extrinsic (doped) graphene can be realized, most easily by applying a gate voltage between graphene and a capacitively-coupled gate electrode. A common geometry is graphene over 300 nm SiO<sub>2</sub> dielectric on doped Si wafer, where the doped Si acts as a “back gate”. In such a scheme the back gate voltage generally tunes the Fermi level to  $\pm$  (200 – 300 meV). Other electrochemical doping techniques, such as the molecular charge-transfer doping using molecules such as tetrafluoro-tetracyanoquinodimethane (F4TCNQ) and polymer electrolyte top gates [51], can heavily dope graphene to Fermi levels around 500 meV. The photon energy from visible to far infrared covers a wide range between a few meV and a few eV. Therefore, both interband and intraband transitions need to be considered in the photoexcitation of graphene. These are discussed separately below.

### 2.1.1 Optical absorption due to interband transitions

For incident photon with relatively high energy, the interband transition dominates the absorption. Fig. 2.1 shows the transmission spectra of monolayer and bilayer graphene in the optical range. The key point to calculate light absorption is to determine the optical conductivity (ac conductivity), which is a material property, linking the current density to the electric field for general frequencies. The quantum treatment, assuming the photon energy  $E$  is much larger than the temperature and Fermi energy, predicts the optical conductivity of a two dimensional Dirac spectrum with a conical dispersion relation to be a constant independent of frequency [52-55]:

$$\sigma \equiv e^2 / 4\hbar \quad (2.1)$$

implying that the transmittance, absorption and reflection of graphene can be expressed through fundamental constants in optical range. For example, based on reference [55], the transmittance of monolayer graphene can be written as  $T = (1 + 2\pi\sigma/c)^{-2} \approx 1 - \pi\alpha$ , where  $\alpha$  is fine structure constant. Since the reflection of graphene is very small, the absorption can be approximated as  $A \approx 1 - T \approx 2.3\%$ . This is a notably large value for a one-atom-thick layer.

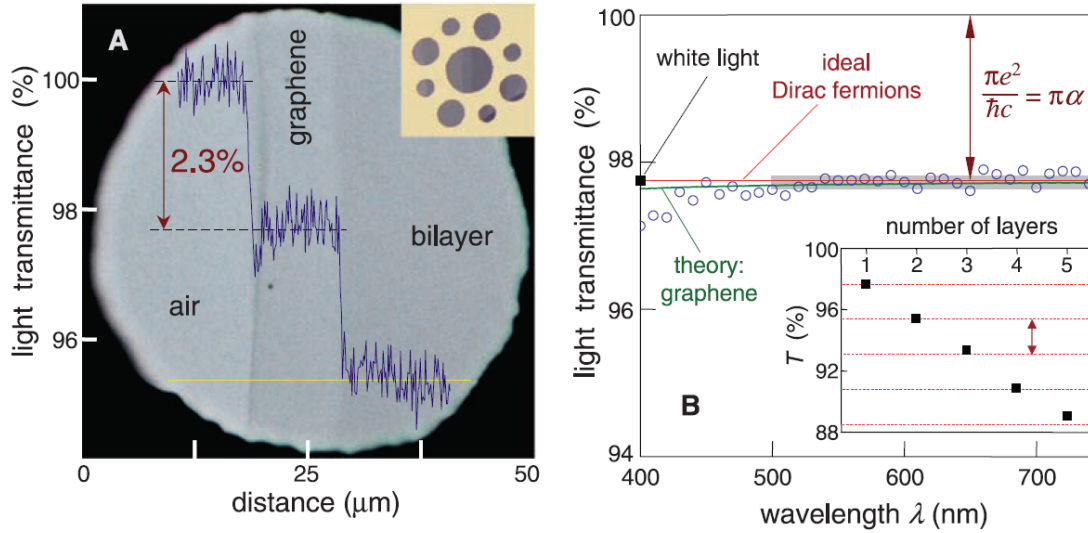


**Figure 2.1** (A) Photograph of a 50-μm aperture partially covered by graphene and its bilayer. The line scan profile shows the intensity of transmitted white light along the yellow line. (B) Transmittance spectrum of monolayer graphene (open circles) and

theoretical prediction (red line) and correction (green line). (Inset) Transmittance of white light as a function of the number of graphene layers. Figure from Ref. [56]

Fig. 2.1 shows the white light transmittance for few layer suspended graphene characterized by Nair et al. (Univ. of Manchester) [56]. In the visible spectrum range, the data matches very well with the theory for Dirac fermions. Besides, the transmittance roughly scales linearly with the layer number of graphene up to 5 layers. Notice that the measured graphene sheet is suspended, thus the refractive index of the environment can be approximated as 1. For a substrate-supported graphene sheet, the medium property also plays a role in light-matter interaction. Since graphene is a layered material, the theory of thin film optics applies for this medium-coupled transmission. Considering a general condition, where a graphene sheet is located at the boundary of two media with the refractive index  $n_{1,2}$ , and assume the normal incidence of the light, the transmittance through the film can be written as [57]:

$$T = \frac{4n_1n_2}{|n_1 + n_2 + Z_0\sigma|^2} \quad (2.2)$$

where  $Z_0 = 377\Omega$  is the impedance of the free space and  $\sigma$  is the AC conductivity. Eqn. (2.2) is the general expression for the transmission through a graphene sheet sandwiched by the media and will be used in following chapters. Taking  $n_1 = n_2 = 1$ , the expression for suspended graphene is recovered. Respectively, the absorption and the reflectance are expressed as:

$$A = \frac{|4n_1Z_0\sigma|}{|n_1 + n_2 + Z_0\sigma|^2} \quad (2.3)$$

$$R = \frac{|n_1 - n_2 - Z_0\sigma|^2}{|n_1 + n_2 + Z_0\sigma|^2} \quad (2.4)$$

It is necessary to emphasize that in Eqn. (2.2),  $n_1$  and  $n_2$  are interchangeable, which means the transmission does not depend on the propagation direction of the light beam. However, the absorption and reflectance do show a dependence on the

propagation direction. In Eqn. (2.3) and Eqn. (2.4), the light is assumed to transmit from medium 1 to medium 2.

Returning to the interband transition in graphene, Eqn. (2.1) is valid for photon energies larger than twice the Fermi energy. Below this, the absorption starts to decrease in doped graphene. This phenomenon is called Pauli blocking: The photoexcited charge carrier can only transmit to a state that is not occupied by a charge carrier. The interband transition in graphene requires the initial state and the final state to keep the same  $k_F$ , in order to satisfy the momentum conservation law, which means, the blue arrow shown in Fig. 2.2a has to be vertical. In addition, the length of the arrow represents the photon energy. All of these suggest that only those photons with energy larger than  $2E_F$  can be absorbed by the doped graphene. Wang et al. (UC Berkeley) [58] and Mak et al. (Columbia Univ.) [59] studied the gate tuning of interband optical transitions in graphene, as shown in Fig 2.2b. The carrier density (thus the Fermi level) of the device is tuned by applying an ion liquid top gate voltage. The gate-induced change of transmission is plotted as a function of the incident photon energy. Due to Pauli blocking, the transmission spectrum shows a step-like shape, showing that the transmission is enhanced when the photon energy of the incident radiation is below  $2E_F$ . The threshold energy is shifted due to the Fermi level drift by tuning the gate voltage.

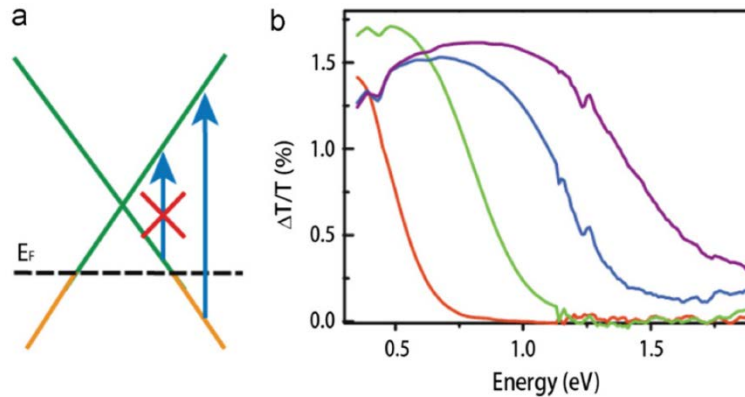


**Figure 2.2** (a) An illustration of Pauli blocking in hole-doped graphene. (b) The gate-induced change of transmission in hole-doped graphene as a function of the photon

energy of the incident radiation. The values of the gate voltage referenced to that for charge neutrality, for the curves -0.75, -1.75, -2.75 and -3.5V, from left to right. Figure from Ref. [59]

### 2.1.2 Optical absorption due to intraband transitions

The interband transition dominates the light-matter interaction in graphene in the visible and near infrared range. However, the situation is different for excitation with even lower energy in doped graphene, where the interband transition is forbidden due to Pauli blocking. The intraband transition, also called the free carrier response, determines the light-matter interaction in the long wavelength range. The ac conductivity of graphene changes its form when the photon energy is small. In this case, the long wavelength limit approximation can be used and charge carriers in graphene are treated as quasi-classical particles. The simplest way to calculate the long wavelength ac conductivity is to use the Drude model [60]: Assuming the momentum per electron under the external electric field  $\vec{E}(\omega)$  is  $\vec{p}(t)$  at time  $t$ , then the momentum after a very small time interval  $dt$  can be written as  $\vec{p}(t + dt) = \vec{p}(t) + e\vec{E}(\omega)dt$ . There is a chance that the electron is scattered to another direction during this time interval with the possibility  $dt/\tau$ , where  $\tau$  is the electron scattering time. Assuming that the scattered electron can travel to any direction with the same possibility, only the unscattered electron needs to be considered. Therefore, the kinetic equation of the electron can be written as  $\vec{p}(t + dt) = \left(1 - \frac{dt}{\tau}\right)(\vec{p}(t) + e\vec{E}(\omega)dt)$ , which is simplified as:

$$\frac{d\vec{p}}{dt} = e\vec{E}(\omega) - \frac{\vec{p}}{\tau} \quad (2.5)$$

For an electromagnetic wave,  $\vec{E}(\omega) = \vec{E}_0 e^{i\omega t}$ , Eqn. (2.5) can be solved by assuming the electron momentum has the same time dependence. Combined with equations, which describe the current density  $\vec{J} = ne\vec{v}$ , and the relation between the current



density and external electric field  $\vec{J}(\omega) = \sigma(\omega)\vec{E}(\omega)$ , one can derive the frequency-dependent Drude conductivity [29, 60]:

$$\sigma(\omega) = \frac{\sigma_0}{1+i\omega\tau} = \frac{\sigma_0}{1+\omega^2\tau^2} - i\frac{\sigma_0\omega\tau}{1+\omega^2\tau^2} \quad (2.6)$$

where  $\sigma_0$  denotes the dc conductivity. It is usually convenient to define Drude weight  $D = \pi\sigma_0/\tau$  to express the Drude conductivity with microscopic material parameters. For conventional semiconductors and metals, the Drude weight is related to carrier density  $n$  and carrier effective mass  $m^*$ :  $D = \pi ne^2/m^*$ . This expression requires careful modification in the case of graphene in which the effective mass approximation fails.

Generally, for a 3D electron system, the dc conductivity can be written as [60]:

$$\sigma_0 = e^2 \int \frac{d\mathbf{k}}{4\pi^3} \tau(E(\mathbf{k})) \mathbf{v}(\mathbf{k}) \mathbf{v}(\mathbf{k}) \left(-\frac{\partial f}{\partial E}\right)_{(E=E(\mathbf{k}))} \quad (2.7)$$

Where  $\tau$  is the relaxation time,  $v$  is the electron group velocity and  $f$  is the Fermi function. To evaluate this equation at  $T = 0$ , the relaxation time can be taken outside of the integral, since  $(-\frac{\partial f}{\partial E}) = \delta(E - E_F)$ . Then the integral is expressed as:

$$\sigma_0 = e^2 \tau(E_F) \int \frac{d\mathbf{k}}{4\pi^3 \hbar} \frac{\partial}{\partial \mathbf{k}} \mathbf{v}(\mathbf{k}) f(E(\mathbf{k})) \quad (2.8)$$

Based on Eqn. (2.8), the Drude weight can be calculated for electrons with an arbitrary dispersion relation. For a free electron system,  $\frac{\partial v}{\hbar \partial k} = 1/m^*$ . The Drude weight form  $D = \pi ne^2/m^*$  is then recovered by substituting this in Eqn. (2.8).

Graphene is a two-dimensional system and its electron group velocity is  $v_F$ . Therefore, Eqn. (2.8) should be rewritten as:

$$\sigma_0 = e^2 \tau(E_F) v_F \int \frac{d\mathbf{k}}{2\pi^2 \hbar} \frac{\partial}{\partial \mathbf{k}} f(E(\mathbf{k})) \quad (2.9)$$

Using Eqn. (2.9), graphene's Drude weight is written in a different form:  $D = \sqrt{\pi n} e^2 v_F / \hbar$ . The absorption due to the intraband transition can be expressed using

Eqn. (2.3). Assuming a suspended graphene sheet ( $n_1 = n_2 = 1$ ) and graphene resistivity much larger than the impedance of the free space, Eqn. (2.3) is rewritten according to the long wavelength limit as:

$$A(\omega) = Z_0 \operatorname{Re}[\sigma(\omega)] \quad (2.10)$$

Wang's group at UC Berkeley [61] measured experimentally the ac conductivity of graphene as a function of infrared frequency using far-IR spectroscopy technique, as shown in Fig. 2.3, which can be regarded as a scaled absorption spectrum. Spectra at different gate voltages are shown with a fit to the Drude model [53, 62]. The absorption increases with carrier density, because it gives a rise in  $\sigma_0$ . For a fixed gate voltage, the absorption decreases with the increasing frequency. According to Eqn. (2.6), the spectrum actually shows half of a Lorentzian peak. The width of the peak is determined by the scattering time  $\tau$ , which is related to the mobility of graphene and will be discussed more in following chapters. At zero frequency, the absorption is solely determined by the dc conductivity of the material.

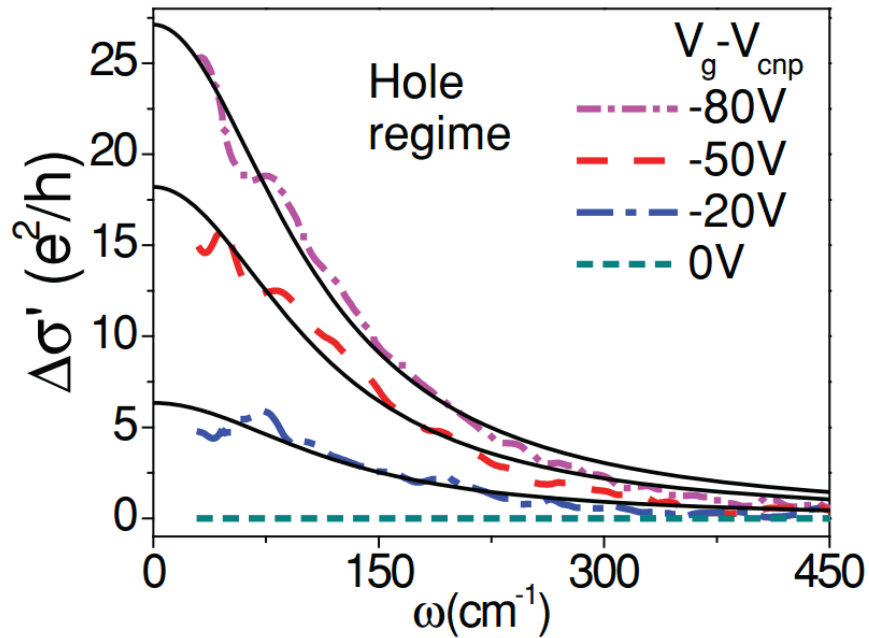


**Figure 2.3** Change in the optical sheet conductivity of graphene in the infrared range induced by electrostatic doping. Figure from Ref. [61]

Fig. 2.4 shows the theoretical optical conductivity of graphene over a broad range of frequencies calculated by Peres et al. (Univerisdade do Minho) [63], compared with the experimental result. [64] The plot summarizes the characteristics of the light-matter interaction in graphene from far infrared to the optical range. The interband transition dominates from the optical to near-IR range, resulting in a frequency independent absorption. The interband-transition induced absorption is strongly reduced in the mid-IR range due to Pauli blocking. The intraband transition dominates the far-IR range, resulting in a frequency dependent absorption peaked at zero frequency, according to the Drude model. The gate voltage tunes the Fermi energy, determining the frequency where Pauli blocking happens, and the absorption at zero frequency depends on the dc conductivity [64]. These two properties are both related to the carrier density in graphene. The width of the Drude absorption in the far-IR is determined by graphene's electron scattering time.

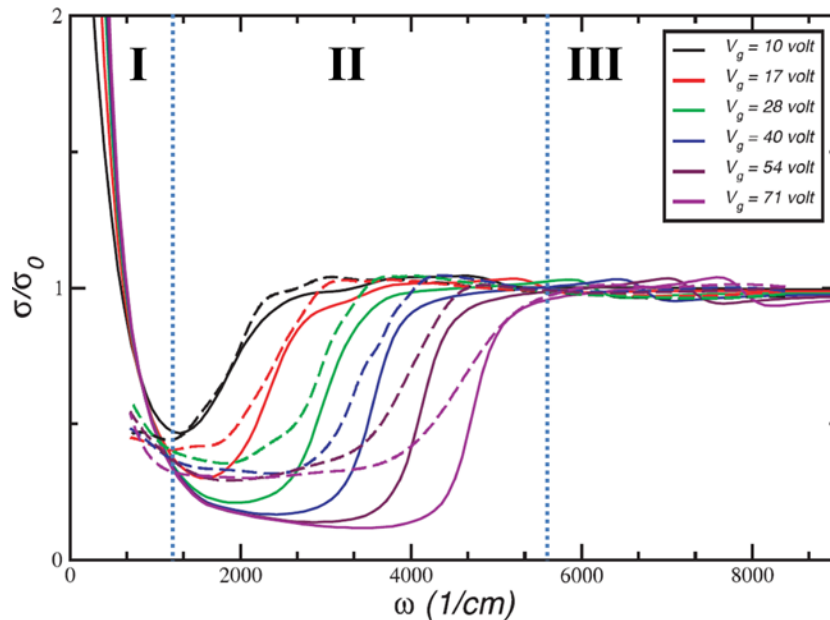


**Figure 2.4** Real part of the infrared conductivity including the effect of phonons, unitary scatterers and charged impurities. Solid lines: Theoretical curves. Dashed lines: Experimental data. Blue dotted lines show the boundaries (for the spectrum at  $V_g = 71$  V) between Drude response (I), Pauli blocking (II) and the interband transition (III) dominant ranges. Figure adapted from Ref. [63]

## 2.2 Plasmon excitation in finite-sized graphene

There is an assumption when treating the low frequency excitation in graphene using a Drude model, i.e. the graphene sheet is infinitely large in a 2D surface, which allows electrons move freely under the oscillating electric field of the incident radiation and are only scattered by phonons and other scattering centers of residual, which is the reason why the zero frequency absorption only depends on the dc conductivity of the sample. A real graphene sample always has finite size and in many cases, the dimension of it is only few microns, which means electrons driven by the oscillating electric field are not able to go further at the boundary of the sample if graphene is not connected to some conducting material. This results in a change of the absorption spectrum in the long wavelength range.

To describe the light-matter interaction in a patterned graphene sample, the plasmonic behavior needs to be taken into account. In physics, a plasmon is a quantum of plasma oscillation. The plasmon is a quasi-particle resulting from the quantization of the plasma oscillation just as photons and phonons are quantizations of electromagnetic and mechanical vibrations, respectively. Thus, plasmons are described in the classical picture as an oscillation of free electron density with respect to the fixed positive charges in the material. The plasmon resonance can be excited by the external electromagnetic field if both their frequency (energy) and the momentum match with each other. Once the electromagnetic field satisfies the condition to excite plasmon resonance in the material, its absorption will be strongly enhanced. Plasmons have been studied extensively in metallic materials and are proposed to have broadband potential applications [65-67].

Similar to metallic materials, each carbon atom in graphene's lattice has a  $\pi$ -orbital electron, which can be regarded as a free electron, making it possible to couple the incident light into the electron system and excite the plasmon resonance. However,

graphene's plasmon is different from the bulk plasmon in a 3D metal: Due to the 2D nature and low charge carrier density, the plasmon resonance peak of a patterned graphene is usually covered by far-IR or mid-IR frequencies [68, 69]. In addition, as massless Dirac fermions, charge carriers in graphene show a different dispersion relation (Eqn. 1.4) from free electrons in general materials, thus the strict consideration of the plasmon in graphene should take into account the quantum mechanics [70, 71]. However, as a long wavelength limit approximation, one can still use the classical analysis to treat the system to get the basic picture of plasmons in the monolayer graphene system. As shown in Fig. 2.5, an oblate spheroidal particle is used to describe a piece of graphene with the height to be  $2c$  and the diameter to be  $2a$ . The dielectric constant of graphene and the medium are  $\xi^i$  and  $\xi^e$ , respectively. At the end, I will let  $D \rightarrow 0$ . The electron motion equation based on the Drude model (Eqn. 2.5) is rewritten as:

$$\dot{\vec{p}} + \gamma \vec{p} = -e \vec{E} \quad (2.11)$$

where  $\gamma = 1/\tau$  denotes to the scattering rate. Let  $\vec{E}(t) = \vec{E}_0 e^{-i\omega t}$ , one can solve for the displacement of the electron and get:

$$\vec{x}(t) = \frac{e}{m(\omega^2 + i\omega\gamma)} \vec{E}(t) \quad (2.12)$$

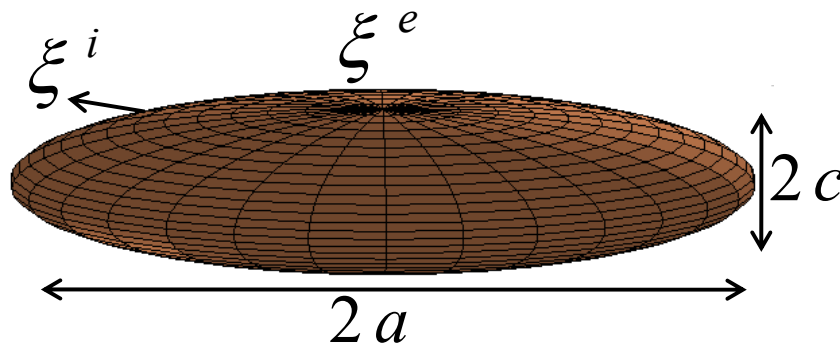


**Figure 2.5** Schematic of a piece of graphene flake with pancake geometry ( $d = 2a$ ,  $h = 2c$ ) and dielectric constant  $\xi^i$ . The environment dielectric constant is  $\xi^e$ .

Next, one can describe the collective oscillation of electrons using the susceptibility:

$\vec{P} = -ne\vec{x}$  . Therefore, the electrical displacement can be expressed as  $\vec{D} = \xi^i \vec{E} = \xi_0 \vec{E} + 4\pi\vec{P} = \xi_0 \vec{E} + 4\pi(-ne\vec{x})$  . Using Eqn. (2.12), one can write the dielectric constant inside graphene as:

$$\xi^i = \xi_0 - \frac{\omega_p^2}{\omega(\omega + i\gamma)} \quad (2.13)$$

where  $\omega_p^2 = \frac{4\pi ne^2}{m}$  .

For the spheroid geometry assumed at the beginning, the electric fields inside ( $E^i$ ) and outside ( $E^o$ ) the material are related by the following equation:

$$E^i = \frac{\xi^e E^o}{\xi^e + (\xi^i - \xi^e)n^x}$$

$$\Rightarrow 4\pi P = \frac{(\xi^i - 1)\xi^e E^o}{\xi^e + (\xi^i - \xi^e)n^x} \quad (2.14)$$

where  $n^x \equiv \frac{\pi c}{4a}$  . For a resonance peak, one should have the denominator of the right side term in Eqn. (2.14) to be zero. Using Eqn. (2.13) and ignoring small terms, this expression can be rewritten as:

$$\xi^e \approx \frac{4\pi ne^2 / m}{\omega_R(\omega_R + i\gamma)} \frac{\pi t}{4D} \quad (2.15)$$

where  $t = 2c$  and  $D = 2a$ . The next step is to let  $t \ll 0$  and replace the carrier density  $n$  with the 2D carrier density  $n_2$ , which needs to project the oblate spheroidal particle into the 2D surface as a round disk with the diameter  $D$  [72]. Therefore, the relation between  $n$  and  $n_2$  can be expressed as:  $n_2 = n \frac{V}{A}$ , where  $V = \frac{4}{3}\pi ca^2$  and  $A = \pi a^2$ . Then  $nt$  in Eqn. (2.15) are replaced with  $3n_2/2$ . Considering the real part of Eqn. (2.15) and replacing the effective mass of the electron by using the relation  $mv_F = \hbar k_F$ , one can rewrite it as:

$$\omega_R^2 \approx \frac{3\pi^{3/2} \sqrt{n_2} e^2 v_F}{2\xi\hbar D} \quad (2.16)$$

Eqn. (2.16) shows the plasmon resonance frequency in a graphene disk with the diameter  $D$ , which is consistent with the experimental result [73]. More generally, one can use the full quantum mechanical treatment to calculate the plasmon dispersion relation in graphene with any kind of the shape. The result is consistent with what is derived from the classical approximation and can be written as [70, 71]:

$$\omega_R^2 \approx \frac{g_s g_v e^2 \sqrt{\pi n_2} v_F}{2\xi\hbar} q \quad (2.17)$$

where  $g_s = g_v = 2$ , corresponding to the spin and valley degeneracy, and  $q$  is the wave vector.

It is found in Eqn. (2.17), the plasmon resonance frequency in graphene is proportional to  $q^{1/2}$ , which is consistent with the normal 2D plasmons [74]. However, the carrier density dependence of  $\omega_R$  shows a different behavior, i.e. instead of being proportional to  $n^{1/2}$  as the normal 2D plasmons, it is proportional to  $n^{1/4}$ , which is a direct consequence of the relativistic nature of charge carriers in graphene.

Finally, I include this plasmonic effect in the expression of patterned graphene's ac conductivity and see how it changes the absorption spectrum in the far infrared range. The plasmonic ac conductivity of graphene is expressed as:

$$\sigma(\omega) = \frac{\sigma_0}{1 + i(\omega^2 - \omega_R^2)\tau / \omega} \quad (2.18)$$

Fig. 2.6 shows the schematic of Drude and plasmon spectrum of monolayer graphene, according to Eqn. (2.6) and Eqn. (2.18), respectively. Compared to the Drude response, the peak value of the plasmonic ac conductivity shifts from zero frequency to the plasmon resonance frequency, but the magnitude of the peak absorption does not change, which is still solely determined by the dc conductivity. Detailed analysis and related experimental results will be shown in following chapters.

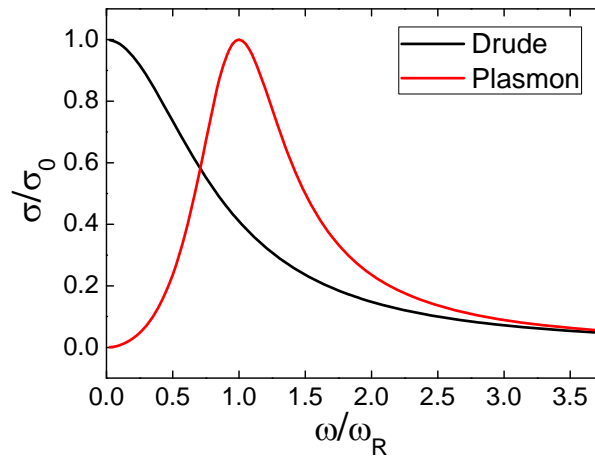


**Figure 2.6** Schematic shown the real part of the ac conductivity as a function of the frequency for a Drude response (black line) and a plasmon response (Red line).

### 2.3 Photodetection mechanisms in graphene

As a photodetector, the device should be capable of transferring the absorbed radiation energy to an electrical signal output. Some techniques to do this in traditional photodetectors have been reviewed in the first chapter. In this section, three main detection mechanisms reported in graphene will be introduced, i.e. the photovoltaic effect, the photothermoelectric effect and the bolometric effect.

#### 2.3.1 Photovoltaic effect

The photovoltaic effect is nowadays a widely used mechanism to make photodetectors based on semiconductor materials. Similar to the photoconductive effect introduced in the previous chapter, the photovoltaic effect also requires the electron-hole pair generation in the material due to photon absorption. However, being different from the photoconductive effect, a photovoltaic detector can work without any bias voltage. The photo-excited electron and hole are driven to opposite



directions due to the built-in electric field in the device and thus generates a photocurrent signal.

The photovoltaic effect is the first reported photocurrent generation mechanism in graphene [75]. It is analyzed in detail in Ref. [76, 77], which report scanning photocurrent measurements in graphene-metal junctions. The results from Park et al. (Cornell Univ.) [76] are shown in Fig. 2.7: Since graphene is connected to metal electrodes, its Fermi level has to be aligned with the Fermi level of the contact, which corresponds to an electron band bending in graphene near the metal electrodes, as depicted in Fig. 2.7d. The bending band creates a built-in electric field, which drives photo-excited electrons and holes to opposite directions and generate an electrical signal. The radiation source in this measurement is a 532-nm laser, which provides photons with high enough energy to excite electrons from the valence band to the conduction band.

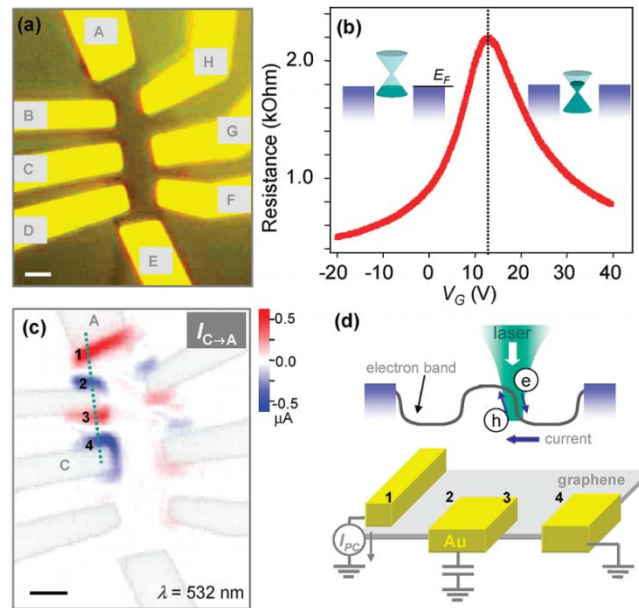


**Figure 2.7** (a) Optical image of a graphene device. (b) Four-probe resistance of the device. (c) Combined light reflection and photo-current image ( $I_{C \rightarrow A}$ ). (d) Schematic of the photocurrent generation in the device. Figure from Ref. [76]

Another approach to build a bending band in graphene is to fabricate graphene *pn* junctions [78]: The local gating technique allows graphene based bi-polar technology

comprising junctions between  $p$ -doped and  $n$ -doped regions. The built-in electric field is generated due to the Fermi level aligning of regions with different doping.

The magnitude of the photovoltaic signal is determined by the photo-excited carrier density  $n_{e/h}^*$ , which can be expressed as [79]:  $n_{e/h}^* = M\alpha P\tau_{rc}/E_{ph}a_{spot}$ , where  $M$  is the carrier multiplication factor,  $\alpha$  is the quantum efficiency,  $P$  is the radiation power,  $\tau_{rc}$  is the carrier recombination time,  $E_{ph}$  is the photon energy and  $a_{spot}$  is the spot size (assuming the light is all focused on graphene). Although the photovoltaic effect is the earliest reported photodetection mechanism in graphene, it might be the least characterized one at this point, because it is complicated to determine  $\tau_{rc}$  [80, 81]. In addition, theories and later experiments show that it is very possible that the photocurrent generated in a device like Fig. 2.7a is a signal due to combined effects [79] [82-85], i.e. the photovoltaic and the photothermoelectric effect, which makes it more difficult to understand the photovoltaic part.

### 2.3.2 Hot electron photothermoelectric effect

In solid state electronic devices, charge carriers can absorb energy through optical excitation or Joule heating and become “hot”. The term “hot” refers to the effective temperature used to model the carrier density, not to the overall temperature of the device. Hot carriers are out of equilibrium and will get relaxed either by phonon scattering or diffusion.

As discussed in Chapter 1.2, graphene is an ideal material to study the hot electron effect, because of its weak electron-phonon coupling, strong electron-electron interaction and small electron specific heat. In this section, I will firstly review the thermoelectric Seebeck effect briefly, which explains how hot carriers diffuse in the material to generate an electrical signal. Then the responsivity of a graphene based photothermoelectric detector will be estimated.

A qualitative picture of the Seebeck effect is shown in Fig. 2.8: Assume there is a uniform metal stripe with free electrons inside. Charge carriers on one side of the stripe are continuously heated to create a temperature gradient of the electrons from the left to the right side. Free electrons start to diffuse according to the temperature gradient. Since electrons at the left side diffuse faster than the right side, more charge carriers will be accumulated at the right side when the system gets into equilibrium. This steady-state non-uniform charge carrier distribution results in a voltage across the metal bar.

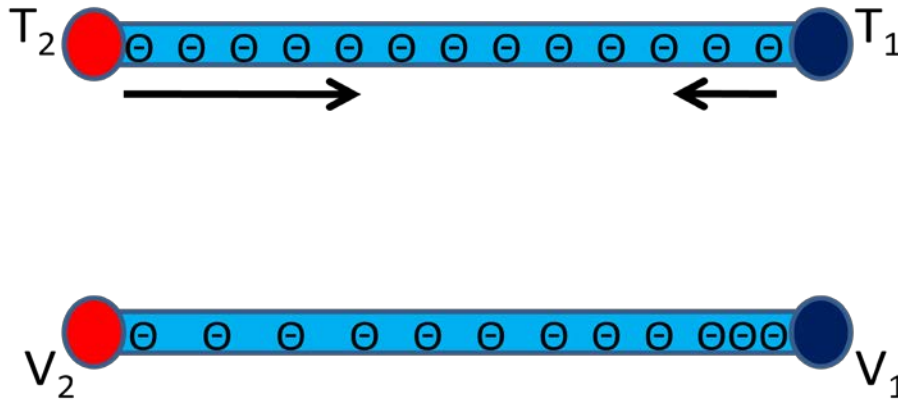


**Figure 2.8** Schematic of the Seebeck effect in a uniform metal bar.

The quantitative description of the Seebeck effect can be found in Eqn. (2.19), where  $S(T)$  is called Seebeck coefficient, an intrinsic property of the material.

$$V = -\int_{T_1}^{T_2} S(T)dT \quad (2.19)$$

The Seebeck coefficient is usually a constant for metals at a fixed temperature. Ignoring electron-phonon effects, the Seebeck coefficient can be determined from the Mott relation [82]:

$$S = LT(d \ln \sigma / dE_F) = \frac{LT}{|E_F|} (d \ln \sigma / d \ln |E_F|) \quad (2.20)$$

where the Lorentz number  $L = \pi^2 k_B^2 / 3e^2$ . In extrinsic graphene, the quantity in parentheses is roughly constant, with positive (negative) sign for electrons (holes). Then graphene's Seebeck coefficient is inversely proportional to  $E_F$ , diverging at small Fermi energy or carrier density. This divergence is cut off due to puddling, which reduces the Seebeck coefficient due to cancellation of electron and hole like Seebeck effect. Graphene's Seebeck coefficient  $S$  has been measured by Kim's group (Columbia Univ.) [86] and Lau's group (UC Riverside) [87] as shown in Fig. 2.9. The Seebeck coefficient has the predicted  $S$ -shape as a function of the gate voltage: proportional to  $1/E_F$  at high carrier density, and crossing zero at low carrier density. It changes the polarity at the charge neutral point (Dirac point) and is proportional to the electron temperature.

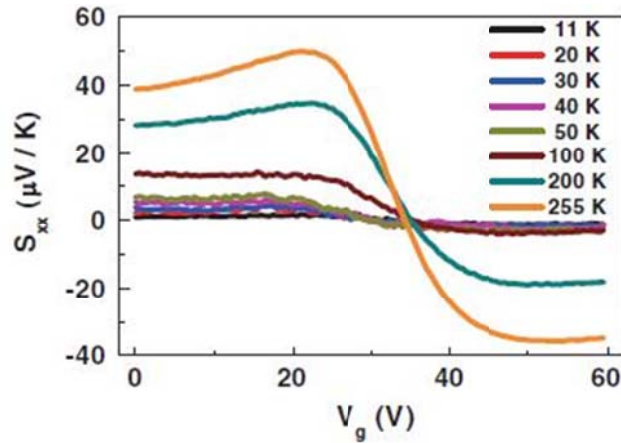


**Figure 2.9** Monolayer graphene's Seebeck coefficient as a function of the gate voltage at different temperatures. The curves cross at the charge neutral point. Figure from Ref. [87]

Assume a graphene-based device with charge carriers heated by light illumination. According to the Seebeck effect, it is expected a thermal voltage signal is generated by the charge carrier diffusion corresponding to the temperature gradient. Next I will roughly estimate the magnitude of this thermoelectric signal and calculate the voltage responsivity, which is defined as the thermal voltage divided by the absorbed power. For simplicity, a purely diffusively cooled device is assumed, where the electron-

phonon coupling and other details of the device are ignored at this level, and the cooling is due to diffusion of electrons to the leads. According to Eqn. (2.19), a temperature difference  $\Delta T$  results in a voltage  $V = -S \Delta T$ . In addition, based on the Wiedemann Franz law, graphene's electron thermal conductivity is written as:

$$\kappa = L\sigma T \quad (2.21)$$

where  $L$  is the Lorentz number, thus, the steady state heat flux can be expressed as:  $Q = \kappa \Delta T$ . Then *Responsivity*  $\equiv |V/Q| = (1/\sigma E_F)(d\ln\sigma/d\ln E_F) \approx 2/\sigma E_F$ . The responsivity is maximized at small  $E_F$  and small  $\sigma$ . In realistic devices these quantities are limited by disorder; for graphene on SiO<sub>2</sub> the minimal values are roughly  $\sigma = 0.2$  mS and  $E_F = 50$  meV [50, 88], giving a maximum responsivity of  $2 \times 10^5$  V/W. This compares favorably with the commercially available room-temperature photodetectors, especially those working in THz range [14], such as pyroelectric detectors and Golay cells as introduced in Chapter 1. Notice that the responsivity is derived from a pure diffusive device. Practically, phonon scattering is accompanied with the carrier diffusion into the electrodes. Optical phonons of graphene [43] and remote surface polar phonons [89] (for SiO<sub>2</sub> substrate) emission play a role in visible/near IR excitation. For long wavelength radiation, carriers are scattered by graphene's longitudinal acoustic phonons. One can evaluate its effect on the responsivity of a graphene photothermoelectric detector by means of the carrier diffusion length, which is defined as  $\xi = \sqrt{\kappa/G}$ , where  $\kappa$  is the electron thermal conductivity as shown in Eqn. (2.21) and  $G$  is the electron-phonon thermal conductance. A theoretical calculation of  $G$  for mono- and bi-layer graphene is shown in Ref. [90]. Ref. [83] shows that the diffusion length of graphene with reasonable mobility at room temperature is  $\sim 7$   $\mu\text{m}$ , which is very favorable for realizing diffusively cooled devices at room temperature. However, more recently it was pointed out that disorder-assisted electron-phonon scattering may be important in graphene and in fact may dominate the hot electron cooling in low mobility graphene devices [91-93]. Traditional electron-phonon

scattering requires the momentum conservation, resulting in a severe constriction of the energy transfer due to a small Fermi surface size. In contrast, disorder-assisted scattering allows for arbitrarily large momentum of the emitted phonon. The entire thermal distribution of phonons can contribute to hot carriers' relaxation, resulting in a more efficient energy transfer per collision, which is called supercooling. In this case, the diffusion length is expressed as  $\xi = \sqrt{\kappa/G_{sc}}$ , where  $G_{sc}$  is the thermal conductance to the lattice due to supercooling.  $G_{sc}$  is strongly dependent on the disorder density and is proportional to  $T^2$  [92]. Several recent experiments have shown that the diffusion length of a graphene device with disorder is less than 1  $\mu\text{m}$  at room temperature [92, 93], suggesting that to optimize the responsivity of a graphene based thermoelectric detector, the channel length of the graphene element should be confined to  $\sim \mu\text{m}$  level.

### 2.3.3 Bolometric effect

As another photodetection mechanism, the bolometric effect relies on the temperature dependence of the material's electrical resistance. The device is biased to show a current change when it is heated by the electromagnetic radiation.

The efficient thermal decoupling of electrons from the lattice and the small electron specific heat of graphene realize large light-induced changes in electron temperature, making graphene as a good potential candidate of sensitive and high speed bolometer. However, the temperature dependence of mono-layer graphene's electrical resistance is weak, strangling the application of the bolometric effect. Several techniques are applied to achieve a temperature-dependent resistivity. One example shown in Fig. 2.10a is a dual-gated bilayer graphene device characterized by Yan et al. (Univ. of Maryland) [94]. Unlike the linear dispersion relation of monolayer graphene, bilayer graphene shows a quadratic dispersion relation with zero bandgap. Moreover, if there is an external electric field perpendicular to the bilayer

sheet, the inversion symmetry in the graphene plane will be broken and a bandgap will be opened subsequently [95], resulting in a temperature-dependent resistance induced by the insulating state. The photoresponse is characterized at low temperature with a biased dc current as shown in Fig. 2.10b. The radiation source is a 658-nm laser. The optical and electrical responsivity of the device exceeds  $1 \times 10^3$  V/W (referred to the power of the incident radiation) and  $2 \times 10^5$  V/W (referred to the absorbed power), respectively. Other work [96] in disordered graphene bolometer shows even higher responsivity (optical:  $1.6 \times 10^5$  V/W and electrical:  $6 \times 10^6$  V/W) at 1.5 K.

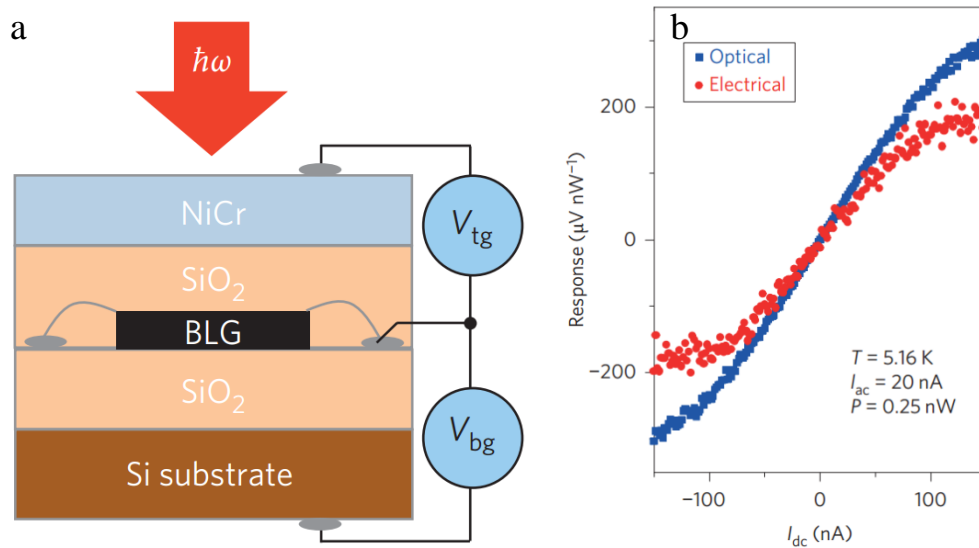


**Figure 2.10** (a) Schematic of a dual-gated bilayer graphene device and electric-field-effect gating. (b) Optical (blue) and electrical (red) responses as a function of dc current at  $T = 5.16$ K. Figure from Ref. [94]

Lastly, I compare different photodetection mechanisms in graphene: The photovoltaic detector is predicted to work in a broad temperature range, although the sensitivity could be temperature dependent [80, 81]. There is a lack of experimental evidence to show the photovoltaic detection speed. For a doped graphene device with Fermi energy  $E_F$ , there is a threshold photon energy  $2E_F$ , below which the electron-hole pair will not be generated because the interband transition is forbidden. In contrast, the photothermoelectric detector's responsivity is independent of the

excitation energy. In principle, the radiation wavelength can be extended to arbitrarily large value. The sensitivity is high and independent of the temperature for a pure diffusive device. The response is predicted to be fast due to the extremely small electron specific heat. Similar to the photothermoelectric detector, a graphene bolometer also covers a broadband detection range with high sensitivity and fast speed. However, it usually relies on a more complicated device structure, and more importantly, it requires a temperature-dependent electrical resistance, which has so far only been realized at cryogenic temperature in graphene, limiting its application at room temperature. In summary, I found the photothermoelectric effect to be the most promising mechanism to make a graphene based room-temperature broadband photodetector. In following chapters I will discuss how to experimentally realize such detectors, and characterize their performance.



## Chapter 3: Experimental techniques

In this chapter, I summarize the device fabrication processes as well as the experimental set-ups used for characterizing the devices' electrical and optical properties. Section 3.1 mainly focuses on device preparation. I first explain how to obtain and identify monolayer graphene. Then the processes for fabricating electrical contacts are introduced, especially the shadow evaporation technique, which is applied for making most of the devices in this project. In Section 3.2 I introduce the electrical transport measurement set-up, which is used to characterize the device's electrical conductivity as a function of the gate voltage, as well as the device's thermoelectric response to Joule heating. Starting from Section 3.3, I will describe experimental set-ups for characterizing the optical response of the devices. Continuous wave laser sources are used in the set-up introduced in Section 3.3 for dc photoresponse characterization, while pulsed laser sources are applied in Section 3.4 for measuring the response time of the devices. The laser scanning microscope (LSM) is introduced in Section 3.5, which is capable of scanning a focused laser spot across the sample to probe the photoresponse of each part of the device. Last, in Section 3.6 I will briefly explain the operation principle of the Fourier transform infrared spectroscopy (FTIR) and introduce the FTIR set-up used in this project to characterize the transmission spectra of large area graphene devices.

### 3.1 Graphene photodetector fabrication

#### 3.1.1 Preparation and characterization of monolayer graphene

There are three main techniques to obtain monolayer graphene samples, i.e. exfoliation from the bulk graphite, epitaxial growth on SiC substrates, and chemical

vapor deposition (CVD) on metallic foil, all of which were used in my experiments. I will briefly review each technique next.

As described in Section 1.2, graphene consists of carbon atoms, which construct hexagonal lattices in the two dimensional plane. Neighboring atoms are connected through robust covalent bonding. Graphite is composed of many layers of graphene, which are bonded by weak Van der Waals forces. Therefore, a top-down technique can be applied here by repeatedly cleaving thick graphite to get thin layers. A well-known technique for exfoliating thin single crystals using an ordinary Scotch tape is used in my experiment, pioneered by Novoselov et. al (Univ. of Manchester) in 2005 [97]: Bulk Kish graphite is mechanically exfoliated using Scotch tape repeatedly until the tape is covered with flakes of graphite. The area containing thin layers of freshly exposed graphite is then pressed onto a low doped Si ( $100 \sim 250 \Omega \cdot \text{cm}$ ) substrate with 300 nm  $\text{SiO}_2$  on top as insulating layer. As the last step, the tape is removed and it is possible that monolayer graphene is left on the substrate, since the Van der Waals force between the substrate and the bottom layer of thin graphite may be slightly larger than the Van der Waals force between graphene layers. The size of exfoliated graphene is usually a few microns to a few tens of microns. It is worth emphasizing that the thickness of  $\text{SiO}_2$  is selected to be 300 nm, in order to enhance the interference of visible light and provide good optical contrast for thin films on it [97]. The optical micrograph helps to tell the layer number of the graphene flake, as shown in Fig. 3.1a. However, the contrast of the image may depend on the light source, the white balance of the image, and how well the light is focused. Therefore, to accurately characterize the layer number of the flake, Raman spectroscopy is usually applied [98]. As shown in Fig. 3.1b, the Raman spectra for graphene or graphite contain two characteristic peaks: a peak at  $\sim 1580 \text{ cm}^{-1}$ , which is called the G peak, and a peak  $\sim 2700 \text{ cm}^{-1}$ , which is called the 2D peak. The 2D peak of monolayer graphene is a single Lorentzian lineshape (as shown in the inset of Fig. 3.1b), whereas

for bilayer graphene the 2D peak is composed of four Lorentzian peaks, and multiple Lorentzian components for even thicker flakes.

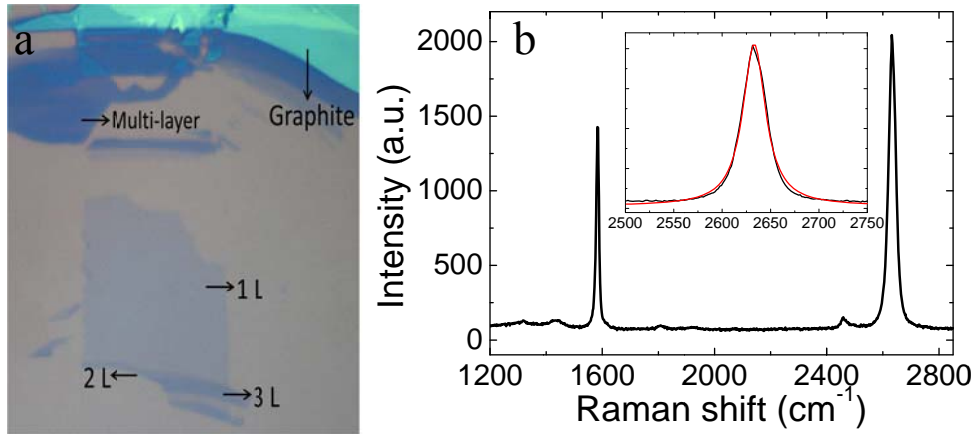


**Figure 3.1** (a) Optical micrograph of an exfoliated graphene sample. (b) Raman spectrum of monolayer graphene. Inset: Lorentzian fit (red line) to the 2D peak (black line) of the Raman spectrum of monolayer graphene.

Compared to the top-down exfoliation technique, CVD and epitaxial growth are both bottom-up techniques capable of producing large area monolayer graphene. The CVD-grown graphene used in this project is purchased from *Graphene Supermarket*, which follows steps reported in Ref. [99] to grow uniform monolayer graphene on copper foil and then transfer the film to a low doped silicon substrate using the technique reported in Ref. [100]. Fig. 3.2 shows the optical micrograph and the Raman spectrum of a CVD-grown graphene sample. It is found in Fig. 3.2a that CVD-grown monolayer graphene can cover the whole substrate. However, its quality is generally lower than exfoliated sample, due to defects, chemical residues, ripples, tears, holes, etc. Those disorders are reflected in the Raman spectrum as a peak  $\sim 1350$  cm<sup>-1</sup>, which is called D (disorder) peak, as shown in Fig. 3.2b; this peak is activated only by point disorder which mixes the two valleys in graphene.

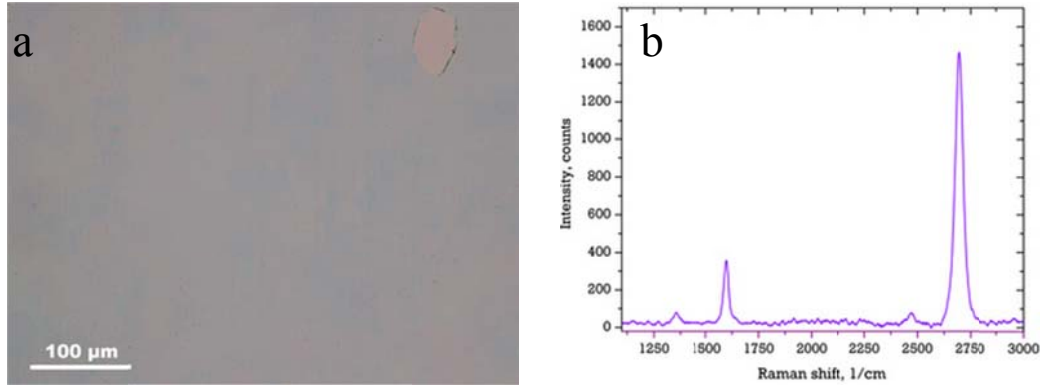


**Figure 3.2** (a) Optical micrograph of CVD-grown monolayer graphene on SiO<sub>2</sub>. (b) Raman spectrum of CVD-grown monolayer graphene.

Another technique to get large area monolayer graphene is to prepare it epitaxially on single-crystal SiC. Heat treatment of the SiC causes sublimation of Si and reconstruction of the carbon-rich surface to form graphene layers. In the case of the samples used here, the detailed growth process can be found in Ref. [101]. Briefly, the starting substrate is SiC (0001) which is semi-insulating (resistivity  $> 10^9 \Omega \cdot \text{cm}$ ). The substrates are placed in an argon ambient under controlled temperature, pressure and flow conditions to produce large area uniform graphene.

It is difficult to observe monolayer graphene on SiC optically, since the substrate is optically transparent. Fig. 3.3 shows the Raman spectrum of a SiC-graphene sample, which is used in following experiments. Graphene's 2D peak can be clearly observed in the Raman spectrum, while the G peak is overlapped with the two-phonon spectrum of the substrate [102-104] as shown in Fig. 3.3a. According to Ref. [102, 103], one can subtract the spectrum of a bare substrate from the epitaxial graphene's spectrum to get the pure response of graphene, as shown in Fig. 3.3b. A good fit of the 2D peak to a single Lorentzian (inset) verifies the single-layer nature of the sample. The notable D peak around  $1400 \text{ cm}^{-1}$  indicates the sample is disordered. There are some other features between the D peak and G peak, which are also observed in Ref. [104] and are possibly due to the interfacial  $\text{sp}^2$  carbon layer

between graphene and SiC, however, there is a lack of detailed discussion about this in the literature.

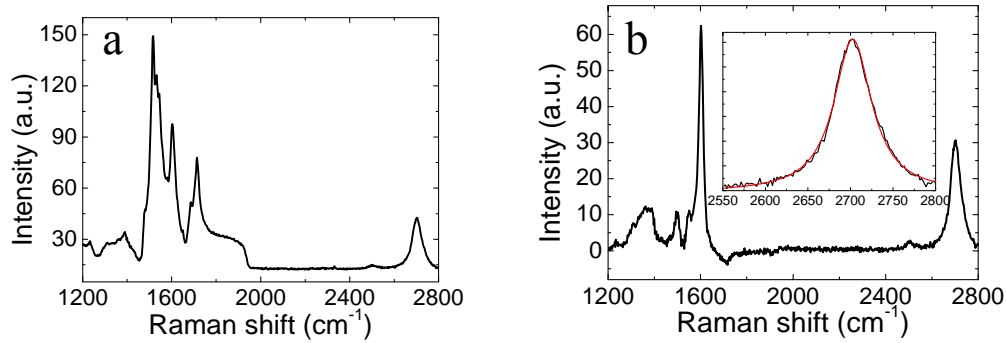


**Figure 3.3** (a) Raman spectrum of a monolayer epitaxial graphene on SiC. (b) Raman spectrum of the same device shown in (a) with the background response subtracted. Inset: Lorentzian fit to 2D peak.

### 3.1.2 Photodetector fabrication – shadow evaporation technique

The photodetector devices are fabricated using a standard electron beam lithography technique.

Firstly, I will explain how to fabricate devices with exfoliated graphene and introduce the shadow evaporation technique. Detailed recipes and optical micrographs of devices in progress are provided in Appendix A. The fabrication process starts with locating alignment markers near the target monolayer graphene flake: A bilayer e-beam resist [methyl methacrylate (8.5%)/methacrylic acid copolymer (MMA), Micro Chem Corp.; and poly(methyl methacrylate) (PMMA), Micro Chem Corp.] is spun onto the substrate (see Appendix A for recipe). A “cross” far away from the flake is then exposed by the electron beam. Afterwards, the sample is developed in PMMA and copolymer resist developer (IPA/MIBK 3:1, Micro Chem Corp.) for 45 seconds to remove the resist in the “cross” area. The “cross” is regarded as a coordinate base to roughly define the position of the graphene flake using an optical microscope equipped with digital coordinate readout. The sample is then

inserted back into a SEM converted E-beam chamber (*FEI XL-30*). The “cross” is found through SEM imaging and the sample is moved to the position, where the graphene flake should be located, by the SEM mechanical stage. Usually, two sets of alignment markers are written subsequently using the *Nanometer Pattern Generation System* (NPGS) software control. The developing process is then repeated to remove the resist in the patterned area to show alignment markers. As will be shown in the next paragraph, with the assistance of the first set of the developed alignment markers, one will be able to fix the position of the graphene flake and write the pattern for metal electrodes deposition. When aligning the sample with the first set of alignment markers, the e-beam resist in the area around the markers can be overexposed or even crosslinked. Therefore, should the aligning process be repeated in the future, the second set of alignment markers will be used.

The next step is to deposit metal electrodes, which contact to graphene and serve as part of the device. For a typical photodetector, at least two electrodes are needed (one as the signal output and the other is grounded). It will be shown in following chapters that it is essential to make the device asymmetric, so as to generate a net electrical signal even with uniform light illumination and zero bias current. In this project, the asymmetry in the device is realized via using different metal contacts. The traditional approach to deposit various metal electrodes is to repeat the e-beam writing and the subsequent metallization several times for each metal. One example is shown in Fig. 3.4: Firstly, the leads-like structures are patterned on the resist using e-beam lithography, followed by a thermal evaporation of Au/Cr (4 nm/ 45nm) in high vacuum conditions ( $<10^{-6}$  Torr). The metalized sample is then put in acetone for few hours to lift off the resist. The same process is repeated two times more to deposit pure chromium (20 nm) electrodes on the left side and pure gold (25 nm) electrodes on the other side.

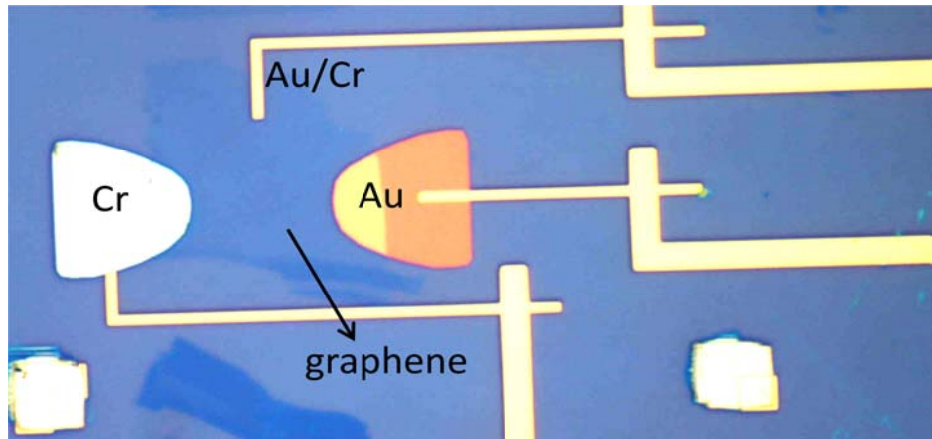


**Figure 3.4** Optical micrograph of an exfoliated graphene photodetector device with three different metallic probes (Cr, Au and Au/Cr).

Repeated lithography processes increase the risk of damaging the sample and have more chance to induce residues on graphene surface or near contacts, sacrificing the quality of the device. Therefore, in most devices tested in this project, a shadow evaporation technique is applied, in order to realize dissimilar metal-contacted device with one lithography step [105]. Fig. 3.5 shows the schematic of lithographic steps to do shadow evaporation: PMMA/MMA double layer resist is spun onto the substrate (see Appendix A for recipe). MMA is the copolymer of PMMA with low-molecular-weight and is more sensitive to the electron beam than PMMA. Therefore, an undercut shown in Fig. 3.5b can be achieved by slightly increasing the dosage when exposing the pattern to the electron beam. Successive angled evaporations of chromium (red arrows) (Fig. 3.5c) and gold (yellow arrows) (Fig. 3.5d) using a rotating sample holder in the thermal evaporator chamber followed by liftoff produce a single-layer graphene device with dissimilar metal contacts on the opposing sides as shown schematically in Fig. 3.5e. Fig. 3.5f shows the optical micrograph of the electrical contacts of the photodetector and the inset is a zoomed-in image of the light sensitive part (bimetallic contacts connected to the exfoliated graphene flake) of the device taken via atomic force microscopy.

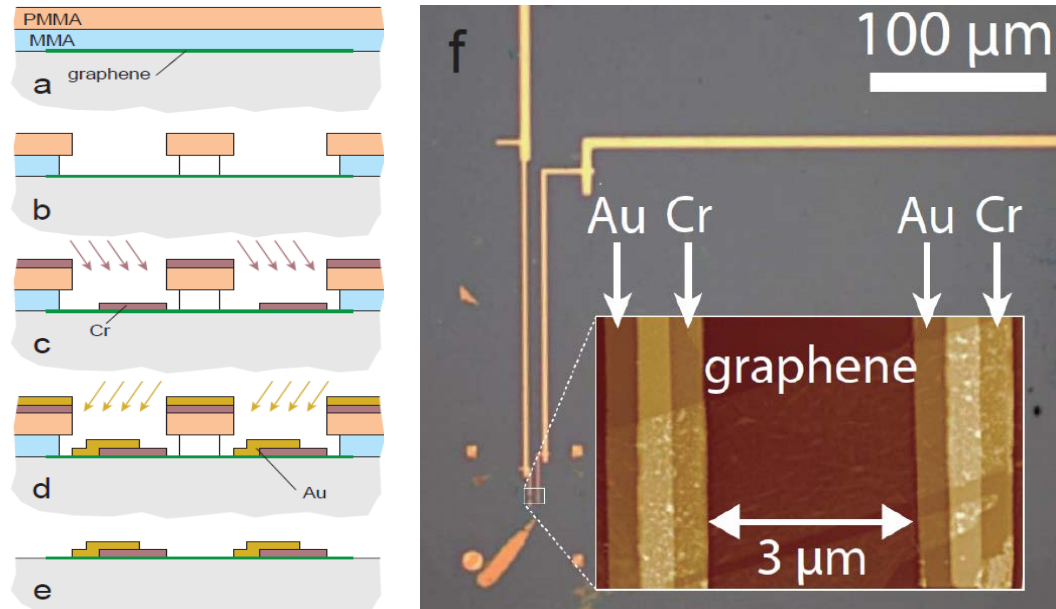


**Figure 3.5** (a-e) Lithographic steps of the shadow evaporation technique, as described in text. (f) Optical micrograph of the device. Inset: AFM image of the graphene flake contacted with dissimilar metal electrodes.

Sometimes the monolayer graphene flake is directly connected with multilayer graphene sheets or there is a special requirement for the graphene flake's geometry. In these cases, a final lithographic step is needed to etch graphene flake into some special shape. Etch masks are prepared by similar electron-beam lithography and resist developing techniques as described before except that only PMMA is used as the resist to achieve better resolution. Oxygen plasma (300 mTorr) is used in a dry etching system (*Technics PE-IIA*) to remove the portion of graphene which is not protected by the mask (see Appendix A for recipe). The resist mask is removed in acetone afterwards, leaving the mask pattern transferred to the graphene flake.

CVD- or SiC-grown graphene is usually used to fabricate large area device in this project. The fabrication technique is slightly different from above for the exfoliated graphene due to the fact that graphene covers the whole chip: First, the device can be fabricated anywhere on the substrate and the precise alignment is unnecessary since the device's size is large, so in many cases, the patterning of alignment markers can be omitted. Second, it is essential to isolate the region where



the device is planned to be fabricated from the rest of graphene, in order to avoid the detector being electrically shorted by the conducting graphene layer on the substrate. Therefore, at the very beginning of the fabrication, an etch mask is usually prepared to create a graphene island for further treatment. (Note that some large area devices also need alignment markers. In such cases, alignment markers will be patterned first, followed by the metal deposition. The positioning of the graphene island is determined with the assistance of the metalized alignment markers afterwards.)

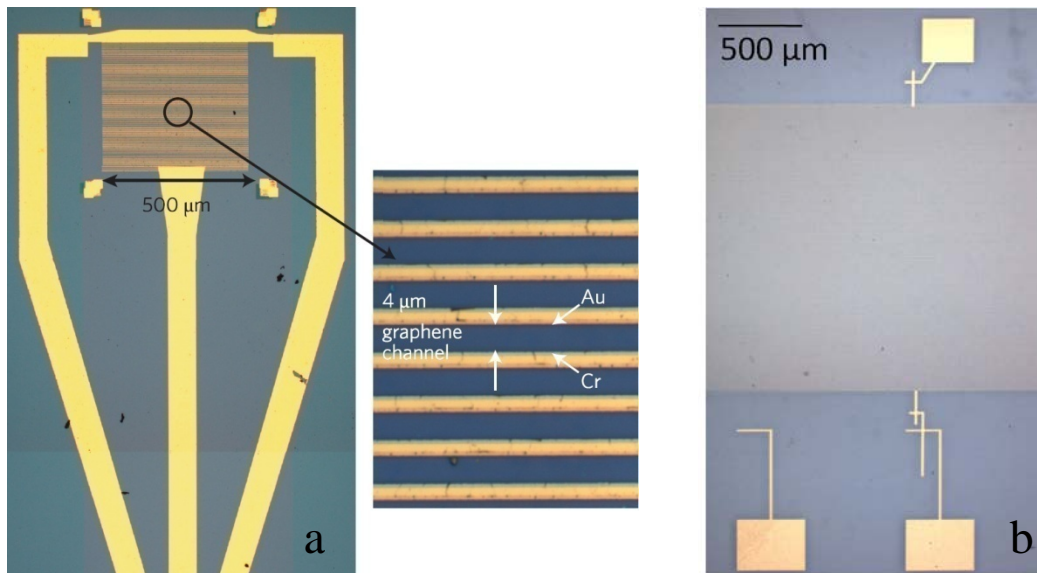


**Figure 3.6** (a) A photodetector based on CVD-grown graphene on  $\text{SiO}_2$  substrate. (b) A photodetector based on epitaxial grown graphene on SiC substrate.

Figure 3.6 shows two examples of large area graphene photodetectors. Fig. 3.6a presents a device based on CVD-grown graphene that is used for the time-domain THz response characterization. Many graphene channels (light sensitive part) are connected in series with dissimilar metal contacts (established using the shadow evaporation technique described above) to enhance the response and the electrodes are designed to be optimized for a time-domain measurement. Detailed information will be shown in following chapters. Fig. 3.6b shows a graphene photodetector prepared on SiC substrate. Similar to the one shown in Fig. 3.6a, many graphene channels are connected in series. When using as a detector, the top pad will be

grounded and the bottom right pad serves as a signal output. One thing to be pointed out is the function of the bottom left pad, which is isolated from the light sensitive part of the detector: Since SiC is an insulating material, the back gating technique does not apply to the device shown here. To tune the carrier density in the graphene sheet, a polymer electrolyte top gate is prepared. To prepare the electrolyte,  $\text{LiClO}_4$  and polyethylene oxide (PEO) are mixed in the weight ratio 0.12:1, and the mixture is dissolved in methanol. A sharp wood stick is used to put a small droplet on the device, which covers the whole light sensitive part of the device and most area of the metal pad in the bottom left of Fig. 3.6b. The top gate voltage is then applied to the naked part of that pad, pushing or pulling the mobile ions ( $\text{Li}^+$ ) in the electrolyte. The resulting high capacitance of electrochemical double layer formed between surface of the sample and accumulated ions can tune the carrier density in graphene over a wide range [51].

### 3.2 Transport measurement set-up

The transport properties of graphene photodetectors are characterized by a dc/ac set-up using a dc source&meter (*Keithley 2400*)/lock-in amplifier (*SR 830* or *EGG 7260*). The schematic is shown in Fig. 3.7. A two-probe dissimilar metal-contacted device is taken as an example: One electrode (drain) is grounded and the other (source) serves as the bias input. The substrate is connected to a *Keithley 2400* for applying the gate voltage to tune the carrier density of graphene. Another *Keithley 2400* can be directly connected to the device as a tunable dc bias voltage source and it measures the dc current through the device simultaneously, in order to measure the  $I$ - $V$  characteristic of the device. In comparison, a lock-in amplifier generates sinusoidal current flowing through the device, and measures the voltage whose frequency matches that of the excitation signal. When using the lock-in amplifier to characterize the device, a divider resistor  $10\text{ M}\Omega$  (or  $1\text{ M}\Omega$ , which is much larger than the

resistance of the device) is connected in series with the voltage source, so that the current through the device is primarily determined by the source bias and the divider resistor. The error can be neglected as long as the device's resistance is much less than the divider's resistance, which is always true for devices characterized in this project, unless otherwise specified. The source bias is also taken as a reference signal inside the amplifier to lock the frequency. The voltage difference between device's two probes at the same frequency as the source bias (also called the first harmonic) is measured using the lock-in differential inputs A and B, in order to characterize the electrical conductivity of the device. The lock-in amplifier also allows a second harmonic readout, which means the voltage difference between device's two probes at  $2f$  (assuming the source bias frequency is  $f$ ) can be measured as well. This is useful for device's characterizing the thermoelectric response of the device to Joule heating, which will be shown later. It is useful to point out a switch box is used to bridge the device and the external electronics to protect the electrically fragile device. This method is adopted in all measurements in this project, unless otherwise specified.

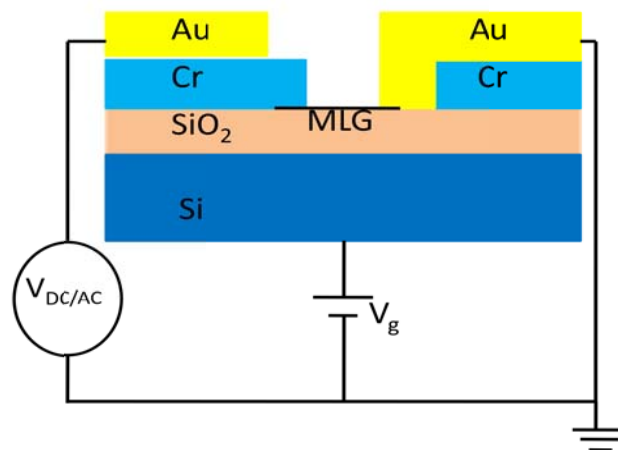


**Figure 3.7** Schematic of the transport measurement set-up of a bi-metal contacted graphene photodetector on SiO<sub>2</sub>/Si substrate.

### 3.3 DC photoresponse measurement set-up

There are different techniques to characterize the photoresponse in a detector. First I will discuss the dc photoresponse, the steady state average amplitude of the signal is concerned (ignoring the transient response, or how the signal is built up right after the device is illuminated by the light).

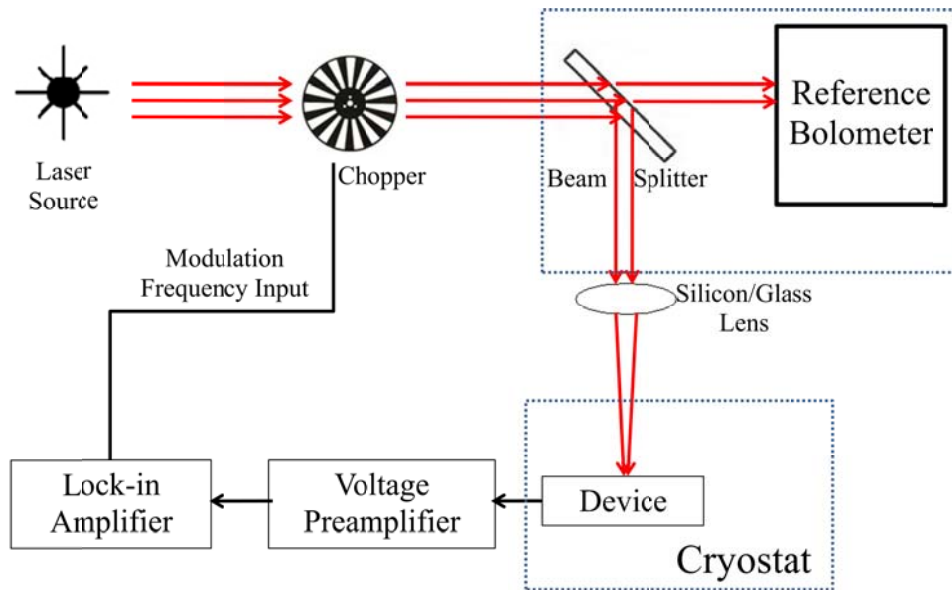


**Figure 3.8** Experimental set-up for broadband dc photoresponse characterization

Fig. 3.8 shows the experimental set-up used in this project to characterize the broadband dc photoresponse in graphene photodetectors. Three different laser sources are used to excite the response: 1. A continuous wave (CW) THz laser, which is optically pumped by CO<sub>2</sub>-laser resonator with methanol (CH<sub>3</sub>OH) or methanol-D (CH<sub>3</sub>OD) vapors. The frequency of the laser depends on the cavity parameters of the CO<sub>2</sub>-laser resonator and the type of the vapor. Two main lines used in the project are 2.5 THz (84 cm<sup>-1</sup>) and 5.3 THz (175 cm<sup>-1</sup>). The power of the beam for both lines is 10 – 20 mW; 2. *81663A Distributed Feedback Laser Source (Keysight Technologies)*. This is a CW near infrared laser with wavelength 1.55 μm and a maximum output power ~ 20 mW. The output is coupled to optic fibers in the experiment; 3. *Menlo*

*Systems C-Fiber 780 Fiber Lasers.* This is a fiber laser system with 780 nm and 1.56  $\mu\text{m}$  outputs. The custom 1.56  $\mu\text{m}$  output is used in the measurement. Unlike previous two laser sources, this system provides pulsed excitations with the pulse width  $\sim 60$  fs and the repetition rate 100 MHz. The average power of the beam can be tuned up to  $\sim 50$  mW. The photoresponse is characterized by illuminating the detector with a chopped laser beam and detecting the open-circuit photovoltage signal using a voltage preamplifier and lock-in amplifier. The detecting frequency of the lock-in amplifier is locked by the chopper's rotating frequency input. The reason for chopping the laser is to apply the lock-in technique, in order to read the signal at the selected frequency, avoiding background noise from other frequencies. The beam is focused on the detector using a glass lens (for near-IR excitation) or a Si lens/a gold paraboloid (for THz excitation) with the beam size a few hundred microns in diameter. For some devices (especially those covered by the electrolyte top gate on the front surface), the radiation is sent from the back side of the substrate to enhance the absorption. For THz photoresponse characterization, a beam splitter is mounted to take part of the radiation into a reference bolometer, which is used to monitor the power intensity of the source, since the THz laser is very sensitive to humidity, environmental temperature, and any mechanical vibrations. For the near-IR pulsed excitation, the device is mounted in a continuous flow cryostat system (*Janis Research*) to characterize the temperature dependence of the photoresponse from room temperature down to  $\sim 10$  K.

### 3.4 Time-domain photoresponse measurement set-up

This dc photoresponse setup is used to characterize the steady state responsivity of the device, which is defined as the magnitude of the signal divided by the radiation power, to CW excitation. For a pulsed excitation, the setup automatically averages the response in the time domain, measuring the average responsivity, i.e. the magnitude

of the signal divided by the average power of the source. Thus this setup loses information about the speed of the detector. New experimental set-ups were designed to characterize the response time of the graphene photodetectors as described below.

### 3.4.1 Experiment set-up for pulse coincidence measurement

One approach used in this project to characterize the response time of a photodetector is the pulse coincidence technique, which is also termed the asynchronous optical sampling (ASOPS) [106] method, with an ultrafast pulsed laser with wavelength  $1.56 \mu\text{m}$ , pulse width  $\sim 60 \text{ fs}$  and energy per pulse  $500 \text{ nJ}$  as pump and probe sources with maximum scan length  $10 \text{ ns}$  and scan resolution  $\sim 100 \text{ fs}$ .

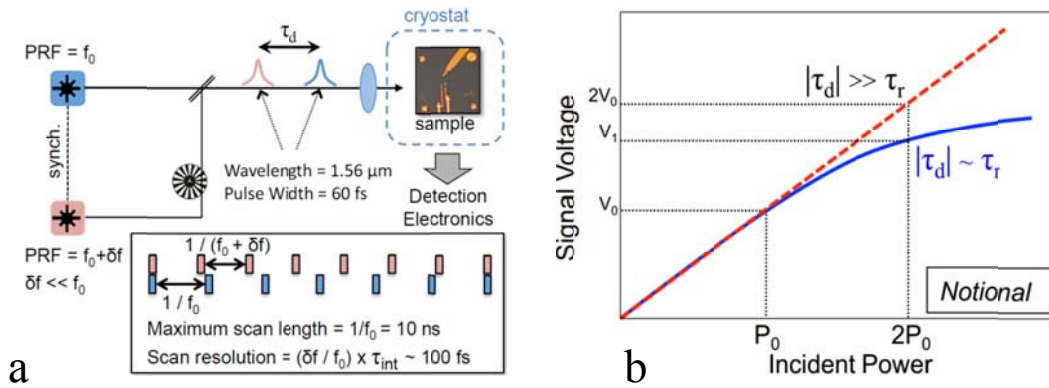


**Figure 3.9** (a) Experimental set-up for the pulse coincidence measurement. (b) Schematic showing the power dependence of a linear (red dashed line) and a sublinear (blue solid line) response.

As shown in Fig. 3.9a, the device is mounted in a cryostat. The repetition rate of the pump pulse is  $f_0 = 100 \text{ MHz}$ , which is slightly different from the probe pulse with a repetition rate  $f = f_0 + \delta f$ , resulting in an asynchronous illumination on the device. The detection electronics, as described in Section 3.3, measures the photovoltage for pump + probe pulses at each delay time. Consider a nonlinear device (sublinear) as shown in Fig. 3.9b: Assuming the power of each pulse is  $P_0$ , which can generate an average photoresponse  $V_0$  in the device in one repetition period, the total photovoltage  $V_t$  will be a function of the delay time  $\tau_d$ . If  $\tau_d$  is much larger than the

device's response time  $\tau_r$ , the device would have been relaxed from the first excitation when the second one arrives. In this case, each pulse generates  $V_0$  independently and the total signal is  $V_t = 2V_0$ . If  $\tau_d$  is comparable to or much smaller than  $\tau_r$ , then they can be regarded as one big pulse with the power  $2P_0$ . As shown in Fig. 3.9b, due to the nonlinear nature of the device, the total response then should be written as:  $V_t = V_1 < 2V_0$ . Therefore, one should be able to measure the response as a function of the delay time of pump and probe pulses to characterize the response time of the detector.

Compared to the direct time-domain measurements, which will be shown in the next section, there are several advantages of the pulse coincidence technique: 1. The signal measured is the dc photoresponse, therefore the lock-in technique is applicable, eliminating a lot of broadband pick-up noise. 2. There is no requirement for very high pulse energy, since even a tiny signal can be accurately characterized with the assistance of a voltage preamplifier and the precise readout of the lock-in amplifier. 3. The measurement of a fast response (for graphene detectors, the response time is as small as  $\sim 10$  ps) is transferred to a quasi-dc measurement, so the upper limit determined by the bandwidth of the equipment does not make a restriction anymore. However, this technique requires nonlinearity in the device to show a different magnitude of the response when two pulses overlap each other, which is a drawback if the device is linear.

### 3.4.2 Broadband direct-time-domain-readout photoresponse measurement set-up

As discussed in previous section, the pulse coincidence technique characterizes the intrinsic response time of the device, which is solely determined by the speed of the thermal process in graphene, showing the physical limit of the device's response time. The speed of a real device relies not only on the intrinsic response time, but is limited by e.g. the  $RC$  time constant of the device and leads as well. Therefore, to characterize the extrinsic response time, which includes the time constant of each part

of the circuit, will be technologically more relevant. The time-domain readout of the photoresponse shows a direct measure to the extrinsic response time of the device.

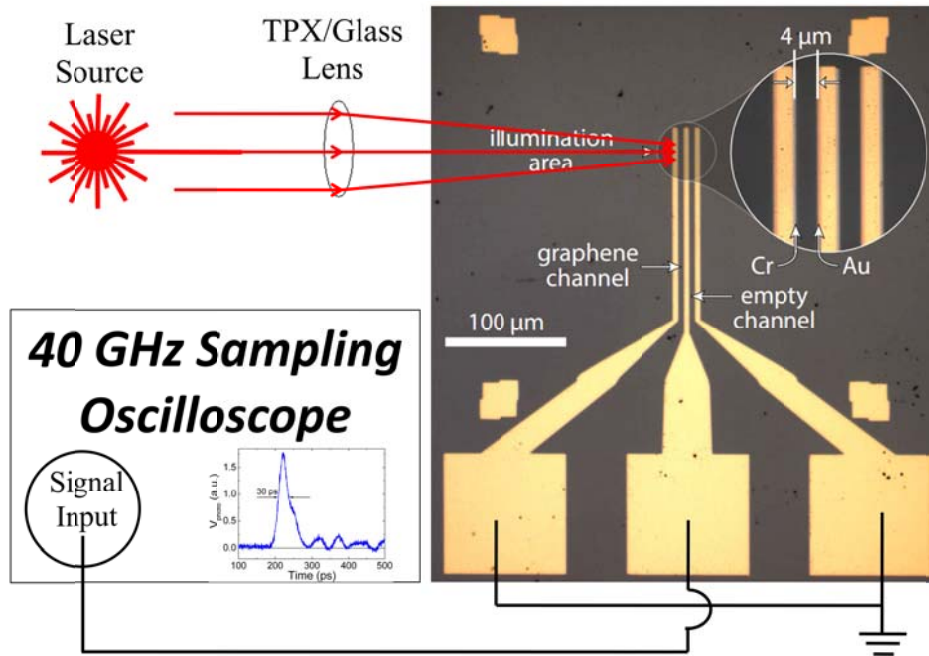


**Figure 3.10** Experimental set-up for time-domain photoresponse characterization.

As shown in Fig. 3.10, the selected laser source is *Coherent Libra Amplified Ti:Sapphire Laser*, which is a mode-locked laser oscillator with an amplifying stage that increases the pulse energy, enhancing the magnitude of the response in the time domain measurement, and reducing the pulse repetition frequency. The wavelength of the pulsed laser beam is 800 nm, with the pulse width  $\sim 50$  fs, repetition rate 1 kHz. The maximum energy per pulse can be very high, but it is attenuated to 250 nJ per pulse in my experiment to protect the sample. Broadband THz pulses can also be produced in this system through optical rectification of femtosecond pulses in a lithium niobate prism [107]. The generated THz pulses have duration  $\sim 1$  ps and a spectrum spanning 0-2 THz (peaked around 0.3 THz) with a pulse energy of  $\sim 160$  nJ at a repetition rate of 1kHz. The beam is focused on the device through a glass lens for optical excitation and a polymethylpentene (TPX) lens for THz excitation,



reaching a spot size of a few microns and approximately 1 mm for optical and THz radiations, respectively.

A typical device for direct time domain readout is shown in Fig. 3.10, whose leads are designed to be very symmetric, in order to avoid picking up noise from the environment. The pads of the device are contacted by a three-tip radio-frequency ground-signal-ground probe. The output photoresponse signal is recorded using a high speed (bandwidth = 40 GHz) sampling oscilloscope.

### 3.5 Scanning photocurrent measurement set-up

The scanning photocurrent measurement set-up is built mainly based on a confocal laser scanning microscope (LSM), which images the device and illuminates it with a sharply focused laser beam simultaneously, and is therefore able to determine the photoresponse of each part of the device.

As shown in Fig. 3.11, a focused laser spot of nominally 1  $\mu\text{m}$  diameter is scanned over the sample using a set of two galvano-mirrors. A long working-distance objective lens is used to focus the light onto and to gather the reflected light from the sample. The reflected light is directed to a Si photodiode, which measures the reflected light at each pixel. In addition, part of the beam is taken into a CCD camera, so that one can easily view the relative position of the beam spot to the sample [108]. The wavelength of the source is 638 nm in this experiment and the photodetection electronics is the same as described in Section 3.3. The sample is fixed in a chip carrier with silver paint.

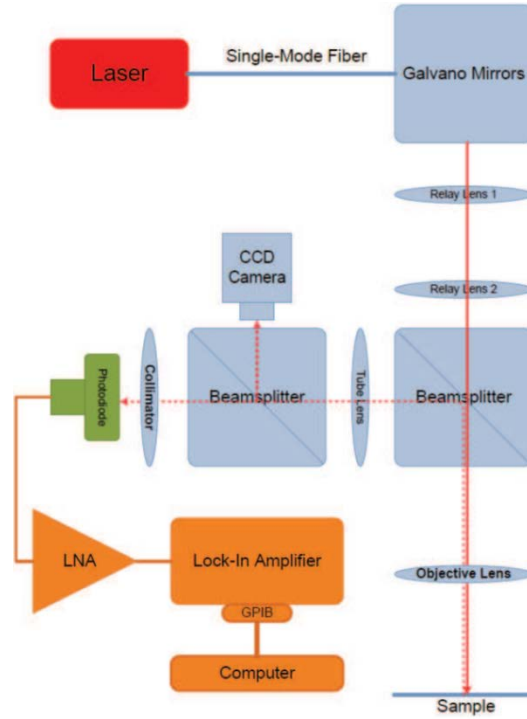


**Figure 3.11** Experimental set-up for scanning photocurrent measurement.

### 3.6 Fourier transform infrared spectroscopy set-up

Fourier transform infrared spectroscopy (FTIR) [109] is a powerful technique in optics to obtain an infrared spectrum of absorption, transmission, reflection, emission or photoconductivity of a solid, liquid or gas. An FTIR spectrometer simultaneously collects high spectral resolution data over a wide spectral range. In this project, the FTIR technique is used to extract the transmission information of various graphene-metal nanostructures in the far infrared range, which is very useful in determining the absorption of the device, and thus the intrinsic responsivity (referred as the signal per unit absorbed power) of a photodetector.

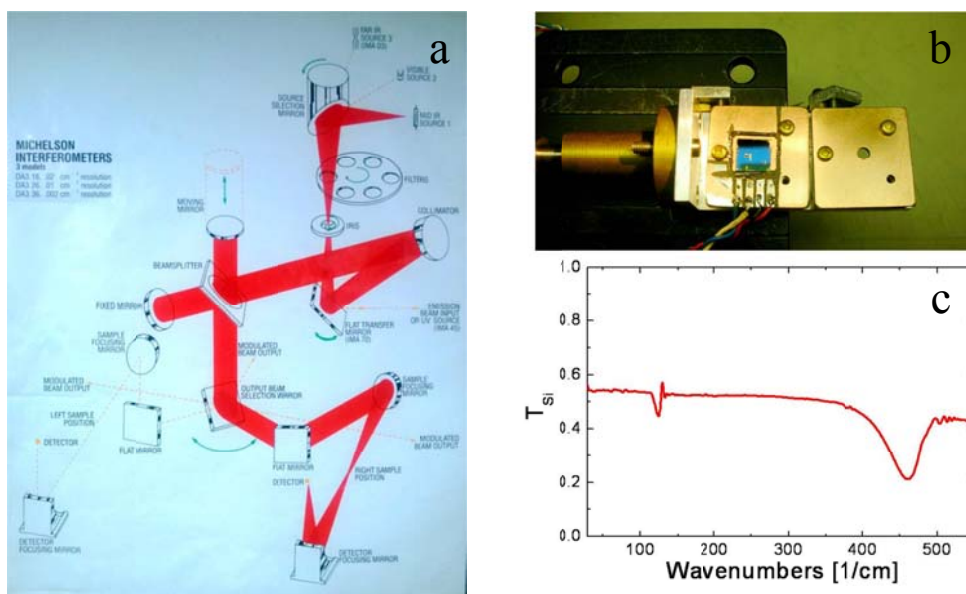


**Figure 3.12** (a) Experimental set-up of a FTIR system. (b) Photograph of two copper plate sample holders, one with a sample on top (left) and another used as reference (right). (c) Transmission spectrum of a SiO<sub>2</sub>/Si substrate.

Figure 3.12a shows the schematic of the operation in a typical FTIR system. In this project, far infrared transmission measurements are performed in a *BOMEM DA-8* FTIR system with mercury lamp as a source. The key component of the system is a Michelson interferometer: Light from the polychromatic infrared source (mercury lamp) is collimated and directed to a beam splitter. Ideally 50% of the light is refracted towards the fixed mirror and 50% is transmitted towards the moving mirror. Light is reflected from the two mirrors back to the beam splitter and 50% of the original light passes into the sample compartment. As the mirror moves, each wavelength of light in the beam is periodically blocked and transmitted by the interferometer, due to the interference effect. Different wavelengths are modulated at different rates, generating different spectrum at each moment. The light intensity (e.g. the transmission through the sample) is recorded as a function of the time (corresponding to the mirror position). Then the computer takes all these data and do a Fourier transform backwards to infer the light intensity at each wavelength. The device, which is usually designed to be slightly larger than  $2 \times 2 \text{ mm}^2$ , is mounted on

a copper plate (shown in Figure 3.12b) with a 2 mm diameter aperture. The mounted sample is placed in vacuum at room temperature and is uniformly illuminated by the incident beam of 8 mm in diameter. The sample aperture is strongly overfilled to minimize spectrometer diffraction losses at low frequencies. Another copper plate with an identical aperture is aligned with the sample holder plate, which can be used to check the transmission, in order to monitor the power drift of the radiation source. Sometimes an electronically controlled rotating wire grid polarizer is placed in front of the sample to probe device's response at different polarizations. Finally, the transmission through the device is detected by a 4 K silicon composite bolometer.

Fig. 3.12c shows a typical transmission spectrum of a bare low doped Si substrate with double side polished SiO<sub>2</sub> (300 nm), which is used in this project to fabricate many devices. From 30 cm<sup>-1</sup> to 400 cm<sup>-1</sup>, ~50% of the beam power gets transmitted due to the reflection on silicon surface. Around 450 cm<sup>-1</sup>, there is a dip in the spectrum corresponding to the light-phonon interaction in SiO<sub>2</sub>. The feature around 120 cm<sup>-1</sup> is due to the pick-up noise from the environment. Since the spectrometer is calibrated such that 1 Hz = 1 cm<sup>-1</sup>, so this feature corresponds to 120 Hz noise.

## Chapter 4: Broadband photoresponse characterization of bi-metal contacted graphene photodetectors (CW excitation)

This chapter focuses on the broadband photodetection in exfoliated monolayer graphene devices on low doped silicon substrates. The shadow evaporation technique (as introduced in Section 3.1.2) is used to deposit dissimilar metal contacts for creating asymmetry, in order to generate a net response even with uniform illumination. The steady-state photothermoelectric response is measured from optical to far infrared range with CW excitation. The intrinsic and extrinsic responsivity and the noise equivalent power of the detector in THz range are characterized. The thermoelectric response is also characterized by the Joule heating technique, and compared with a diffusive model taking into account various asymmetric contact effects.

### 4.1 Scanning photocurrent measurement

As introduced before [76, 77], the scanning photocurrent technique has been a widely used method to probe the light-matter interaction in graphene, spawning interest in graphene-based optoelectronics devices. In previous works [76, 77] the local photoresponse was studied in graphene devices contacted with a single type of metal. In this work, similar measurements are performed on a bi-metal contacted graphene photodetector, in order to answer several questions: 1. Is there a photoresponse of the detector to uniform illumination? 2. How does each part of the device respond to the focused beam spot? 3. Is there any difference between the dissimilar metal contacts?

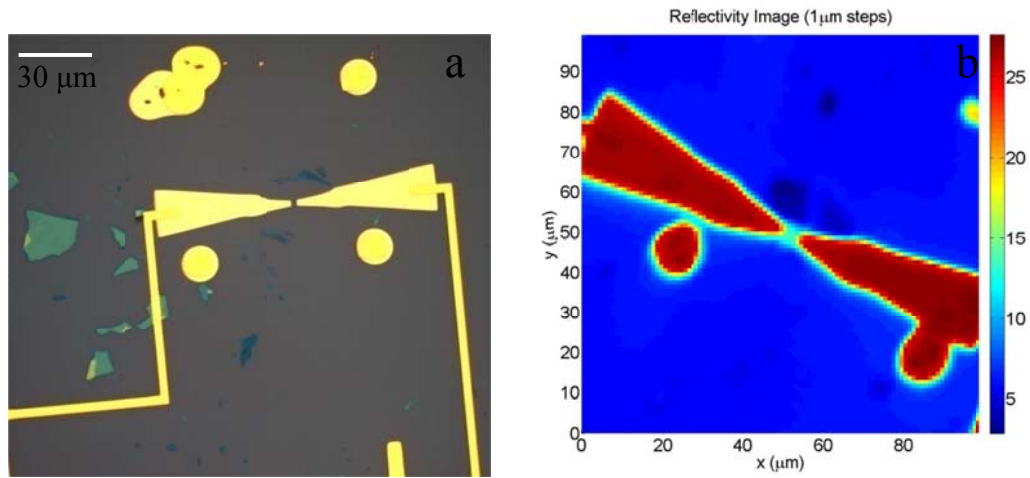


**Figure 4.1** (a) Optical micrograph of a bi-metal contacted graphene photodetector. (b) Reflectivity image of the device taken by the LSM system.

The optical micrograph of a device similar to the one measured in this experiment is shown in Fig. 4.1a. Exfoliated graphene is contacted with chromium on one side and gold on the other side using the shadow evaporation technique. The electrodes are patterned to have a bowtie antenna shape, which was originally designed to optimize the absorption to the long wavelength radiation and is irrelevant in this measurement, as the selected 638-nm CW laser source is not coupled to the antenna. Fig. 4.1b shows the reflectivity image of the real device taken by the LSM system with the beam focused to be  $\sim 2 \mu\text{m}$  in diameter. The red bowtie feature, corresponding to a high reflectivity region, represents the metal electrodes. The blue background is the Si substrate. Bi-metal contacts and single layer graphene sheet at the center are not well resolved in this picture, since the moving step of the beam is set to be  $1 \mu\text{m}$ , resulting in a relatively large pixel size.

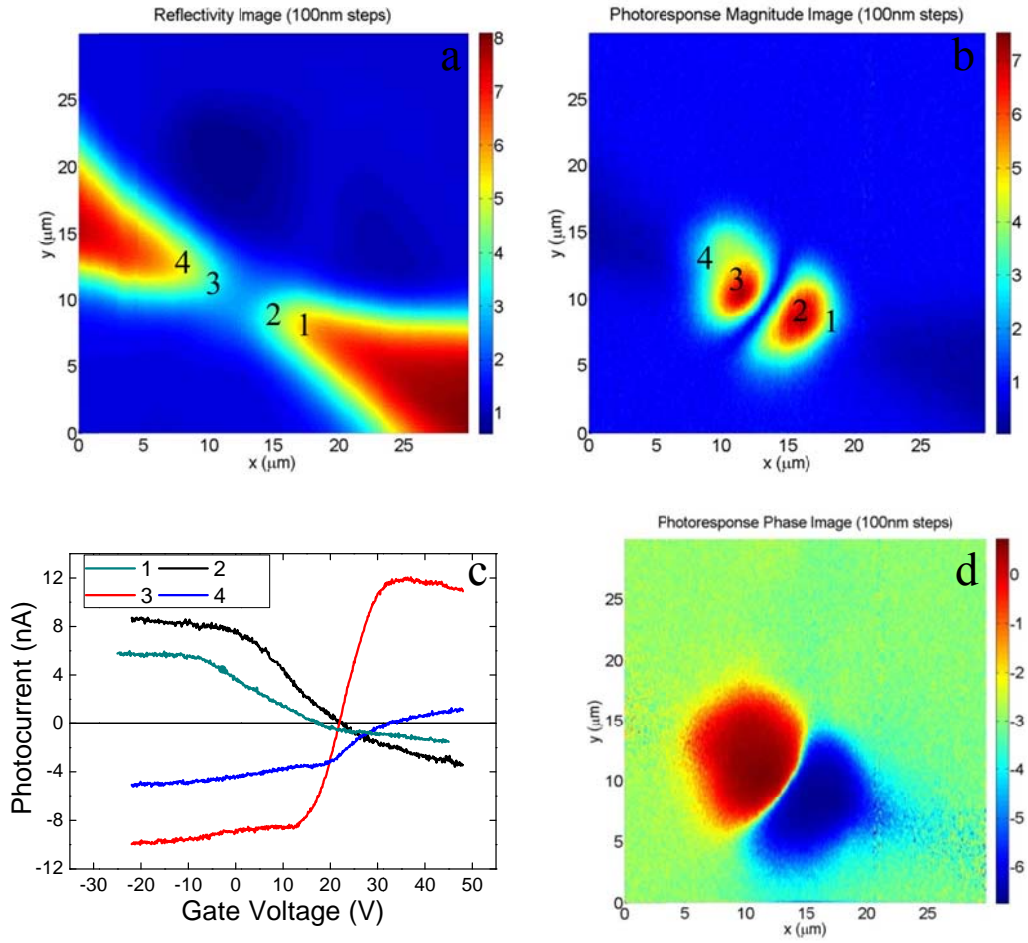


**Figure 4.2** (a) Zoomed-in reflectivity image of the device. (b) Two dimensional magnitude map of the photocurrent signal taken at  $V_g = 0$  V. (c) The photocurrent signal as a function of gate voltage with the beam position fixed at four different points, numbered in (a) and (b). (d) Two dimensional phase map of the photocurrent signal taken at  $V_g = 0$  V corresponding to (b).

Fig 4.2a shows the reflectivity image of the device with a higher resolution. Four points are numbered, corresponding to the bottom metal-metal junction (point at which Au and Cr overlap), the Cr-graphene junction, the graphene-Au junction and the upper metal-metal junction. A two dimensional scan of the photocurrent is then performed. The magnitude and phase map of the signal are recorded in Fig. 4.2b and Fig 4.2d, respectively. Comparing with the reflectivity image, it is found that the photoresponse is largest for illumination of the graphene-metal junctions. The shape and magnitude of the response near one contact are different from those near the other,

presumably due to the asymmetrical metal electrodes (Cr vs. Au). The phase map shown in Fig. 4.2d reveals that the signal changes the polarity when the beam moves from one contact to the other. Fig 4.2c shows the photocurrent as a function of the gate voltage for the beam spot focused on those numbered points in Fig. 4.2a and b. It is much clearer in this plot that the photoresponse is maximized at the graphene-metal junctions. Both the magnitude and the gate dependence of the signal on the Cr-graphene contact are different from that on the Au-graphene contact. This, together with the fact that these curves cross the zero point at different gate voltages, suggests that each part of device could respond to the incident radiation in a different way.

The beam is then defocused to achieve a uniform illumination on the device. The gate dependence of both the photoresponse and the device's conductance are characterized at the same time. As shown in Fig. 4.3a, by measuring the electrical conductivity as a function of the gate voltage, it is known that the charge neutral point of the device is at  $V_g = 20$  V. Fig. 4.3b shows that there is a net photocurrent signal at uniform illumination due to the intrinsic asymmetry of the device. I add up the responses from point 2 (black curve) and point 3 (red curve) as shown in Fig. 4.2c together and plot the sum signal in Fig. 4.3c. Comparing Fig. 4.3b and 4.3c, the similar shapes of the gate-dependent signal imply that if the device is uniformly illuminated, the net response is the addition of the responses contributed by each light sensitive part, as long as the device is working in a linear regime.

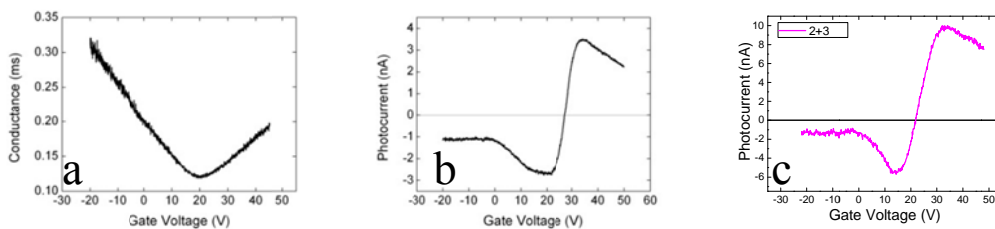


**Figure 4.3** Two-probe electrical conductivity (a) and photocurrent with uniform illumination (b) as a function of the gate voltage. (c) The summation of signals shown in the black and red curve of Fig. 4.2c.



I conclude from this work that the light sensitive part of a bi-metal contacted graphene photodetector is the graphene-metal junction. Dissimilar metal contacts help to generate a net photocurrent signal when the device is uniformly illuminated by a defocused visible light beam. As there is no special requirement of the spot size of the radiation, such devices are compatible with long wavelength (THz) photon detection. The photoresponse is not quantitatively characterized in this experiment, since the signal could be generated from any of several mechanisms for visible excitations (photovoltaic and photothermoelectric effect in graphene, the metal contact's absorption, etc.). A quantitative estimate of the detector's responsivity due to the photothermoelectric effect will be shown in following sections.

#### 4.2 Broadband room-temperature photothermoelectric response

##### 4.2.1 Thermoelectric effect in graphene contacted with dissimilar metals

Next, I will focus on broadband photodetection in graphene based devices via the photothermoelectric effect, especially on room-temperature THz detection. As previously discussed in Chaps. 1-2, graphene has unique advantages for hot-electron photothermoelectric detection, which can be used to detect electromagnetic radiation all the way down to very low frequencies (THz range). Hot electron effects have been exploited in graphene for sensitive bolometry in THz and millimeter-wave at cryogenic temperatures, by using temperature-dependent resistance in gapped bilayer graphene [94], which is sizable only at low temperature, or noise thermometry [110], which requires complex RF electronics. In contrast, the photothermoelectric approach used in this work is temperature insensitive and produces an observable dc signal even under room temperature conditions.

Similar to the previous section, the device consists of an exfoliated graphene flake on low doped Si (100~250  $\Omega\cdot\text{cm}$ ) substrate with 300 nm coated SiO<sub>2</sub> contacted

with dissimilar metals on both sides, realized experimentally through standard electron beam lithography and the shadow evaporation technique (20 nm chromium, followed by 20 nm gold deposition). The optical and atomic-force micrographs of the monolayer graphene device are shown in Fig. 3.5f. Two metal electrodes, each consisting of partially overlapping Cr and Au regions, contact the monolayer graphene flake. The  $3\ \mu\text{m} \times 3\ \mu\text{m}$  graphene channel is selected to be shorter than the estimated electron diffusion length [83].

Fig. 4.4a shows the schematic of the detector in cross section. Figs. 4.4b-e illustrate a simplified photothermoelectric model of the asymmetric device, which shows the principle of the detector's operation, when it is uniformly illuminated by the incident radiation (a detailed discussion will be given in Section 4.4): Electrons in graphene are heated by the incident light and the contacts serve as a heat sink, resulting in a non-uniform electron temperature  $T(x)$  as a function of position  $x$  within the device (Fig. 4.4b). Due to different metal contacts, the Fermi energy profile (Fig. 4.4c) is asymmetric across the device. Consequently, the Seebeck coefficient ( $S$ ; Fig 4.4d) profile becomes asymmetric as well according to Eqn. (2.20). Diffusion of hot electrons creates a potential gradient  $\nabla V(x) = -S\nabla T(x)$  (Fig. 4.4e). The total signal is the integral of  $\nabla V(x)$  over the device length (area under the curve in Fig. 4.4e), and is non-zero because of the asymmetry.

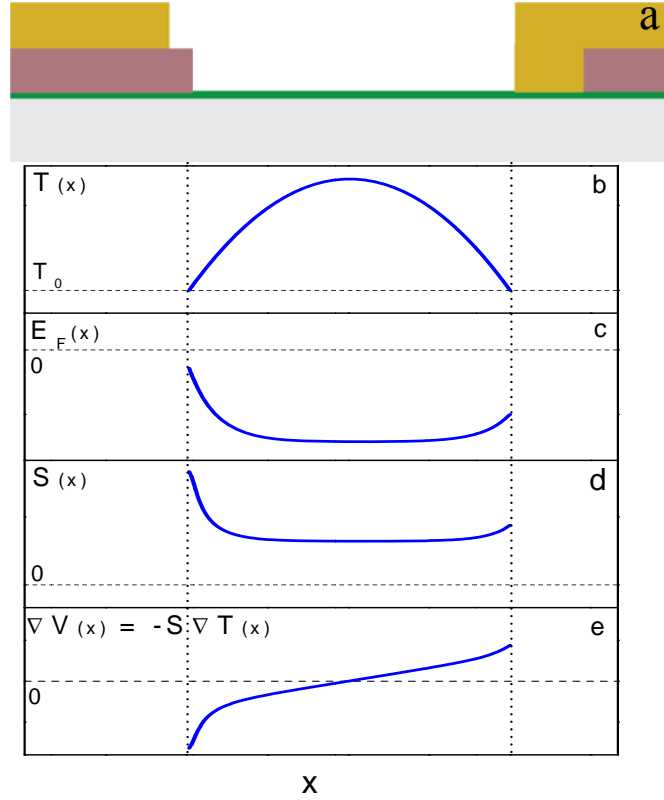


**Figure 4.4** (a) Cross-sectional view of the device. (b-e) Profiles across the device of (b) electron temperature  $T(x)$ , (c) Fermi level  $E_F(x)$ , (d) Seebeck coefficient  $S(x)$  and (e) potential gradient  $\nabla V(x) = -S \nabla T(x)$ . The photoresponse is the integral of  $\nabla V(x)$  over the length of the device, or area under the curve in (e).

The above illustration suggests the photovoltage signal is generated due to temperature-gradient induced hot electron diffusion across the device. It is noticed that photo excitation is not the only way to make charge carriers “hot”, other techniques, for example the Joule heating technique, can also be applied to produce the thermoelectric response. It is useful to compare the magnitude and the gate dependence of these signals, in order to confirm whether they are all generated according to the same operating principle and to understand the photothermoelectric effect more in detail.

There are two methods used in this work to characterize the thermoelectric response of the device to Joule heating, i.e. the dc rectification technique and the ac second harmonics technique. The dc thermoelectric responsivity measurement set-up

is sketched in Fig. 3.7. A dc voltage is applied across the electrodes and the resulting current is  $I_1 = I + I_{\text{thermal}}$  and  $I_2 = -I + I_{\text{thermal}}$  where  $I_1$  and  $I_2$  correspond to different polarities of the applied voltage  $\pm V$ , and  $I$  is the expected Ohmic current generated by the bias voltage neglecting the thermoelectric effect, which changes its polarity according to the dc bias voltage, and  $I_{\text{thermal}}$  is the current due to the thermoelectric effect, whose magnitude depends on the Joule heating power. The polarity of the thermoelectric current depends on the intrinsic property of the device, rather than the polarity of the bias voltage. The applied voltage is 0.2 V and the Joule heating power is tens of microwatts. The thermoelectric responsivity is then expressed as:

$$R = V_{\text{thermal}} / P = I_{\text{thermal}} / I^2 = \frac{2(I_1 + I_2)}{(I_1 - I_2)^2} \quad (4.1)$$

It is verified that  $I_{\text{thermal}}$  is much less than  $I$  in the measurement.

The ac second harmonics technique characterizes the thermoelectric response to ac Joule heating. The set-up is shown in Fig. 3.7 and the operation principle is as follows: An ac bias current  $I_{\text{ac}}(t) = I_0 \sin(\omega t)$  at frequency  $\omega = 15.7$  Hz is applied to the device. Measurements are made in the regime where the thermoelectric voltage is much smaller than  $V_0$ , the amplitude of the applied voltage. The observed thermoelectric voltage  $V(t)$  is proportional to the absorbed power,  $P(t) = (GV_0^2/2)[1 - \cos(2\omega t)]$  where  $G$  is the conductance. This second harmonic component of the voltage  $V_{2\omega} \cos(2\omega t)$  is detected by a lock-in amplifier giving the responsivity:

$$R = 2GV_{2\omega} / (I_0^2) \quad (4.2)$$

Although Eqn. (4.1) and (4.2) measure  $R$  in different ways, the signal is generated from the same physical origin, which is confirmed by characterizing the dc and ac thermoelectric response simultaneously in a similar device mounted in vacuum as shown in Fig. 4.5. The dc and ac thermoelectric responses shown in Fig. 4.5 are very similar to each other.

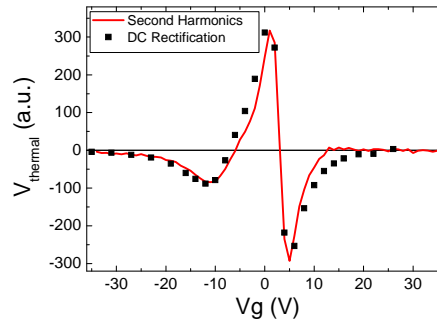


**Figure 4.5** The thermoelectric response measured using dc rectification (black dots) and ac second harmonics (red line) technique on another similar device.

#### 4.2.2 Broadband room-temperature photodetection

Fig. 4.6 summarizes the results of the Joule heating measurements and the broadband photodetection. For the THz excitation, the experimental set-up is described in Fig. 3.8. The device is uniformly illuminated with a chopped continuous wave THz laser, whose wavelength is  $119\ \mu\text{m}$  and the chopping frequency is 331 Hz. The open-circuit photovoltage signal is detected by using a voltage preamplifier (Bandwidth: 10 Hz  $\sim$  10 kHz, Gain: 10k) and lock-in amplifier. The near IR photoresponse is characterized in a similar way, except that the source is replaced with a  $1.54\ \mu\text{m}$  fiber-coupled CW near IR laser as described in Section 3.3. The responsivity  $R$  of the detector, which is defined as the ratio of signal voltage to the absorbed power, is characterized to dc (Fig. 4.6b) or ac (Fig. 4.6e), near infrared ( $1.54\ \mu\text{m}$ ) (Fig. 4.6f), and THz ( $119\ \mu\text{m}$ ) (Fig. 4.6c) excitation. In order to better compare the response across such disparate wavelengths, the responsivity is defined using the absorbed power, rather than the incident power. For broadband photodetection, the device absorbs only a small fraction of the incident near-IR/THz power (it will be shown in the following section how I characterize the spot size and the power intensity of the beam, and how I estimate the quantum efficiency of the detector). While the absorption is low (on order a few percent) it could in principle be increased

by using multilayer graphene, using an antenna, or tailoring a plasmonic resonance in graphene to match the incident frequency (as I demonstrate in Chapter 7). Thus the results referenced to absorbed power highlight the ultimate potential for this device scheme. However, as it will be discussed later, even the unoptimized device shown here with no antenna has performance referenced to *incident* power that is unrivaled in its combination of speed and sensitivity.

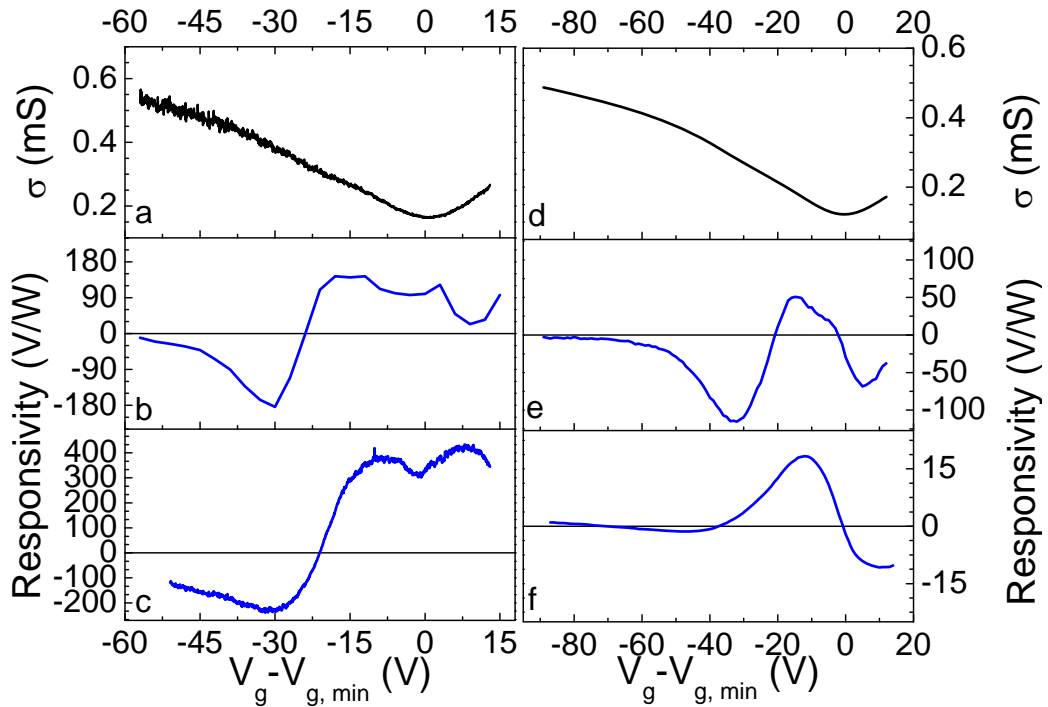


**Figure 4.6** Broadband thermoelectric responsivity of graphene photothermoelectric detector. (a,d) Electrical conductance, (b,e) responsivity to Joule heating, and (c,f) responsivity to radiation as a function of gate voltage for the device shown in Fig. 3.5f at room temperature and in ambient environment. Responsivity to Joule heating was measured at dc in (b) and at 15.7 Hz using the second harmonic technique in (e). Panel (c) shows responsivity to 119  $\mu\text{m}$  wavelength THz radiation and panel (f) shows response to 1.54  $\mu\text{m}$  infrared radiation.

Fig. 4.6a shows the two-probe conductance  $G$  as a function of gate voltage  $V_g$  measured from the point of minimum conductance  $V_{g,\text{min}} = 42$  V. The effective charge carrier mobility is derived to be  $1,500 \text{ cm}^2/\text{Vs}$  from this measurement, likely an underestimate of the true mobility due to inevitable contact resistance in the two-

probe geometry. Fig. 4.6b and 4.6c plot the responsivity  $R(V_g)$  as a function of gate voltage for dc Joule heating and THz excitation, respectively.

Comparing Fig. 4.6b and 4.6c, it is found for both excitations, the peak responsivity appears at low carrier density, changes sign at  $V_g - V_{g,\min} = -20\text{V}$  and is small at large negative  $V_g$ . The overall shape and magnitude are comparable, suggesting that both signals are generated from the same mechanism – the hot carrier thermoelectric effect. The THz responsivity is slightly larger than dc, possibly reflecting a slight overestimation of the THz absorption due to (1) neglected contact resistance in estimating graphene’s conductivity or (2) inhomogeneity, which causes the average conductivity to be greater than the inverse of the average resistivity.

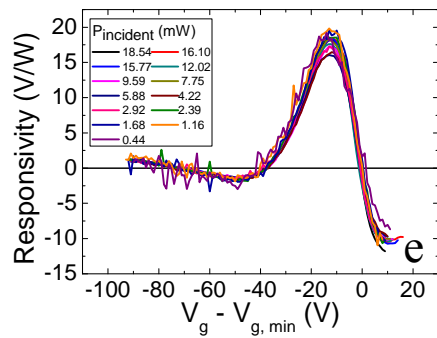
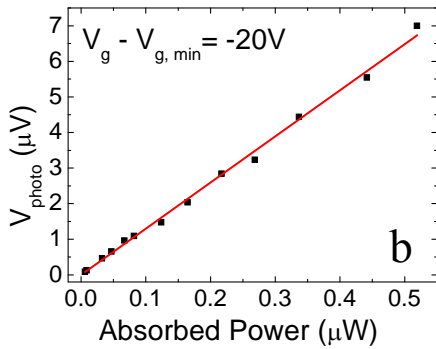
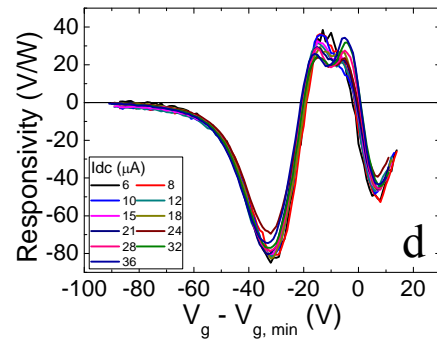
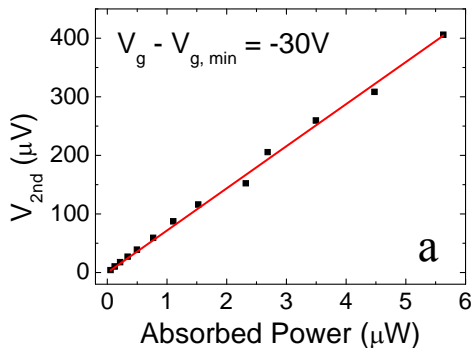
At a later time (after 150 days) I measured the conductance and responsivity to ac Joule heating and near IR illumination of the same device, shown in Figs. 4.6d-f. According to Fig. 4.6d, the charge neutral point drifts to  $V_{g,\min} = 80\text{ V}$  and the conductance becomes somewhat lower, suggesting that the device has degraded slightly.

Now I continue to compare the data shown in the left and right columns shown in Fig. 4.6: The responsivity under ac Joule heating (Fig. 4.6e) is lower than previously measured (Fig. 4.6b) but shows similar functional form, suggesting the degradation of the device has attenuated the thermoelectric response. The near IR responsivity is much lower than the far IR responsivity, possibly indicating the importance of optical phonon emission [45] in hot carrier relaxation for excitation energies exceeding the optical phonon energy ( $\sim 160\text{ meV}$ ). The near IR responsivity shows a different gate-voltage dependence, possibly due to contribution of the photovoltaic effect [76, 111] or due to the thermoelectric response produced by the light absorption in the contact. The photoresponse of the device to near IR radiation will be revisited in following chapters. Fig. 4.6b, c, e, f together show that the thermoelectric signal persists from dc to near infrared frequency with comparable responsivity, implying that the

photothermoelectric effect is a promising mechanism for extraordinarily broadband detection of radiation.

#### 4.2.3 Power dependence of the thermoelectric response

The thermoelectric response in a diffusive device is assumed to be linear, since both the electron thermal conductivity and the Seebeck coefficient of graphene are proportional to the temperature according to the Wiedemann-Franz law and the Mott relation, respectively. It is useful to check the power dependence of the signal and further confirm that the detector works based on the thermal effect and in the linear regime.





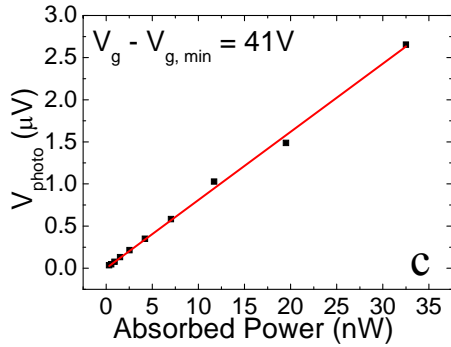


**Figure 4.7** Power dependence of the thermoelectric signal to (a) Joule heating, (b) near infrared excitation, and (c) THz excitation at selected gate voltages. Gate dependent responsivity for different excitation powers are shown in (d) and (e) for Joule heating and near infrared excitation, respectively.

Fig. 4.7a-c shows the power dependence of the response for Joule heating, near-IR and far-IR radiation at a randomly selected gate voltage respectively. The data is taken on one device for Fig. 4.7a-b and on another device for Fig. 4.7c. Both devices are similar to the one shown in Fig. 3.5f fabricated using exfoliated graphene and the shadow evaporation technique for bi-metal contacts. The red solid line in each figure is a proportional fit to the experimental result. Fig. 4.7a-c shows that the voltage response is proportional to the absorbed power (i.e. the responsivity is independent of power) over a power variation of 3 orders of magnitude at fixed gate voltage. For Joule heating and near infrared excitation, a gate scanning of the thermoelectric response at different excitation power input is further performed. The responsivities as a function of the gate voltage for different powers are shown in Fig. 4.7d-e. It is observed that all curves in Fig. 4.7d and 4.7e coincide with one another, suggesting that the responsivity of the device is independent of the absorbed power at all applied gate voltages, verifying that the device is operating in the linear regime at room temperature, and that the assumption that the signal is generated by heating is correct.

### 4.3 Noise-equivalent power of the graphene photodetector

Noise-equivalent power (NEP) is a measure of the sensitivity of a photodetector. It is defined as the signal power that gives a signal-to-noise ratio of one in a one hertz output bandwidth [112]. NEP is a very important characteristic parameter of a detector: It is equal to the noise spectral density divided by the responsivity, thus, a smaller NEP corresponds to a more sensitive detector. Here, the responsivity can be either referred to the absorbed power or the incident power, corresponding to the electrical NEP or optical NEP, respectively. The optical NEP is equal to the electrical NEP divided by the optical coupling efficiency of the detector. Both electrical NEP and optical NEP of the bi-metal contacted graphene detector are characterized in this work.

#### 4.3.1 Incident power and absorbed power

In this section, I will first explain the method used to calculate the incident power. The total incident power of the beam is measured by a silicon bolometer at a temperature of 4 K or a thermopile (calibrated at NIST, Boulder) for THz excitation, and by a power meter (PM100A-Compact Power Meter, Thorlab) for near infrared excitation. However, as shown in Fig. 3.5f, the light sensitive part of the device (few microns) is usually much smaller than the spot size of the beam, therefore, only a small amount of the radiation effectively illuminates the detector.

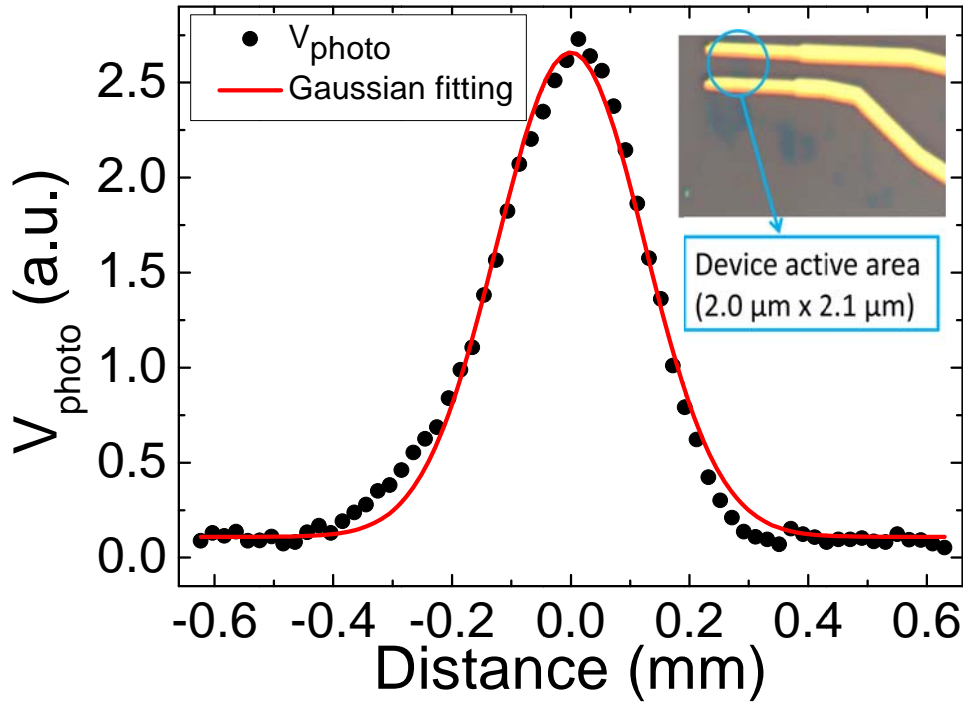


**Figure 4.8** Photovoltage as a function of distance measured as the far infrared laser is scanned across the device (black dots) and Gaussian fit to the experimental data (red curve). Inset: Optical micrograph of the device. The device active area (graphene flake) is between two metal electrodes.

Fig. 4.8 shows how the overfilling of the detector by the beam is accounted for when calculating the incident power: The device shown in the inset of Fig. 4.8, which is similar to the one shown in Fig. 3.5f, is mounted on a motor controlled XYZ-stage, which can freely move in the space with the step accuracy of a few microns. The device can be approximately regarded as a point, since its active area is much smaller than the laser's spot size. When moving the stage in X or Y direction, the beam will be scanned across the device. The spatial distribution of the photovoltage signal reflects the beam intensity profile as shown with black dots in Fig. 4.8. I fit the data using a Gaussian function:

$$V_{\text{photo}} = V_{\text{bg}} + \frac{V_0}{w\sqrt{\pi/2}} e^{-2r^2/w^2} \quad (4.3)$$

where  $V_{bg}$  is the background signal due to electrical pick-up and other noise sources,  $w$  the Gaussian width,  $V_0$  the Gaussian amplitude, and  $r$  is the distance to the center of the device. As shown in the inset of Fig. 4.8, the graphene flake's size is  $\sim 2.0 \mu\text{m} \times 2.1 \mu\text{m}$ . For convenience of calculation, I approximate its shape as a disk with the same area (radius  $r_0 = 1.16 \mu\text{m}$ ). Considering the total incident power  $P_0 = 17 \text{ mW}$  (measured by a thermopile), the effective power  $P_{\text{effective}}$  shining on device's active area can be expressed as:

$$P_{\text{effective}} = P_0 \cdot \frac{\int_0^{r_0} e^{-2r^2/w^2} r dr}{\int_0^{\infty} e^{-2r^2/w^2} r dr} = 0.75 \mu W \quad (4.4)$$

The effective incident power for near infrared excitation can be calculated in the same way as shown above.

Next the quantum efficiency of the device (optical coupling efficiency) will be discussed. As introduced in Section 2.1.1, the absorption of monolayer suspended graphene to visible (or near-IR) radiation is  $\sim 2.3\%$ , according to the interband transition. The device shown here, however, is located on a  $\text{SiO}_2/\text{Si}$  substrate. Since the thickness of  $\text{SiO}_2$  is 300 nm, comparable to the wavelength of the near-IR excitation, multiple reflections in the sandwiched structure need to be considered. The cross sectional view of the device is simplified as shown in Fig. 4.9. Air,  $\text{SiO}_2$  and Si are numbered as medium 0, 1 and 2. The thickness of graphene is neglected and Si is taken to be infinitely thick. The air- $\text{SiO}_2$  and  $\text{SiO}_2$ -Si boundaries are labeled as *I* and *II*, respectively. The electric field of the incident beam is defined as  $E_{i1}$ . Correspondingly, the electric fields of the total incident, reflected and transmitted radiation at two boundaries are named in the same way. The arrows are plotted tilted in the figure to help following the propagating direction of the radiation, however, a normal incidence is assumed in the calculation.

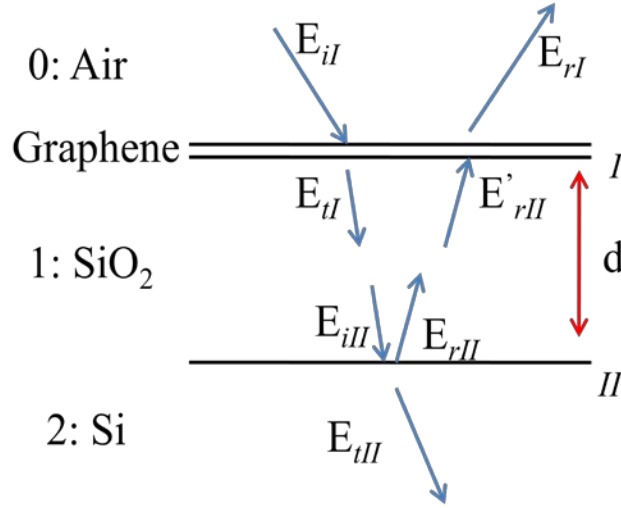


**Figure 4.9** Schematic shown the propagation of a polarized near infrared radiation in a air-Graphene-SiO<sub>2</sub>-Si layered structure.

Define  $\gamma_{0,1,2} = \sqrt{\frac{\xi_0}{\mu_0}} n_{0,1,2}$ , where  $\xi_0$  and  $\mu_0$  are the vacuum permittivity and permeability, and  $n$  is the refractive index of the medium. The total electric and magnetic field at boundary  $I$  can be expressed as [113]:

$$\begin{cases} E_I = E_{iI} + E_{rI} = E_{iI} + E'_{rII} \\ H_I = \gamma_0(E_{iI} - E_{rI}) = \gamma_1(E_{iI} - E'_{rII}) \end{cases} \quad (4.5)$$

Similar relations can be written for boundary  $II$ :

$$\begin{cases} E_{II} = E_{iII} + E_{rII} = E_{tII} \\ H_{II} = \gamma_1(E_{iII} - E_{rII}) = \gamma_2 E_{tII} \end{cases} \quad (4.6)$$

Define  $h = n_1 d$ , where  $d$  is the thickness of SiO<sub>2</sub>, then the phase shift of the beam when transmitting through SiO<sub>2</sub> can be expressed as:

$$\begin{cases} E_{iII} = E_{iI} e^{-ik_0 h} \\ E_{rII} = E'_{rII} e^{ik_0 h} \end{cases} \quad (4.7)$$

Combining Eqn. (4.5) ~ (4.7), one can write:

$$\begin{bmatrix} E_I \\ H_I \end{bmatrix} = \begin{bmatrix} \cos k_0 h & i \sin k_0 h / \gamma_1 \\ \gamma_1 i \sin k_0 h & \cos k_0 h \end{bmatrix} \begin{bmatrix} E_{II} \\ H_{II} \end{bmatrix} \quad (4.8)$$

The matrix in Eqn. (4.8) is called the characteristic matrix, which relates the fields at the two adjacent boundaries. This can be extended to multilayer structures. According to Eqn. (4.5), (4.6) and (4.8), the reflection coefficient, which is defined as  $r = E_{r1}/E_{i1}$  can be derived. The real absorption in the device depends on the total electric field on the interface between the air and SiO<sub>2</sub> and the quantum efficiency  $\eta$  is finally written as

$$\eta = \left| (E_{i1} + E_{r1}) / E_{i1} \right|^2 \cdot 2.3\% = 3.5\% \quad (4.9)$$

by taking the thickness and the refractive index of SiO<sub>2</sub> to be 300 nm and 1.44, respectively.

The absorption for the THz excitation is easier to deal with, since the thickness of the SiO<sub>2</sub> layer is much smaller than the wavelength of the radiation and thus can be ignored. The system is then be approximated as a thin film of graphene sheet sandwiched by two infinite media (air and Si). According to Eqn. (2.3):

$$\eta = \frac{|4n_1 Z_0 \sigma(\omega)|}{|n_1 + n_2 + Z_0 \sigma(\omega)|^2} \quad (4.10)$$

where  $n_{1,2}$  is taken to be 1 and 3.42 for air and Si,  $Z_0 = 377\Omega$  and  $\sigma(\omega)$  is the ac conductivity of the graphene sheet, which can be derived from Eqn. (2.6). For the THz excitation, the imaginary part of  $\sigma(\omega)$  can be neglected and thus replaced by the dc conductivity  $\sigma_0$ , which is characterized through the transport measurement. The dc conductivity  $\sigma_0$  depends on the carrier density, thus the quantum efficiency is gate dependent. Assuming  $\sigma_0$  equals 0.2 ms, the quantum efficiency is  $\sim 1.5\%$ .

#### 4.3.2 Noise source and NEP measurement

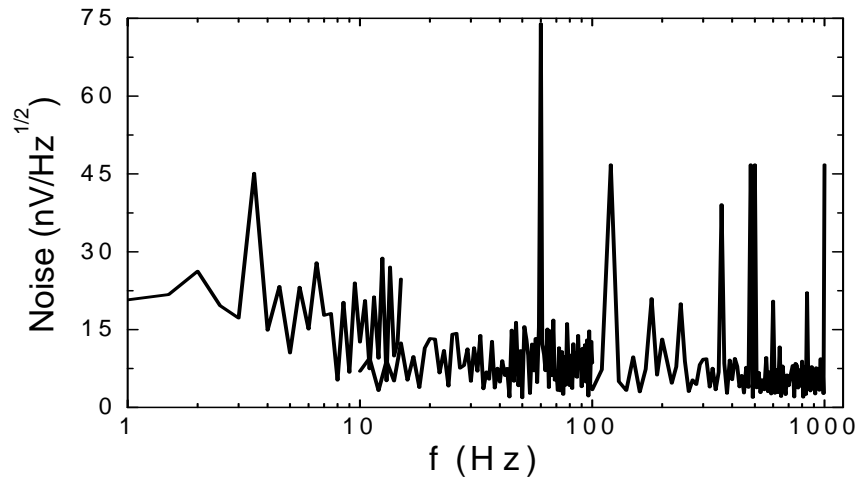
In electronics, noise is a random fluctuation in an electrical signal, a characteristic of all electronic circuits [114]. Before characterizing the noise experimentally, it is necessary to theoretically discuss the origin of the noise in a detector, or more generally, in an electrical circuit. The calculated noise represents

the limit sensitivity of a device. To compare the measured noise with the theoretically calculated value helps to better understand how well the device works and if there is any possibility for the device's quality improvement.

Different types of noise have been demonstrated to exist in electrical systems. The thermal noise, also called Johnson-Nyquist noise [114], is an unavoidable noise, which is the electronic noise generated by the thermal agitation of the charge carriers (usually the electrons) inside an electrical conductor at equilibrium, which happens regardless of any applied voltage. The RMS voltage per unit bandwidth of the Johnson-Nyquist noise is theoretically predicted to be  $(4k_B T/G)^{1/2}$ , where  $k_B$  is the Boltzmann constant and  $G$  is the conductance of the device. This is frequency independent and suggests the Johnson-Nyquist noise exists as long as there is a resistance in the device. Another type of noise, which occurs almost in all electronic devices, is the flicker noise, also referred to as  $1/f$  noise or pink noise, since it is proportional to  $1/f^a$ , where  $0 < a < 2$ . The third type of noise is shot noise, which is caused by unavoidable random statistical fluctuations of the electric current when the charge carriers traverse a gap. In the device presented here, the photoresponse is detected by measuring an open circuit photovoltage, without generating any dc current through the device. Therefore, shot noise can be excluded. Lastly, in detectors relying on thermal effects, it is often necessary to consider phonon noise, which arises from the random exchange of energy between a thermal mass and its surrounding environment. The random exchange of phonon leads to fluctuations in temperature and hence fluctuations in temperature-dependent quantity being detected, i.e. resistance (in a bolometer) or thermopower (in our devices). However, I believe the thermoelectric graphene photodetector introduced here works solely based on hot electron diffusion. As discussed in previous chapters, the electron-phonon coupling in graphene is weak. Thus, I expect that phonon noise does not play a role in determining the noise floor in the present device. In addition, there are some other

noise types, which are either irrelevant or much weaker than the thermal noise, so they will not be discussed in detail.

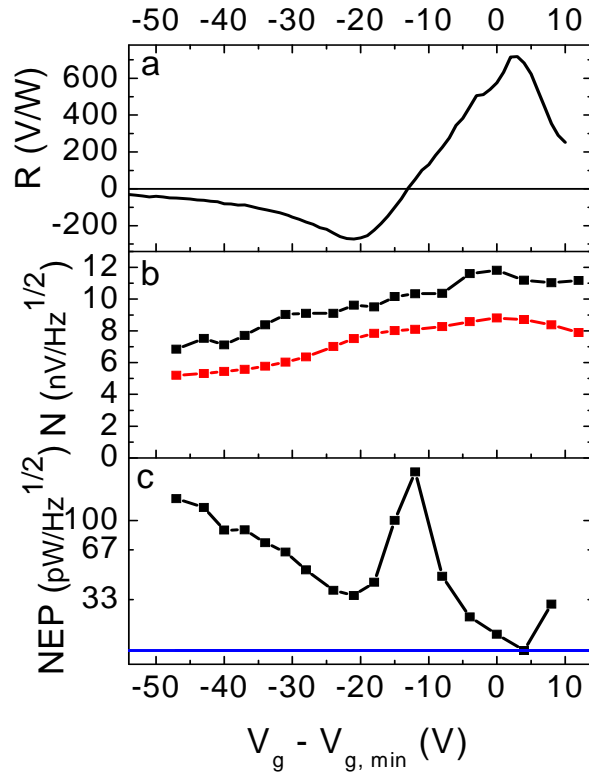
The noise floor of the graphene photodetector is experimentally measured using the same set-up as for the THz photoresponse characterization with the beam blocked, so only the noise will be recorded by the detecting electronics. The device's optical micrograph is shown in the inset of Fig. 4.8. The flicker noise is checked first by measuring the noise as a function of the chopping frequency (locked frequency in the lock-in amplifier) without applying any gate voltages.



**Figure 4.10** Frequency dependent noise floor of a bi-metal contacted graphene photodetector.

As shown in Fig. 4.10, neglecting fluctuations and several peaks at some special frequencies (due to electrical pick-up of the 60 Hz line frequency and other harmonic frequencies), the noise monotonically decreases with the increasing frequency at low frequency. Above 100 Hz however, the noise is nearly frequency independent, suggesting that the flicker noise can be ignored. Therefore, the chopping frequency is selected to be 331 Hz for further characterizations such that the contribution from flicker noise is negligible.





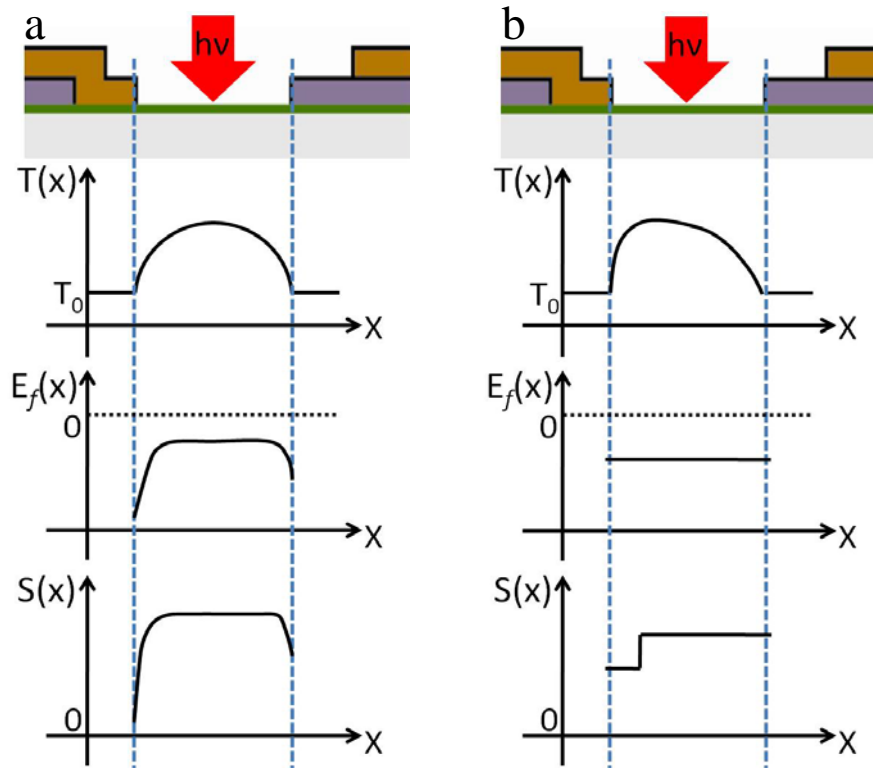
**Figure 4.11** Noise equivalent power of graphene photothermoelectric detector. (a) Responsivity to 119  $\mu\text{m}$  wavelength THz radiation, (b) measured noise (black dotted line) and calculated Johnson-Nyquist noise (red dotted line), and (c) measured noise equivalent power (NEP) as a function of gate voltage for the device shown in the inset of Fig. 4.8. The blue line corresponds to  $\text{NEP} = 16 \text{ pW/Hz}^{1/2}$ . NEP is plotted in log scale.

Fig.4.11 displays the experimentally measured NEP of the device shown in the inset of Fig. 4.8 as a function of the gate voltage. Fig. 4.11a shows the gate-voltage-dependent responsivity; the peak responsivity to THz excitation is 715 V/W, which is the highest sensitivity among all measured devices. Fig. 4.11b shows the measured noise versus the gate voltage with no THz excitation (black dotted line) and the calculated Johnson-Nyquist noise floor  $(4k_B T/G)^{1/2}$  (red dotted line), where  $T = 300 \text{ K}$  is room temperature and  $G$  is the conductance acquired from a two-probe transport measurement. The measured noise and calculated Johnson-Nyquist noise match well with each other and have similar gate dependence, suggesting that the dominant noise in the device is Johnson-Nyquist noise. The experimental noise slightly exceeds the

calculated result, possibly because part of the noise is contributed by the measurement electronics, but the fact that it is very close to the theoretical limit indicates that nearly Johnson-Nyquist noise-limited performance is attainable. Dividing the measured noise by the responsivity at each gate voltage, the experimental NEP is then plotted in Fig. 4.11c. The NEP diverges near  $V_g - V_{g, \min} = 13$  V, where the photoresponse approaches zero. It reaches a minimum level of  $16 \text{ pW}/(\text{Hz})^{1/2}$  at peak responsivity, which is the best measured NEP among all devices.

#### 4.4 Photothermoelectric model for a diffusive device

In this section, a photothermoelectric model will be introduced to qualitatively explain the response of the device shown in Fig. 3.5f to the THz excitation. As illustrated in Chapter 4.2.1, photo excited hot electrons diffuse from the center part of the graphene flake to the metal electrodes, and asymmetric metal contacts give rise to a net photovoltage signal across the device. Next I model the response of the device considering three sources of asymmetry and quantitatively obtain their influence on the thermoelectric signal. I consider two effects in the models: (1) asymmetry due to the contact metals, including pinning of the chemical potential at the graphene/metal interface and the long-ranged electrostatic effect of the nearby metal on graphene due to their different work functions [115], and (2) asymmetry in contact resistance [116]. The first effect is inevitable in the dissimilar-metal contacted devices. Additional scattering in graphene caused by metal near the contact may contribute to additional contact resistance [116] and it is reasonable to suppose that this effect may be asymmetric for different contact metals.



**Figure 4.12** Schematic shown the asymmetrical Seebeck coefficient profile across the device due to (a) chemical potential pinning by the metal contacts and (b) extra contact resistance caused by addition scattering in graphene.

Fig. 4.12a and 4.12b describe the schematics of both effects separately. As shown in Fig. 4.12a, the Fermi level of graphene can be tuned by applying a gate voltage to the device. However, near the contact electrodes, graphene's chemical potential is pinned by the metal, and thus the Fermi energy, as well as the conductance, is different and not tunable near the contacts. According to the Mott relation, the Seebeck coefficient profile across the device then becomes asymmetric due to the chemical potential pinning by dissimilar metals. As a result, a net thermoelectric response is generated, even though the temperature profile is symmetric due to the uniform illumination.

Fig. 4.12b shows the effect of additional resistance in graphene near one electrode. The Wiedemann Franz law suggests that the electron thermal conductance is proportional to its electrical conductance, therefore the additional resistance results

in an asymmetric electron temperature profile across the device. Fig. 4.12b illustrates this effect assuming there is an extra contact resistance on the left side of the device. Although the contact resistance does not change the Fermi energy of the graphene sheet, it does have influence on the Seebeck coefficient  $S$ , as  $S$  is a function of both  $E_F$  and  $\sigma$ . The asymmetric temperature and Seebeck coefficient profiles together, will contribute to a net thermoelectric response.

The detailed modeling of a specific device such as the one shown in Fig. 3.5f is done as follows. The device is approximated as a  $3 \mu\text{m} \times 3 \mu\text{m}$  square. I assume that the local electrical conductivity  $\sigma$  of graphene depends on the local Fermi energy  $E_F$  as:

$$\sigma = \sigma_{\min} \left(1 + \frac{E_F^4}{\Delta^4}\right)^{1/2} \quad (4.11)$$

where  $\sigma_{\min}$  is the minimum conductivity and  $\Delta$  is a parameter that expresses the disorder strength [83]. This functional form for  $\sigma$  correctly extrapolates between the highly doped region where  $\sigma \sim E_F^2$  and the charge neutral point where  $\sigma \sim \text{constant}$ .

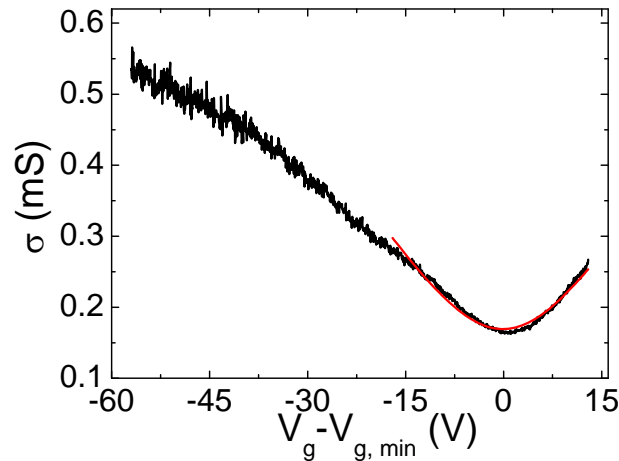


**Figure 4.13** Electrical conductance as a function of gate voltage (black curve) for the device shown in Fig. 3.5f. Red solid line is a fit to Eqn. (4.11).

Fig. 4.13 reproduces the  $G(V_g)$  data from Fig. 4.6a with a fit to Eqn. (4.11) (red curve) to obtain  $\sigma_{\min} = 0.169$  mS and  $\Delta = 107$  meV. To treat asymmetry in contact metal I followed the results of Ref. [115] to obtain the charge carrier distribution across the device and thus the local Fermi level. For chromium and gold I select parameters  $V_{b1} = 65$  meV and  $V_{b2} = 265$  meV for gold,  $V_{b1} = -67$  meV and  $V_{b2} = 65$  meV for chromium according to the model in Ref. [115]. Then the 1D diffusive heat conductance equation, expressed as

$$-\frac{d}{dx}(\kappa \frac{d}{dx} T_{el}) = \rho \quad (4.12)$$

is numerically solved to get the temperature profile across the device [83], where  $\kappa$  is the electron thermal conductivity,  $T_{el}$  is the electron temperature,  $\rho$  is power intensity of the beam, and the  $x$ -axis is parallel to the graphene channel. Given the temperature profile and local Fermi level one can calculate the thermoelectric field  $E = S\nabla T$ , where  $S$  is given by Eqn. (4.11) and the Mott relation  $S = LT(d\ln\sigma/dE_F)$ , and integrate over the device to obtain the thermoelectric voltage.

The thermoelectric signal due to asymmetric contact resistance is treated as follows. It is assumed that the whole device is uniformly doped with Fermi energy determined by the gate voltage, and add an extra contact resistance  $R_c = 33.5 \Omega$  to the region from the gold contact extending 100 nm inside the graphene (the corresponding contact resistivity is  $\rho_c = 1000 \Omega$ ). Then, the conductivity of this region can be rewritten as:

$$\frac{1}{\sigma} = \frac{1}{\sigma_{\min} (1 + \frac{E_F^4}{\Delta^4})^{1/2}} + \rho_c \quad (4.13)$$

The electron thermal conductivity and Seebeck coefficient in this region change correspondingly.

To model the combined effects of contact metal and contact resistance, I first calculate the Fermi level distribution taking into account the contact metal asymmetry. The temperature profile is calculated from the thermal conductivity assuming an extra contact resistance  $R_c = 33.5 \Omega$  in the region from the gold contact extending 100 nm inside the graphene. The local Seebeck coefficient and the thermopower are then calculated as before.

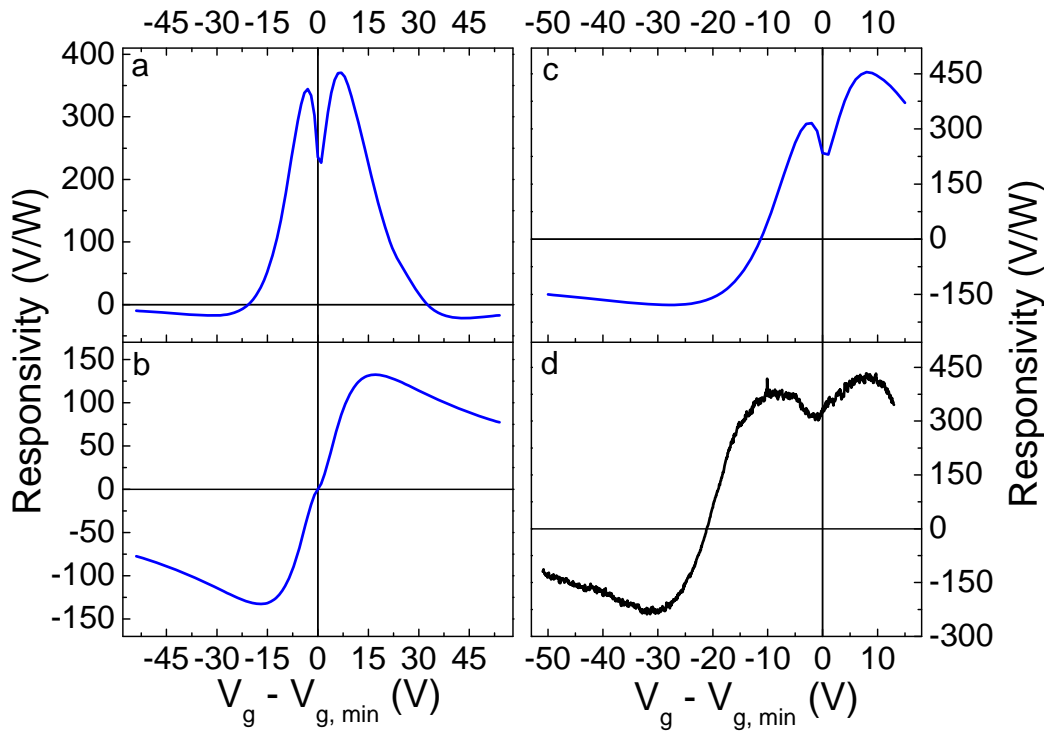


**Figure 4.14** Simulated responsivity of graphene photothermoelectric detector. The assumed asymmetry of the device is (a) induced by the work function difference of Cr and Au and different chemical potential pinning near both contacts, (b) purely induced by an additional contact resistance near the Au electrode, (c) induced by the asymmetries shown in (a) and (b) together. (d) Measured responsivity of the device to 119  $\mu\text{m}$  wavelength THz radiation (replotted from Fig. 4.6c).

Fig. 4.14 summarizes the results of the modeling. In general it is found that asymmetry in contact metal produces a signal symmetric in  $|V_g - V_{g,\text{min}}|$  (Fig. 4.14a) while additional contact resistance produces a signal antisymmetric in  $|V_g - V_{g,\text{min}}|$  (Fig. 4.14b). The combined effect of contact metal and contact resistance asymmetry (Fig. 4.14c) describes well the magnitude and the shape of the gate-voltage dependent

response to THz excitation in the real device (replotted in Fig. 4.14d). One can identify the overall asymmetry as arising from contact resistance, and the dip in responsivity near charge neutrality as due to contact work function/Fermi-energy pinning effects. The model has several adjustable parameters as described before, and verification will require more work to systematically vary these and observe their effect on responsivity. However the fact that the data can be modeled with physically reasonable parameters indicates that model captures the essential operating principles of the device.

#### 4.5 Discussion and conclusion

##### 4.5.1 Improving device performance

It is noticed that only a few percent of the incident power is absorbed by the device since graphene is only one atom thick and allows most of the EM wave transmit through it. The limited absorption of monolayer is e.g. overcome by Liu et al. (UC Berkeley) [117] by integrating graphene with an optical waveguide, which greatly increases the interaction length. Another method to enhance the intrinsic absorption of graphene to THz radiation is to couple the plasmon mode into the device, so that the Drude absorption spectrum is changed to a plasmonic absorption spectrum. By carefully designing the device geometry and adjusting the carrier density of graphene, one can match the plasmonic resonance frequency to the incident EM wave's frequency and thus enhance the absorption. Related experiments and detailed analysis will be shown in Chapter 7. Another problem is that the responsivity of the device shown in this section is several orders of magnitude smaller than the maximum thermopower estimated for an ideal device. Part of the reason is that the temperature profile is symmetric across the device, resulting in a zero integral of the temperature gradient. Since the photovoltage is equal to the integral of  $S\nabla T$ , only a

non-uniform  $S$  will contribute to a net signal, which happens in a narrow region near the contacts. In order to take advantage of the whole device area, one might design a graphene  $pn$  junction device. In this case, the integral of  $S\nabla T$  will be maximized due to anti-symmetric  $S$  profile and the symmetric temperature profile. In addition, the diffusive model did not include the heat transfer from electrons to acoustic phonons, which may lower the electron temperature. The normal electron-acoustic phonon relaxation in graphene is extremely inefficient, since the sound velocity is much less than the Fermi velocity, which, combined with the momentum conservation greatly restricts the energy of emitted phonons [92]. However, recent studies [91-93] show that the hot electron can be relaxed by disorder-assisted phonon cooling (also named as supercooling), which relaxes the momentum conservation restraint and makes the cooling more efficient, resulting in a notable decrease of the electron temperature across the device, especially the center part of the graphene sheet. This effect is possibly insignificant for the bi-metal contacted device, since the center part does not contribute to the net signal a lot. However, the effect needs to be taken into account if the full area of the graphene sheet (e.g. a graphene  $pn$  junction) is involved in generating the signal. In this case, high mobility graphene is preferred to increase the diffusion length and restrain the heat transfer to the lattice due to the supercooling, in order to take advantage of the whole light-sensitive graphene sheet.

#### 4.5.2 Summary and conclusion

To summarize, photodetectors based on dissimilar metal-contacted exfoliated graphene on low doped silicon substrate are fabricated using the standard e-beam lithography technique. The devices' responses to broadband CW-laser excitations are characterized through measuring an open-circuit photovoltage signal.



The laser scanning microscope probes the photoresponse of each part of the device, confirming that the most light-sensitive part is the graphene-metal junction. Transport measurements (dc/ac Joule heating) show that a thermoelectric voltage can be generated in the device due to the hot electron diffusion. Considering the strong electron-electron interaction and weak electron-phonon coupling in graphene, hot electrons can also be generated by photo excitations, thus a photothermoelectric signal is predicted to exist when the device is illuminated by electromagnetic radiation. Broadband photoresponse to uniform CW-laser beams is then measured and compared to response from Joule heating. It is found that the response for THz radiation and Joule heating match very well, however a reduced responsivity and different gate voltage dependence is observed for the short wavelength (near-IR) excitation, indicating the possible importance of optical phonon emission and/or photovoltaic effects.

Furthermore, the THz photoresponse signal is analyzed in detail. Several devices are measured to optimize the responsivity of the detector referred to the absorbed THz power. The best value is identified to be 715 V/W. Noise sources in the detector are discussed. Both experiment and theory show that the dominant noise in the present device is the inevitable Johnson-Nyquist noise, and the Johnson-Nyquist noise limit is nearly attained in the experiment. The lowest NEP of the detector is experimentally measured to be  $16 \text{ pW}/(\text{Hz})^{1/2}$ . In addition, the thermoelectric response can be modeled considering various contact asymmetries. The simulated result matches well with the measured data. The comparison between the detector shown here and the existing technologies will be made in the following chapter after the speed of the graphene photodetector is discussed.

## Chapter 5: Response of graphene photodetectors to pulsed laser excitations

Two important characteristics of a photodetector are its sensitivity and speed. High sensitivity allows the detection of weak signals, while fast speed helps to realize an immediate signal accumulation and analysis. Chapter 4 mainly shows responsivity measurements of the graphene thermoelectric photodetector (addressing sensitivity), whereas this chapter will focus on the response time characterization of these devices. The CW excitation is usually inappropriate for a time-domain measurement, since the radiation continually illuminates the device and generates a steady state response. One way to compensate for this is to modulate the laser beam at a very high frequency, trying to observe a roll-off of the signal in the detector [118]. However, as will be discussed below, graphene detector generally shows very fast response time (10 ps - 1 ns), which means the modulation frequency has to be more than a few tens of GHz. This is challenging both in the generation of the excitation and the readout of the signal. In contrast, ultrafast pulsed lasers are naturally good sources for characterizing the speed of the graphene photodetectors, since pulse widths of 10 fs – 100 fs are readily attainable in the laboratory, and expected to be much shorter than the device's response time, allowing a direct time-domain readout without being affected by the radiation source.

In this chapter, two techniques are used to measure the response time of the device: (1) Direct time domain measurements using a large bandwidth oscilloscope, and (2) Indirect pulse-coincidence measurements taking advantage of the nonlinearity in the device.

### 5.1 Response time in optical and THz range

The most intuitive idea to characterize the detector's response time is to generate a signal using a laser pulse and then record that photoresponse in the time domain, which is experimentally realized in this project using a *Coherent Libra Amplified Ti:Sapphire Laser* and a high speed (40 GHz) sampling oscilloscope as introduced in Chapter 3.4.2.

#### 5.1.1 Time domain characterization for optical excitations

As introduced in Chapter 3.4.2, the photoresponse was excited by a pulsed laser beam with wavelength 800 nm, pulse width  $\sim 50$  fs, repetition rate 1 kHz and pulse energy of 250 nJ. The device's optical micrograph is shown in Fig. 3.10: the starting material was epitaxial single-layer graphene on (0001) semi-insulating (resistivity  $> 10^9 \Omega\text{-cm}$ ) SiC; see [101] for additional details. The semi-insulating SiC substrate eliminated stray capacitance of device to substrate, so that the  $RC$  time constant due to the device's resistance and the capacitance between graphene and the substrate is restrained. Moreover, the bandgap of SiC is well above the photon energy, strongly attenuating the absorption of the incident light by the substrate, which guarantees that the signal is generated by graphene's absorption. The graphene channel on the left is  $4 \mu\text{m}$  long and  $100 \mu\text{m}$  in width. Electrodes are deposited using the shadow evaporation technique to achieve dissimilar metal contacts on both sides (Left side: Cr; Right side: Au). A third electrode is fabricated on the right to make the device electrodes symmetrical (there is no graphene on the right channel), as the time domain measurement is not frequency locked and can thus include broadband noise into the signal. A symmetric device can efficiently avoid picking up noise coupled into the device by electric or magnetic fields. The pads were contacted by a three-tip radio-frequency ground-signal-ground probe for high speed signal transport and readout.

The result is shown in Fig. 5.1. The response time is characterized by FWHM (full width at half maximum), which is defined as the difference between the two extreme values of the time (independent variable) at which the magnitude of the signal (dependent variable) is equal to half of its maximum value, and is equal to 30 ps in this device. As the response is convolved with the 25 ps response of the oscilloscope, it is concluded that the response time is significantly less than 30 ps shown here.

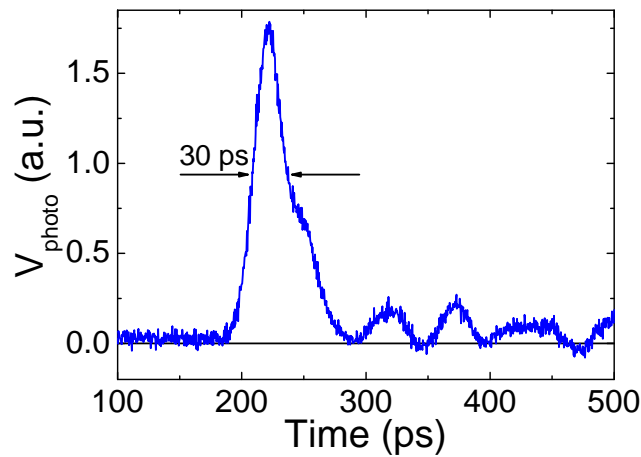


**Figure 5.1** Time domain photoresponse to pulsed laser excitation at 800 nm wavelength recorded by a 40 GHz sampling oscilloscope for device fabricated on SiC (shown in Fig. 3.6b). The FWHM is  $\sim 30$  ps.

### 5.1.2 Time domain characterization for THz excitations

Broadband terahertz pulses with a duration  $\sim 1$  ps and a spectrum spanning 0-2 THz are produced through optical rectification of femtosecond pulses as introduced in the previous section in a lithium niobate prism [107]. The beam diameter is approximately 1 mm and the pulse energy is 160 nJ at a repetition rate of 1 kHz. The device image is shown in Fig. 3.6a. Instead of the SiC, a low doped silicon substrate with  $\text{SiO}_2$  coated on top is selected for device fabrication, which allows one to apply gate voltages to the device when performing the measurement. There is no concern

about the interband transition in silicon since the THz photon energy is much smaller than the bandgap. As it is difficult to focus the THz beam to a tiny spot, a large area detector is prepared using CVD grown graphene. As shown in the right column of Fig. 3.6a, many graphene channels were connected in series, so that the photovoltage generated in each channel will add up together. Each graphene channel is 4  $\mu\text{m}$  long and 500  $\mu\text{m}$  in width and is contacted with shadow evaporated chromium and gold on both sides. The metal electrodes and pads are designed similar to the device shown in the previous section to realize a direct readout at microwave frequencies.

Firstly, a power dependent photoresponse measurement is carried out without applying the gate voltage. As shown in Fig. 5.2a, the power intensity of the incident radiation is controlled by adding intrinsic Si wafers between the laser source and the device. Due to the reflection on the surface, the Si wafer allows  $\sim 50\%$  of the THz beam transmitting through it and thus serves as a natural filter. It is observed that the response monotonically goes down with increased number of the wafers. The peak value of the response as a function of the power intensity is shown in Fig. 5.2b. It is confirmed through a good fit to a linear relationship (red line) that the device did not saturate and is still working in the linear regime.

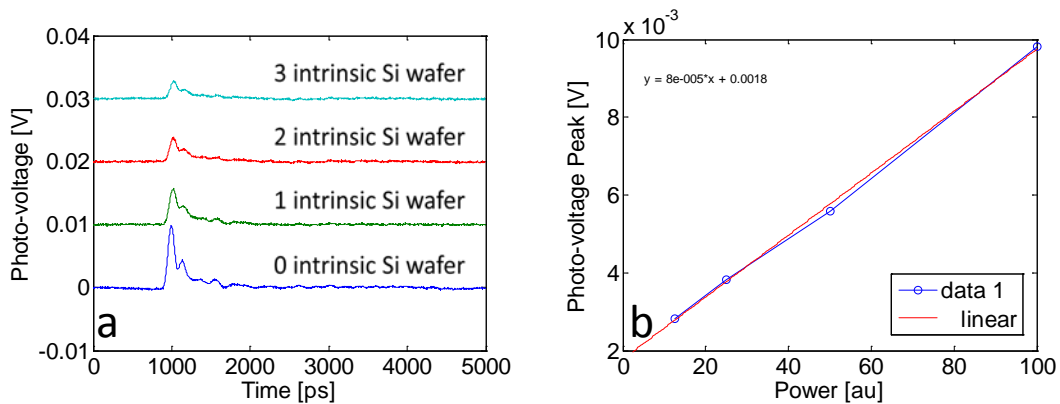


**Figure 5.2** (a) Time domain photoresponse to pulsed THz excitation with different power intensities. 10 mV offset is added to each curve for clarity. (b) Peak response as a function of the absorbed power (blue dots) and a linear fit (red line).

Another piece of information one can get from this power dependence measurement is that there is no visible radiation leaking from the front optics onto the device and generating a signal. As described before, the THz radiation is produced through optical rectification of femtosecond pulses (800 nm) in a lithium niobate prism. Its power is much weaker than the original optical excitation, thus, any leakage of the visible beam may cause a much larger response in the circuit than the THz excitation. The power dependence measurement rules out the possibility of a response contributed by the optical radiation, since the bandgap of intrinsic Si is less than the optical photon energy and thus the Si wafer will block all visible radiations.

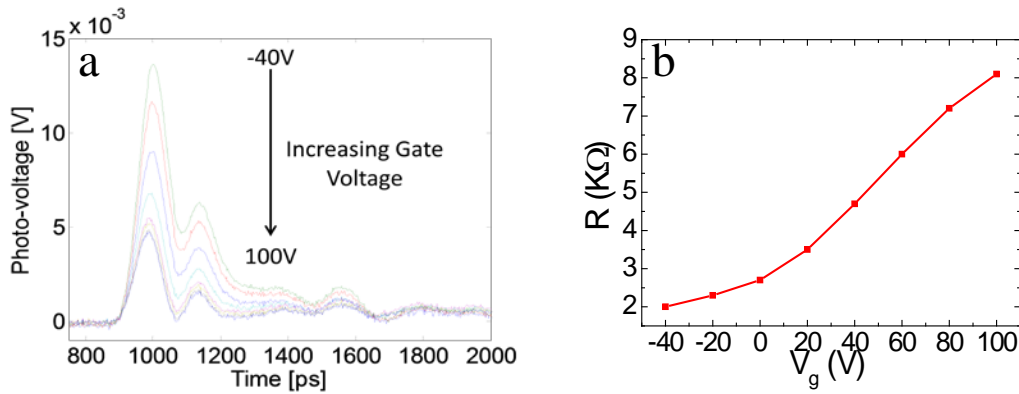


**Figure 5.3** (a) Time domain photoresponse to pulsed THz excitation at different gate voltages. (b) Electrical resistance of the device as a function of the gate voltage.

To better understand the response, it is useful to characterize it at different gate voltages, as shown in Fig. 5.3a. It is found out that the signal monotonically decreases with increasing gate voltages. The electrical resistance of the detector is measured simultaneously as shown in Fig. 5.3b: The device is initially strongly *p*-doped and the charge neutral point cannot be reached even by applying  $V_g = 100$  V. As the experiment and the model discussed in Section 4.4 tell us, the photothermoelectric signal usually peaks near the charge neutral point and is weak for highly doped graphene due to the small Seebeck coefficient, which is inconsistent with that observed in Fig. 5.3a and 5.3b. One possible explanation is that there is a background

signal due to the THz illumination either generated in the substrate or in the metal pads or wires, which contributes a slow response larger than the graphene response, but with a different polarity. Since this background signal is independent of the gate voltage, it behaves like an offset voltage overlapped by the graphene photoresponse.

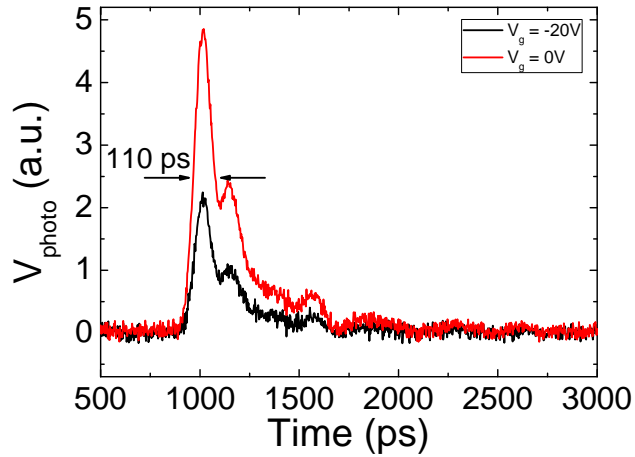


**Figure 5.4** Differential response at  $V_g = -40$  V subtracted from the response at  $V_g = -20$  V (black curve) and  $V_g = 0$  V (Red curve). The FWHM is  $\sim 110$  ps.

To eliminate the background signal, I plot the differential response as shown in Fig. 5.4: The response at  $V_g = -40$  V is subtracted from the response at  $V_g = -20$  V and  $V_g = 0$  V to ensure the rest component of the signal is purely due to the graphene response. According to Fig. 5.4, the FWHM of the electrical impulse response to THz excitation is 110 ps, which is slower than the response time shown in Fig. 5.1 because of the larger size (and thus larger stray capacitance to the substrate) of the CVD device. Note that there is a satellite peak, which is about 120 ps away from the main peak. Considering the distance ( $\sim 1.8$  cm) between the sample and the TPX lens, which is used to focus the THz beam, this satellite peak is probably a signal generated by the reflected beam between the surface and the focusing lens.

## 5.2 Intrinsic response time characterization

The direct time domain measurements shown in the previous section characterized the extrinsic response time of the device, which is useful in a sense of application, because it represents the speed of a real device, including the response time of graphene, the time needed for the signal transmission and accumulation by the detecting electronics. On the other hand, the intrinsic response time, which describes how fast the graphene responds to the incident illumination, is also meaningful to study, since it predicts the limit speed of such photodetectors. In addition, the intrinsic response time is determined by graphene's thermal properties. To characterize it helps to better understand the thermal processes of the system.

The ASOPS method introduced before in Chapter 3.4.1, which is also called the pulse coincidence technique, is applied in this work to measure the intrinsic response time of the photodetector. The experimental set-up and the laser properties are shown in Fig. 3.9a. The optical micrograph of the device is shown in Fig. 5.5a: It consists of a piece of exfoliated graphene connected with bowtie electrodes. Unlike the devices introduced in previous chapters, the shadow evaporation technique is not adopted in the fabrication, so the graphene sheet is contacted with pure chromium pad on one side and with pure gold pad on the other side. This geometry is more appropriate to study the contact absorption effect, which will be discussed in the next chapter.

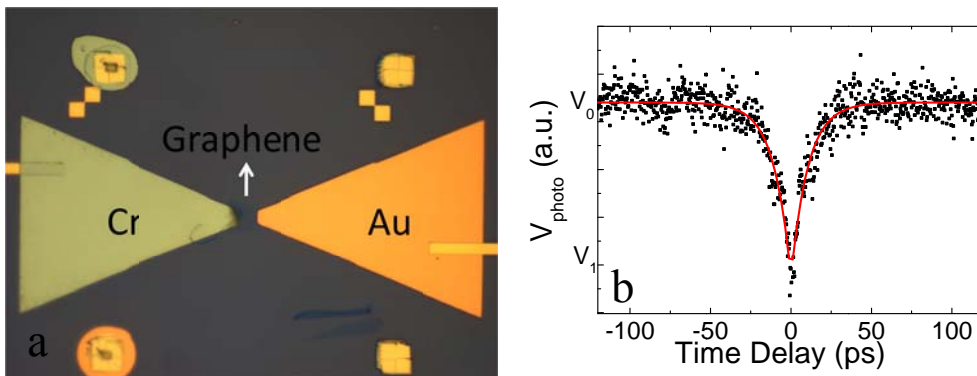




**Figure 5.5** (a) Optical micrograph of the device for the pulse coincidence measurement. (b) Photoresponse from pump-probe laser pulses as a function of delay time at 150K. Red solid line shows a best fit assuming exponential decay of hot-electron temperature.

As introduced before, the pulse coincidence technique requires nonlinearity in the device to induce a change of the signal's magnitude when the delay time of two pulses is less than the device's response time. However, previous experiments show that graphene photodetectors used in this project usually work in the linear regime at room temperature. In addition, the diffusive model also predicts a linear photothermoelectric response. In order to achieve a nonlinear photoresponse, one should consider making the device less diffusive, i.e. increasing the rate of heat transfer contributed by electron-acoustic phonon cooling. Next, I will first discuss the power law of the thermoelectric response to a pulsed excitation due to different cooling mechanisms. The energy relaxation equation is expressed as:

$$\frac{dE}{dt} = C \frac{dT}{dt} = P_{in} - H \quad (5.1)$$

where  $dE/dt$  is the energy change with the time,  $T$  is the electron temperature,  $C = \alpha T$  is the electron specific heat ( $\alpha$  is the prefactor independent of  $T$ ),  $P_{in}$  is the absorbed power, and  $H$  is the heat loss rate. For a ultrafast pulse excitation, the input power can be written as a delta function:  $P_{in} = F_{in} \times \delta(t)$ , giving a rise to the electron temperature, which is described as:

$$T_i = \sqrt{T_0^2 - 2 F_{in} / \alpha} \quad (5.2)$$

where  $T_i$  is the electron temperature right after excited by the pulse, and  $T_0$  is the steady state temperature. Then the system will relax follow the equation:

$$\frac{dT}{dt} = - \frac{H}{C} \quad (5.3)$$

To take electron-acoustic phonon cooling as an example, for the temperature range considered in this measurement, the heat loss rate can be expressed as [92]:

$$H_{e-ph} = A'(T(t) - T_0) \quad (5.4)$$

where  $A'$  is temperature independent thermal conductance. Using Eqn. (5.3), one can solve for the electron temperature as a function of the time. In addition, the thermoelectric as a function of the time can be written as:

$$i(t) = S \cdot (T(t) - T_0) \quad (5.5)$$

where the Seebeck coefficient  $S$  can be expressed as a product of a prefactor and the electron temperature:  $S = \beta T(t)$ . One can calculate the integral of  $i(t)$  to derive the total thermoelectric response due to one pulse and will find that the signal is proportional to  $P_{in}$  when  $T(t) - T_1 \ll T_1$ , whereas it is proportional to  $P_{in}^{3/2}$ , while  $T(t) \gg T_1$ , suggesting that the photoresponse is superlinear due to the electron-acoustic phonon cooling if the energy per pulse is high enough. For completeness, I also summarize the power law for diffusive cooling and the disorder-assisted electron-phonon cooling (supercooling) here. The heat loss rate of diffusive cooling and supercooling can be written as [92]:

$$H_{diff} = A''T(t)(T(t) - T_0) \quad (5.6)$$

$$H_{sc} = A'''(T^3(t) - T_0^3) \quad (5.7)$$

where  $A''$  and  $A'''$  are temperature independent prefactors. Taking Eqn. (5.6) and Eqn. (5.7) into Eqn. (5.3), one can show that the thermoelectric response due to supercooling is proportional to  $P_{in}$ , while  $T(t) - T_1 \ll T_1$ , whereas it is proportional to  $P_{in}^{1/2}$ , while  $T(t) \gg T_1$ , and the response of a purely diffusive device is always proportional to  $P_{in}$ , which is consistent with previous room temperature measurements.

Based on the above discussions, the device is mounted in a cryostat, whose chamber can be cooled down to liquid helium temperature. Nonlinear response is expected in a low temperature measurement, for the following reasons. First, there may be a change in the dominant electron cooling mechanism. The electron-acoustic

phonon coupling thermal conductivity is a constant [90] (shown in Eqn. (5.4)) in the temperature range considered here, while the electron thermal conductivity is inversely proportional to the temperature. Characterizing the device at low temperature may increase the contribution of the electron-phonon heat relaxation, which could be nonlinear if the pulse energy is high enough. Second, the temperature rise upon irradiation becomes a larger fraction of the device temperature. For the same amount of light absorption, the ratio of the electron temperature increase  $\Delta T$  to its steady state temperature  $T_0$  (equals to the lattice's temperature) becomes larger if  $T_0$  is decreased. The discussions in previous paragraph show that the signal generated due to the electron-phonon cooling (as well as supercooling) changes from quasi-linear to nonlinear when  $\Delta T/T_0$  gradually increases. Third, universal conductance fluctuations (UCF) lead to additional temperature dependence at low temperature. UCF is a phenomenon encountered in electrical transport experiments in mesoscopic samples where coherent scattering from disorder leads to reproducible fluctuations in conductance (and related transport parameters, such as the Seebeck coefficient) as a function of an external variable such as gate voltage or magnetic field. As UCF is a coherent phenomenon, it is temperature dependent and becomes prominent at low temperature. UCF can contribute to some nonlinear components of graphene's Seebeck coefficient, especially if  $\Delta T/T_0$  is large, and thus result in a nonlinear photoresponse.

The pulse coincidence measurement was carried out from room temperature all the way down to  $\sim 15$  K. The nonlinear response started to appear below 200 K. The result shown in Fig. 5.5b is measured at  $T_0 = 150$  K. The photovoltage is plotted as a function of the pump-probe delay time. It is observed that the signal shows a dip when the delay time is close to zero. The width of the dip represents the response time of the device. The data is fitted to a two-sided exponential decay (red line in Fig. 5.5b):

$$V = V_0 + (V_1 - V_0)e^{-|\tau_d|/\tau_r} \quad (5.8)$$

where  $V_0$  and  $V_1$  are the flat and dip photovoltage respectively,  $\tau_d$  is the delay time and  $\tau_r$  is the response time as a fitting parameter. The best fits shows an intrinsic response time of 10.5 ps, which is less than the extrinsic response time measured in the direct time domain experiment. However, considering the bandwidth of the oscilloscope used in the time domain characterization, this result is probably consistent with the response time measured in Section 5.1.1.

Next, I will compare the measured response time with theoretical calculations based on a diffusive model. The intrinsic response time is determined by the thermal time constant of the graphene sheet. In a diffusive device, the electron system is relaxed through the heat transfer from hot electrons to the leads. Therefore, the time constant can be written as:

$$\tau = C \cdot A / \kappa \quad (5.9)$$

where  $C$  is the electron specific heat as expressed in Eqn. (1.5), and  $\kappa$  is the electron thermal conductivity as expressed in Eqn. (2.21), respectively;  $A$  is the area of the graphene sheet. The density of states for monolayer graphene is proportional to the Fermi energy:  $D(E) = \frac{dn}{dE} = \frac{2E_F}{\pi\hbar^2v_F^2}$ . Therefore, Eqn. (5.9) can be written as:

$$\begin{aligned} \tau &= \frac{\pi^2 k_B^2 T / 3}{L \sigma T} \cdot \frac{2 E_F}{\pi \hbar^2 v_F^2} \cdot A \\ &= \frac{2 \pi^{3/2} k_B^2}{3 L \hbar v_F e \mu \sqrt{n}} \cdot A \end{aligned} \quad (5.10)$$

where  $\mu$  is the mobility,  $n$  is the carrier density and  $e$  is the elementary charge. The relation  $\sigma = ne\mu$  and  $E_F = \hbar v_F \sqrt{\pi n}$  are used to derive Eqn. (5.10). The mobility of the device is estimated to be 5000 cm<sup>2</sup>/(V·s),  $n$  is  $4.5 \times 10^{12}$  cm<sup>-2</sup> and the area is  $\sim 4$   $\mu\text{m}^2$ . According to these, the time constant is calculated to be 65 ps, which is slower than the experimentally observed value. This suggests that the real thermal conductivity is

possibly larger than the electron thermal conductivity, implying that hot electrons are also scattered either by the graphene lattice [92, 93] or the substrate phonons [119] and this process is accompanied by heat energy transfer.

### 5.3 Conclusion

In this chapter, the photoresponse of the bi-metal contacted graphene detector to broadband pulsed laser excitation was characterized. Direct time domain measurements show that the extrinsic response time of a device optimized for 800-nm optical excitation can be as low as  $\sim 30$  ps, while the response time of a large-area device to pulsed 0-2 THz radiation can be as low as  $\sim 110$  ps. The intrinsic speed of the device is measured by using a pulse coincidence technique, taking advantage of the fact that the generated photovoltage is nonlinear at low temperatures. The intrinsic response time to a near-IR excitation, which corresponds to the thermal relaxation time in graphene, is experimentally determined to be 10.5 ps.

	Responsivity V/W	NEP $\text{pW/Hz}^{1/2}$	Time Constant ns
Our device	$\sim 700$	$\sim 20$	$\sim 0.03$
P3514 Pyroelectric Detector	500	1400	$10^8$
Golay Cell THz Detector	$\sim 10^3$	$\sim 10^4$	$\sim 10^7$

**Table 5.1** Comparison of the characteristics between our device and commercially available room-temperature THz detectors.

At this point, one can compare the graphene photodetector presented in this work to existing technologies. More attention will be paid to the THz range here. The NEP of the bi-metal contacted graphene photodetector,  $16 \text{ pW}/(\text{Hz})^{1/2}$  referenced to absorbed power is competitive with the best room-temperature low-frequency THz detectors, such as the Golay cell and the pyroelectric detector. However a significant advantage of this device is its speed. Table 5.1 shows a comparison between our

graphene photodetector with those commercially available room-temperature THz detectors. The electrical responsivity (and the corresponding NEP) is quoted to demonstrate the sensitivity limit of the device.

Other types of high speed terahertz detectors are studied in different research groups, whose characteristics are shown in Table 5.2. Note that the optical responsivity (and the corresponding NEP) is measured in these detectors.

	Responsivity V/W	NEP nW/Hz <sup>1/2</sup>	Time Constant ns
Our device (2.5 THz)	~ 10	~ 1.1	~ 0.03
FET-based graphene detector (358 GHz) [120]	1.2	2	
FET-based graphene detector (> 1 THz) [121, 122]	$2 \times 10^{-4}$		~ 0.05
Schottky diodes (1 THz) [123]		0.3-10	0.1
Intraminiband superlattice detector (6 THz) [124]	$2.5 \times 10^{-3}$		0.02
Nanosize field-effect transistor (5 THz) [125]		$> 10^4$	0.03

**Table 5.2** Comparison of the characteristics between our device and other high speed THz detectors.

Graphene based room-temperature terahertz detectors based on a transistor geometry [120-122, 126] have shown sensitive detection at 358 GHz [120], however the responsivity and NEP of the device presented here referenced to *incident* power are still superior to these devices. The room for two orders of magnitude sensitivity improvement is anticipated by increasing absorption through e.g. antenna coupling, and further orders-of-magnitude improvements from increasing the thermopower asymmetry as discussed before. For frequencies above 1 THz, the responsivity reported in this work is 5-6 orders of magnitude larger than in earlier graphene-based

detectors [121, 122], in part because photothermoelectric detection does not suffer from the high-frequency roll-off that is characteristic of FET-based detectors. Beyond graphene, there are few existing THz detector technologies with sub-100 ps response times. Schottky diodes can detect 100 ps signal modulations [123], but their responsivity decreases rapidly ( $1/f^2$ ) with frequency  $f$ , and measured NEP are 0.3-10 nW/Hz<sup>1/2</sup> at 1 THz, increasing rapidly above 1 THz. An intraminiband superlattice detector [124] achieved a response time of 20 ps but responsivity was 50  $\mu$ A/W (2.5 mV/W assuming 50  $\Omega$  load) at 6 THz, and a nanosize field-effect transistor [125] demonstrated 30 ps response at 5 THz with an estimated NEP  $>10 \mu$ W/Hz<sup>1/2</sup>. I conclude that the detector shown in this work uniquely offers fast, sensitive detection in the few- THz regime, with orders of magnitude improvement in responsivity and NEP compared to existing THz detectors with sub-100 ps response times.

## Chapter 6: Photoresponse to near-IR pulsed laser: further study and contact effects

As the pulse coincidence technique relies on a nonlinear response to generate a signal, it can be a powerful tool to study the nonlinear power dependent photoresponse of a device. In the previous chapter I introduced the pulse coincidence technique to measure the time response of a graphene photothermoelectric device, presenting measurements carried out without applying gate voltage to the detector. In this chapter I will discuss the gate-voltage dependence of the pulse-coincidence, which will be then further analyzed and explained by characterizing the gate-voltage, power, and temperature dependence of the dc photoresponse.

### 6.1 Gate dependent pump-probe measurement

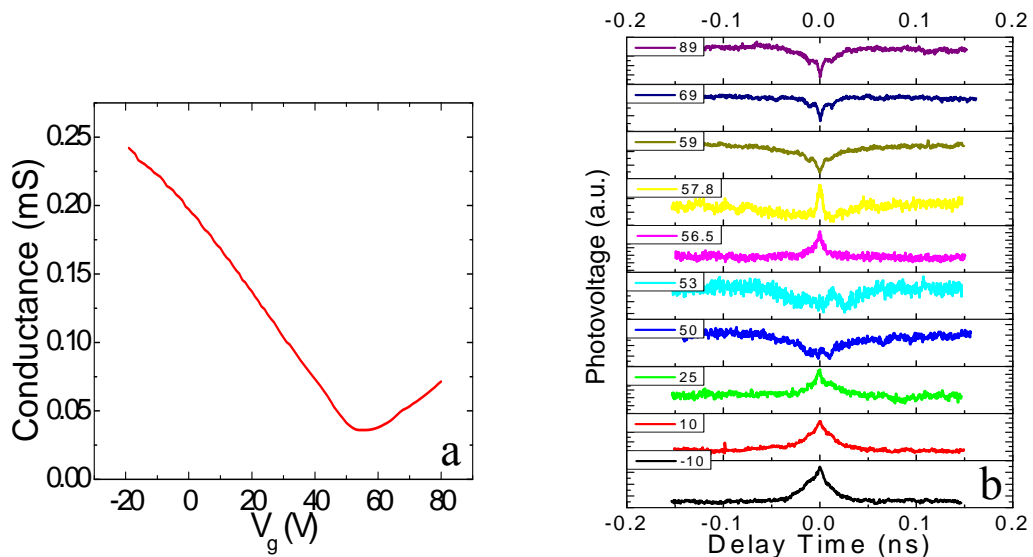


**Figure 6.1** (a) Two-probe conductance as a function of the gate voltage. (b) Photoresponse measured using the pulse-coincidence technique as a function of the delay time at different gate voltages. The temperature is fixed at  $T = 50$  K for both (a) and (b).



The device is the same as shown in Fig. 5.5a. The transport measurement at 50 K is performed with the result shown in Fig. 6.1a. The graphene flake is initially  $p$ -doped and the charge neutral point is at  $V_g \sim 55$  V. The photovoltage at various gate voltages due to the pulsed near-IR excitation as a function of the delay time between the pump and probe pulses is plotted in Fig. 6.1b. Interestingly, the pump-probe signal either shows a peak or a dip at zero delay time, depending on the applied gate voltages. Note that the phase of the signal is not taken into account in Fig. 6.1b (the absolute value of the photovoltage is shown). One can include the polarity of the signal and replot all the curves shown in Fig. 6.1b in one graph as shown in Fig. 6.2.

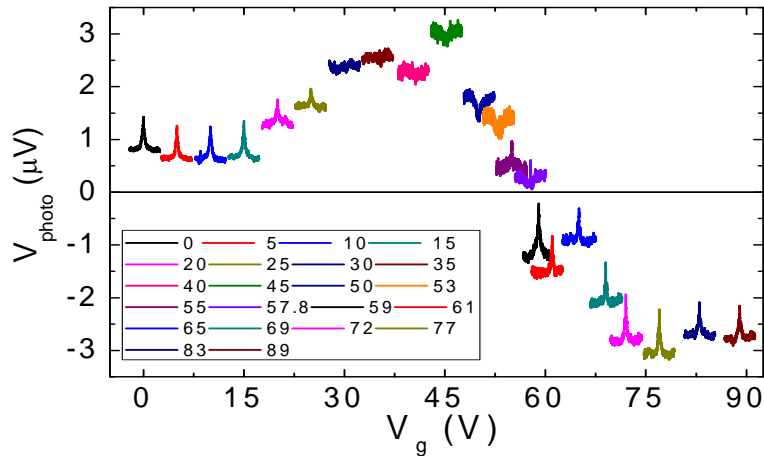


**Figure 6.2** Photovoltage excited by two near-IR pulsed excitations as a function of the gate voltages. At each gate voltage the photovoltage as a function of time delay is shown for a time-delay window of  $\pm 150$  ps.

It is easy to compare in Fig. 6.2 the pulse-coincident response (signal at  $\tau_d = 0$ ) with the floor response (signal at  $\tau_d \gg 0$ ) of the signal at different gate voltages. One finds that below  $V_g \sim 30$  V, the signal gets enhanced when  $\tau_d = 0$ , whereas above  $V_g \sim 60$  V, the signal decreases when two pulses overlap each other. One possible explanation to this is that the signal is superlinear below  $V_g \sim 30$  V and sublinear above  $V_g \sim 60$  V, resulting in an enhancement or an attenuation of the response at zero delay time, respectively. Another argument which can account for the observed

phenomenon is that the photoresponse consists of two components, one linear and the other nonlinear. The nonlinear signal contributes to the feature at  $\tau_d = 0$ , while the linear part serves as an offset to the floor response, which may change the polarity of the floor response and thus makes the nonlinear enhancement/attenuation appears like an attenuation/enhancement in Fig. 6.2.

### 6.2 Power dependent dc photoresponse to pulsed laser excitation

To distinguish between these possibilities, the power dependence of the dc photoresponse to one pulsed laser excitation was characterized at different temperatures. Fig. 6.3a shows the data taken at high temperature ( $T = 267 \pm 2$  K, where the error corresponds to fluctuations in temperature during the measurement of different data sets) and Fig. 6.3b plots the scaled photoresponse (which can be regarded as the responsivity with arbitrary unit) normalized by the incident power as a function of the gate voltage. The fact that all curves coincide with one another in Fig. 6.3b suggests that the signal is proportional to the absorbed power (linear response), consistent with the pulse coincidence measurement shown in the previous section that the pump-probe peak/dip feature is not observed at  $T > 200$  K.

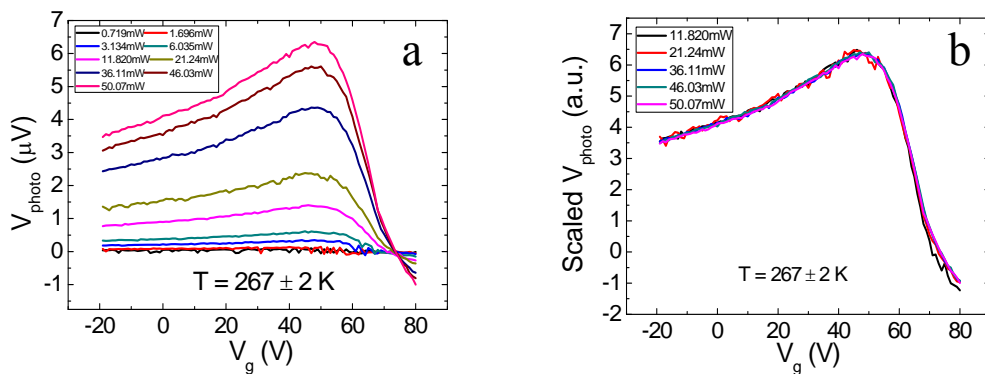


**Figure 6.3** (a) Photovoltage as a function of the gate voltage to one pulsed near-IR excitation with different incident powers. (b) Photoresponse shown in (a) normalized by the incident power as a function of the gate voltage.

Fig. 6.4a shows the power dependent photoresponse measured at low temperature ( $T = 120 \pm 2$  K). Compared to Fig. 6.3a, both the magnitude and the gate-voltage dependence of the signal have changed. More interestingly, it is found that the intersection point with the x-axis changes from  $V_g \sim 60$  V to  $V_g \sim 70$  V, when the incident light power gradually increases. This is shown in Fig. 6.4b, the zoomed-in plot of Fig. 6.4a. At certain gate voltages the signal must be non-monotonic in power, in fact crossing zero at finite power. This evidence strongly suggests that the signal is composed of at least two components with different power dependences. The measured signal, which is the summation of these two components, thus crosses the x-axis at different gate voltages when changing the incident power since both components have their own functional form of the gate voltage dependence.

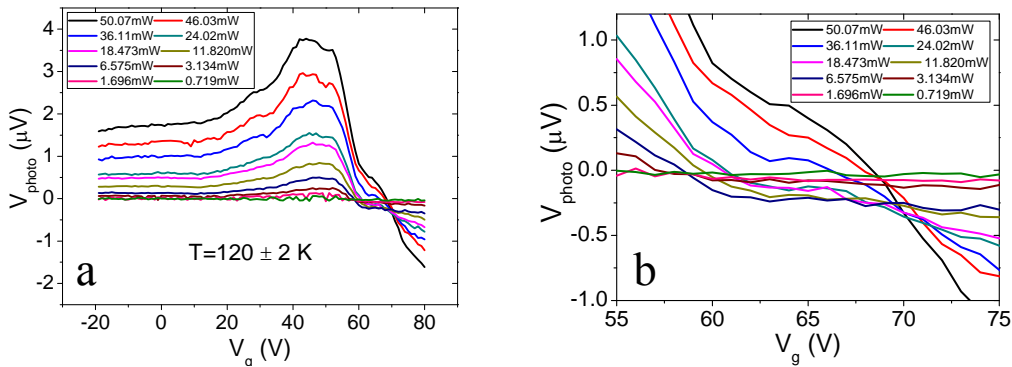


**Figure 6.4** (a) Photovoltage as a function of the gate voltage due to one pulsed near-IR excitation with different average incident powers as shown in legend. (b) Zoomed-in plot of (a) showing the response from  $V_g = 55$  V to  $V_g = 75$  V.

### 6.3 Temperature dependent dc photoresponse to pulsed laser excitation

To determine the origin of these two components of the signal, the temperature-dependence characterization of the photoresponse to one near-IR pulse laser excitation is carried out and the results are shown in Fig. 6.5.

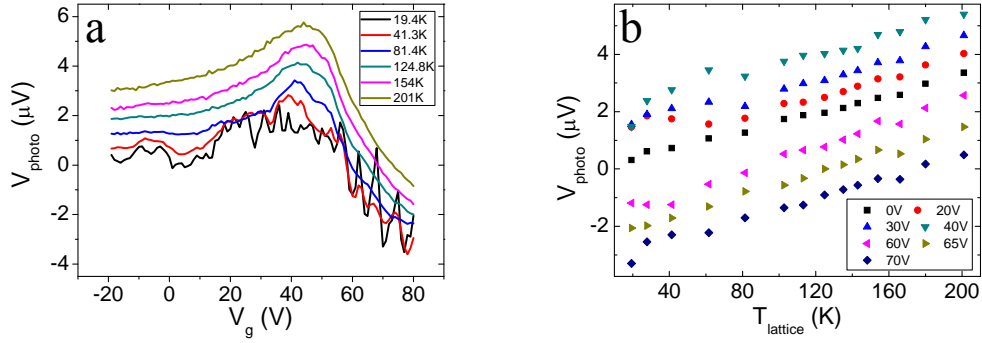


**Figure 6.5** (a) Photovoltage as a function of the gate voltage to one pulsed near-IR excitation at different temperatures. (b) Photovoltage as a function of the temperature to one pulsed near-IR excitation at different gate voltages.

As shown in Fig. 6.5a, the temperature varied from  $T = 19.4$  K to  $T = 201$  K. The overall shape of the photovoltage changes only slightly with the temperature, suggesting that one component of the signal is almost independent of the temperature, but depends on the gate voltage. It is also noticed that the photovoltage continually shifts downwards along the y-axis with cooling. The shift is observed almost uniformly at any gate voltage, implying that the other component of the signal is nearly independent of the gate voltage, but is a function of temperature. To better understand its relation to the temperature, the data shown in Fig. 6.5a is replotted as a function of the lattice temperature in Fig. 6.5b. It is easily seen that the signal shows a linear dependence on the lattice temperature above 80 K. At low temperatures, the strong fluctuation, which can also be observed in Fig. 6.5a, makes it difficult to tell the exact functional form of the signal vs. lattice temperature.

Since the temperature dependent part of the photovoltage barely changes when the carrier density of graphene is tuned in a quite wide range, I considered that this part of the signal is not generated by light absorption in the graphene flake. Ref [127] provides the optical properties of metallic thin films, which shows that the reflectances  $R$  of chromium and gold at the wavelength  $\lambda = 1.55$   $\mu\text{m}$  are very different, namely 0.66 and 0.98, respectively. Considering the beam can hardly transmit

through the metal with the thickness used in this device ( $\sim 40$  nm), the absorption in chromium pad can be as high as  $\sim 34$  %, which is much larger than graphene's absorption (a few percent due to the interband transition). Therefore, it is possible that a thermoelectric response due to the absorption in chromium contributes to the total photovoltage signal of the device.

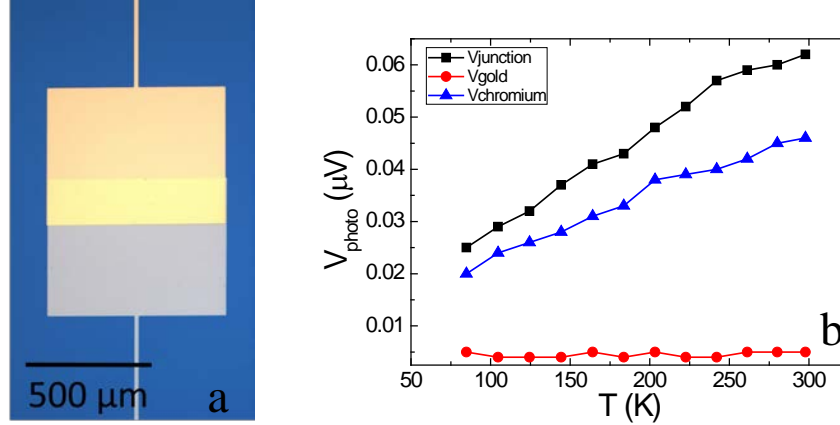


**Figure 6.6** (a) Optical micrograph of a Cr (bottom) - Au (top) thermocouple device. (b) Photoresponse to a CW near-IR excitation as a function of the temperature. Data is shown for the beam focused on the gold pad (red line), the chromium pad (blue line), and the junction (black line).

In order to test whether this effect could produce a signal comparable to the measured one, I devised a test device consisting of a chromium-gold thermocouple constructed from similar thin films as used in the graphene device. The photothermoelectric response of the metal electrodes is characterized by focusing a CW near-IR ( $1.55 \mu\text{m}$ ) laser beam on the chromium-gold thermocouple device, as shown in Fig. 6.6a. The focused spot size is a few microns, so that local illumination is possible. The device is mounted in a cryostat and the photoresponse is measured at different temperatures as shown in Fig. 6.6b. The red curve, which corresponds to the noise level, suggests that there is no photoresponse when the beam is focused on gold due to nearly 100 % reflection of the surface. In contrast, a photoresponse, which shows a linear dependence of the temperature, is observed when the chromium

surface is illuminated (blue curve). This signal is further enhanced when the focused beam spot is adjusted closer to the Cr-Au junction. It is complicated to directly scale the photoresponse shown here to the temperature dependent component of the signal observed in the graphene photodetector shown in Fig. 5.5a, since both the laser source and the sample's geometry have changed significantly. However, one can still make a qualitative estimation: The absorbed power of the chromium pad shown in Fig. 6.6a is comparable with the contact absorption in the experiment shown in Fig. 6.5a. However, the thermoelectric voltage is strongly reduced in Fig. 6.6a, because the wide Cr-Au junction ( $\sim 700 \mu\text{m}$  in width) electrically shorts the light illuminated area (the spot size is  $3 \sim 4 \mu\text{m}$ ), which behaves like a small battery, making the measured voltage  $\sim 200$  ( $700 \mu\text{m} / 3.5 \mu\text{m}$ ) times smaller. This is not an issue for the data taken in Fig. 6.5a, because the spot size of the beam is large and covers the whole area of the bowtie electrodes. It is thus reasonable that the photovoltage shown in Fig. 6.5a is two orders of magnitude larger than that shown in Fig. 6.6a. A quantitative comparison requires to consider more factors, such as the various heat pathways for both geometries, the difference between pulsed and CW excitations etc., but the fact that chromium can absorb near-IR excitation and generate a thermoelectric response that is linear with the temperature suggests that it is very possible the temperature dependent component of the signal observed in the graphene detector is generated due to the chromium contact's absorption.

#### 6.4 Decoupling of the linear and nonlinear signals

Lastly, I will try to decouple the signal shown in Fig. 6.4a into a linear component and a nonlinear component. According to the analysis in previous paragraphs, the photovoltage can be expressed as:

$$V = V_1 \cdot P + V_2 \cdot P^\alpha \cdot f(V_g) \quad (5.4)$$

where the first term is due to the contact absorption, which should be linear and gate independent, and the second term, originated from graphene absorption, shows a power law and is gate dependent. Consider the data shown in Fig. 6.2, the pulse coincidence measurement shows a flat response at  $V_g = 35$  V, implying a pure linear response. Therefore, one can subtract the signal at  $V_g = 35$  V from each curve shown in Fig. 6.4a to get the nonlinear component of the response, while the subtracted gate-independent value is the linear component.

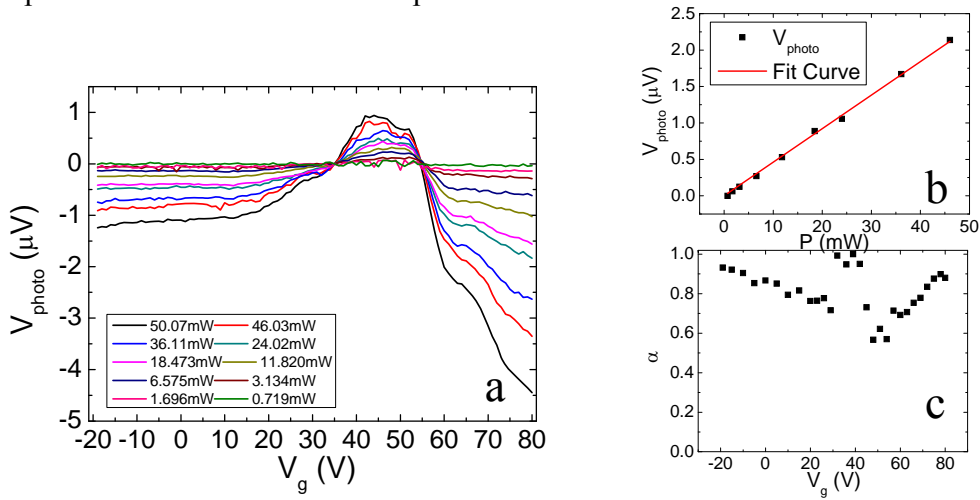


**Figure 6.7** (a) Nonlinear component of the photovoltage as a function of the gate voltage to a pulsed near-IR excitation with different incident powers.  $T = 120 \pm 2$  K. (b) Linear component of the photovoltage as a function to the incident laser power (black dots) with a linear fits (red line). (c) Extrapolated  $\alpha$  at different gate voltages.

The subtracted signal is plotted as a function of the laser power in Fig. 6.7b. The fact that the data can be well described using a linear fits is consistent with the expression of the first term in Eqn. (5.4). The remaining part of the signal, which is assumed to be generated due to graphene's absorption as shown in Fig. 6.7a, is further analyzed by taking the photovoltage at each gate voltage as a function of the light power, in order to extrapolate the power law in the second term of Eqn. (5.4) at different gate voltages separately. The result is shown in Fig. 6.7c:  $\alpha$  varies within a range from 0.6 to 1. According to the theory shown in Chapter 5,  $\alpha$  equals to 1 in a diffusive device, while in a device cooled by electron-acoustic phonon scattering /

supercollision [92],  $\alpha$  varies from 1 to 1.5 / from 0.5 to 1, respectively, depending on the energy per laser pulse. Therefore, the extrapolated  $\alpha$  shown in Fig. 6.7c is consistent with supercollision as reported before in graphene. The fact that  $\alpha$  is not a constant at different gate voltages may suggest that the simple method used here to decouple the signal into a non-linear component intrinsic to graphene and a linear component due to the leads may miss additional contributions. For example, the heated chromium pad can generate a temperature gradient in graphene from Cr side to Au side, which contributes to a response which is linear in power (since  $\Delta T$  is linear in power due to chromium's absorption) but gate-dependent (due to the gate-dependent thermoelectric effect in graphene).

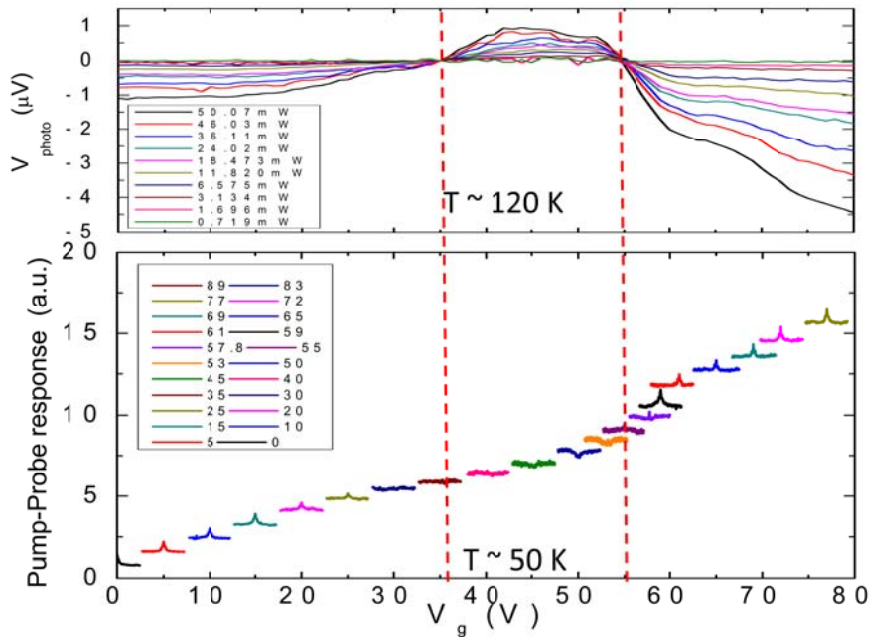


**Figure 6.8** Comparison between the nonlinear response extrapolated from the power dependence measurement at  $T \sim 120$  K (top) and the pump-probe response characterized at  $T \sim 50$  K (bottom).

In Fig. 6.8 I replot Fig. 6.7a (top) and Fig. 6.2 (bottom), to compare the nonlinear signal extrapolated from the power dependence measurement and from the pulse coincidence measurement. In comparison, the nonlinear photoresponse shown on top



is positive between  $V_g \sim 35$  V and  $V_g \sim 55$  V, where the pump-probe signal displays a dip feature at zero delay time, suggesting that the signal is sublinear. Below  $V_g \sim 35$  V and above  $V_g \sim 55$  V, the nonlinear photoresponse flips the sign, reproduced in the pump-probe response as a change from a dip to a peak, which again indicates the sublinear nature of the signal, since the absolute value of the photovoltage is decreased when two pulses overlap each other. Hence the pulse-coincidence data is also consistent with the presence of two signals, one linear in power and temperature and independent of gate voltage, and the other sublinear in power, with a magnitude and sign depending on gate voltage.

### 6.5 Conclusion

To summarize, two components of the signal were observed in a graphene photodetector contacted with large area chromium on one side and gold on the other side, when it is uniformly illuminated by a near-IR pulsed laser. Power dependence and the pulse coincidence measurements show that one component is linear in power and the other is nonlinear at low temperatures. Further characterizations at different temperatures suggest that the nonlinear part of the signal originates from the absorption in the graphene flake, where the linear part is possibly due to the larger heating of the chromium electrode compared to the gold electrode. Further analysis was done to decouple these two components. The dependence of the magnitude and sign of the nonlinear part of the signal on gate voltage explains well observations from the pulse coincidence measurement. In the future, a more quantitative modeling of the signal can be done by taking into account the heat pathways in chromium pad and in graphene, in order to construct the temperature profile across the Cr-graphene-Au junction.

## Chapter 7: Plasmon-enhanced THz detection in graphene

The theories and experiments introduced in the previous chapters have demonstrated that hot electron effects are important in graphene even at room temperature, and have been exploited to realize fast, sensitive THz detection via the photothermoelectric effect. Compared with commercially available room-temperature THz detectors, the graphene based photodetector presented in this work is eight to nine orders of magnitude faster. However, the sensitivity is not improved so much, partly because the optical coupling efficiency in graphene is low, which means a significant challenge remains in increasing graphene's absorption. As discussed in Chapter 2.1, owing to its zero band gap nature, doped graphene shows a relatively high dc conductivity, resulting in a considerable Drude absorption in the THz range. However, the Drude absorption in graphene is strongly frequency dependent, decreasing as  $(\omega\tau)^{-2}$  at high frequencies  $\omega \gg 1/\tau$  where  $\tau$  is the scattering time, proportional to graphene's mobility and typically 10 ~ 100 fs in graphene. Thus, the Drude absorption rolls off at lower frequencies in higher mobility (higher  $\tau$ ) graphene samples.

A number of efforts have been made to increase the absorption in graphene photodetectors. Quantum dots deposited on graphene can enhance the light-matter interaction [19], however the approach is likely limited to the visible or near infrared where the interband absorption of the quantum dot lies, and the response times are slow. Locating the detector in a microcavity, which resonates at selected frequency, can enhance absorption, but to date this has been demonstrated only at near-infrared wavelengths [128] and would be cumbersome for long wavelength THz radiation. Coupling the detector to an antenna is a viable approach for frequencies up to the low THz but there are few demonstrations of antenna-coupled graphene devices [126],

and the approach is applicable only to devices whose size is much smaller than the wavelength. In contrast to these approaches, plasmon resonances in finite-width graphene, as discussed in Chapter 2.2, can provide a strong absorption which has a fast response (set by the thermal relaxation time [129]), is tunable over a broad range of frequencies in the THz through changing either the confinement size or the carrier density [70, 71], and is more amenable to fabrication of arrays for large-area detectors, compared to antenna-coupled devices.

In this chapter, I will first discuss the plasmon mode in a graphene microribbon array, both theoretically and experimentally. Then transmission spectra of different graphene-metal microstructures, obtained using the FTIR technique, will be presented. The challenges of maintaining a distinct plasmon resonance in metal-contacted graphene while maintaining large coupling to the incident light will be discussed. A design using a graphene microribbon array oriented at 45 degrees to a metal contact array is adopted to address the challenges. This optimized device is then used for a far-IR photodetection experiment, in which the plasmon-enhanced photovoltage is observed in a polarization-dependent measurement, by tuning the carrier density in the device to adjust the plasmon resonance frequency to match with the incident radiation's frequency.

### 7.1 Plasmon mode in a graphene microribbon array

The plasmon is described in the classical picture as an oscillation of free electron density with respect to the fixed positive charges in the material, as described in Chapter 2.2. The plasmon dispersion relation of a graphene disk is derived in Eqn. (2.16). Many such disks arranged regularly in a two dimensional surface will form a large-area plasmonic resonant structure. This isotropic pattern, however, is not suitable for making an electronic photodetector, since the elements are not electrically

connected. In this chapter, I consider graphene patterned into a microribbon array, i.e. a pattern of alternating graphene and bare substrate in one direction (perpendicular to the ribbons) with ribbons extending continuously in the other direction (parallel to the ribbons). Such an array supports the plasmon resonance in the direction perpendicular to the ribbon. The question addressed in this chapter involves how best to contact this array with metal structures to form a large area photodetector while preserving the plasmon resonance and allowing coupling of the incident light to the plasmon mode.

Considering a two dimensional graphene sheet sandwiched between two media, the dispersion relation of the plasmon shown in Eqn. (2.17) can be rewritten as:

$$q = \frac{\hbar(\varepsilon_1 + \varepsilon_2)}{4\pi^{1/2}e^2v_F n^{1/2}} \omega(\omega + i/\tau) \quad (7.1)$$

where  $\varepsilon_{1,2}$  is the dielectric constant of the media above/below graphene,  $n$  is the charge carrier density in graphene,  $v_F = 10^6$  m/s is graphene's Fermi velocity,  $\hbar$  is Planck's constant, and  $e$  the elementary charge. It is expected that a graphene ribbon of width  $W$  will determine the plasmon wavevector  $q$  such that

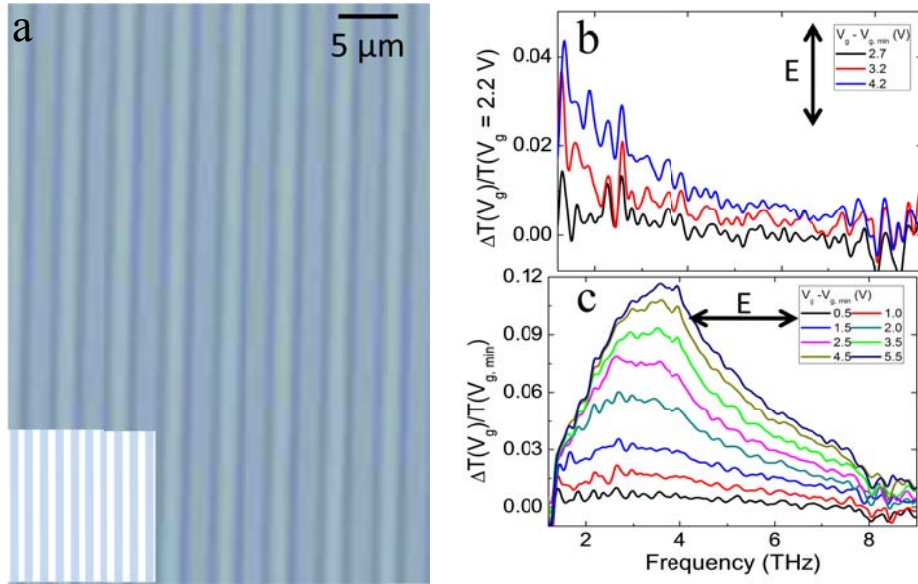
$$q = \frac{N\pi - \delta}{W} \quad (7.2)$$

where  $N$  is the harmonic order of the plasmonic mode, and  $\delta$  is a phase shift upon reflection at the graphene edge. Numerical results indicate that  $\delta = \pi/4$  for termination by dielectric [130, 131]. Then the plasmon resonance frequency for a graphene ribbon is given by:

$$\omega_p = \left( \frac{3\pi^{3/2}v_F e^2}{\hbar(\varepsilon_1 + \varepsilon_2)} \right)^{1/2} \frac{n^{1/4}}{W^{1/2}} \quad (7.3)$$

Experimentally, plasmon resonances in graphene have been previously studied in exfoliated graphene samples by using infrared nano-imaging [132, 133] and by Fourier transform infrared spectroscopy (FTIR) in arrays of microribbons or disks patterned from large-area chemical vapor deposition-grown graphene [68, 73]. The

devices demonstrated in this chapter are fabricated using epitaxial single-layer graphene on (0001) semi-insulating (resistivity  $> 10^9 \Omega\text{-cm}$ ) 6H-SiC. The 2D graphene is patterned into a ribbon array using electron beam lithography with 400 nm thick PMMA resist as an etch mask and oxygen plasma treatment to remove exposed graphene as introduced in previous chapters. The carrier density of graphene is tuned by the  $\text{LiClO}_4/\text{PEO}$  electrolyte top gate (see Chapter 3.1.2), which covers the device on its top surface. Considering the dielectric constant of SiC ( $\epsilon_1 \sim 9.6$ ) and PEO electrolyte top gate ( $\epsilon \sim 3$ ), the plasmon frequency in Eqn. (7.3) can be expressed as:  $f_p = \omega_p/2\pi = 2.73 \text{ THz} \times [n (10^{12} \text{ cm}^{-2})]^{1/4} \times [W (\mu\text{m})]^{-1/2}$ .



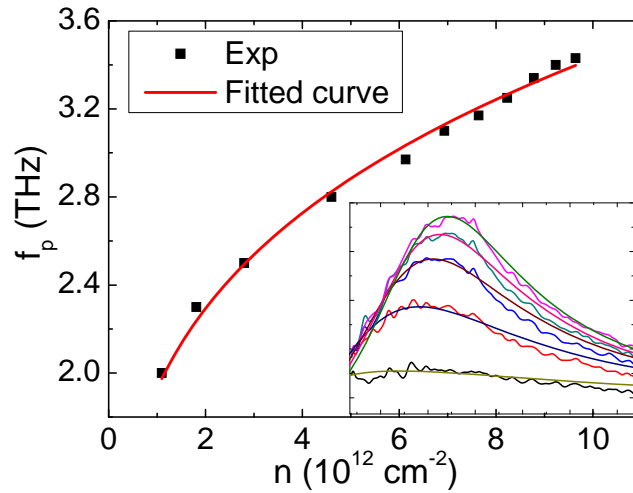
**Figure 7.1** (a) Optical micrograph of a graphene ribbon array with no metal. The inset shows the corresponding schematics. Attenuation spectra at different gate voltages  $V_g$  are shown with incident electric field polarized vertical (b) and horizontal (c). Spectra are normalized by the spectrum at  $V_g = V_{g, \min} + 2.2 \text{ V}$  (b) and  $V_g = V_{g, \min}$  (c).

Fig. 7.1a shows the optical micrograph of the sample with patterned electron-beam resist on top (the graphene on SiC is not easily visible in optical microscopy). The total array size is  $2 \text{ mm} \times 2 \text{ mm}$ , the ribbon width is  $2.3 \mu\text{m}$ , and the period of the array is  $4.6 \mu\text{m}$ . The response of the device to THz excitation is characterized by FTIR (experimental set-up shown in Section 3.6): To minimize time drift of the signal,

transmitted spectrum through the device and an identical bare aperture placed in the sample position is consecutively measured at each gate value and their ratio gives the absolute transmission. The attenuation spectra with the excitation polarized perpendicular and parallel to the ribbon are plotted in Fig. 7.1b and 7.1c, respectively. The attenuation in this work is defined as  $1-T(V_g)/T(V_{g, \min})$ , where  $T(V_g)$  and  $T(V_{g, \min})$  are the transmission at the gate voltage  $V_g$  and the charge neutral point, respectively. Note that here, the spectra are normalized to the transmission at the charge neutral point  $V_{g, \min}$  in Fig. 7.1c and to the transmission at  $V_g = V_{g, \min} + 2.2$  V in Fig. 7.1b (in this case data were not taken for the charge neutral point, so normalization was done using data at the lowest carrier density). The gate voltage  $V_g$  is applied through the electrolyte top gate to tune the carrier density in graphene. As shown in Fig. 7.1b, a Drude response is observed, where the attenuation decreases monotonically with the frequency. A completely different lineshape is seen for the attenuation spectra in Fig. 7.1c, when the incident light is polarized perpendicular to the ribbons, where an enhanced absorption associated with excitation of the intrinsic plasmon is observed. In this device, where the ribbon width is fixed, a blue shift of  $f_p$  is observed when increasing  $n$  by raising the gate voltage.

Next I model the plasmonic relative attenuation through the device at different gate voltages shown in Fig.7.1c. In principle, the Drude spectra shown in Fig. 7.1b can be modeled as well. But unfortunately, the fact that the spectrum at  $V_g = V_{g, \min}$  was not taken, and instead all spectra are normalized by the spectrum at  $V_g = V_{g, \min} + 2.2$  V, makes the modeling more complicated. The first step is to calculate the transmission of the graphene ribbons according to Eqn. (2.2). In this device,  $n_1 = 1.73$  and  $n_2 = 3.1$  are the refractive index of the electrolyte and SiC substrate. The ac conductivity  $\sigma$  can be written as  $\sigma_d = \sigma_0/(1 + i\omega\tau)$  for the Drude response as shown in Eqn. (2.6) and  $\sigma_p = \sigma_0/(1 + i(\omega^2 - \omega_p^2)\tau/\omega)$  for the plasmon excitation as shown in Eqn. (2.18). Note that in this chapter  $\omega_p$  is used to represent the plasmon resonance

frequency. Both the dc conductivity  $\sigma_0$  and the electron scattering time  $\tau$  can be expressed as a function of the carrier density  $n$  and mobility  $\mu$  of graphene, written as:  $\sigma_0 = ne\mu$  and  $\tau = \sqrt{\pi n} \hbar \mu / ev_F$ , where  $e$  is elementary charge and  $v_F$  is the Fermi velocity. The relative attenuation is then expressed as  $\Delta T = 1 - \frac{T(V_g)}{T(V_{g,min})}$ .



**Figure 7.2** Plasmonic resonance frequency  $f_p$  as a function of carrier density  $n$  for the device shown in Fig. 7.1. Black points are extracted from fits of the data in Fig. 7.1c as described in text. Fits to data in Fig. 7.1c are shown as solid lines in inset. Red line: fit to Eqn. (7.3) in text.

To fit the attenuation spectra shown in Fig. 7.1c, a fixed  $\mu = 1300 \text{ cm}^2 \cdot \text{V}^{-1} \cdot \text{s}^{-1}$  is taken and  $n$ ,  $\omega_p$  are set as fitting parameters. I then plot in Fig. 7.2 the modeled  $f_p$  vs.  $n$  with a fit to Eqn. (7.3), which gives  $f_p = 1.92 \text{ THz} \times [n (10^{12} \text{ cm}^{-2})]^{1/4}$ . The prefactor 1.92 is very close to the expected value of 1.80 found from Eqn. (7.3) with  $W = 2.3 \text{ } \mu\text{m}$ . The inset of Fig. 7.2 shows the individual fits to selected curves from Fig. 7.1c.

One hypothesis made in the modeling is that the mobility is independent of the carrier density, which is generally a good assumption for moderately doped exfoliated graphene. However, whether it is true for epitaxial graphene on SiC is still unknown. Moreover, when gating using the electrolyte top gate, the counter ions (whose

concentration depends on gate voltage) are close to the graphene surface and may act as additional disorder to scatter mobile electrons and make the mobility of the device dependent on the carrier density.

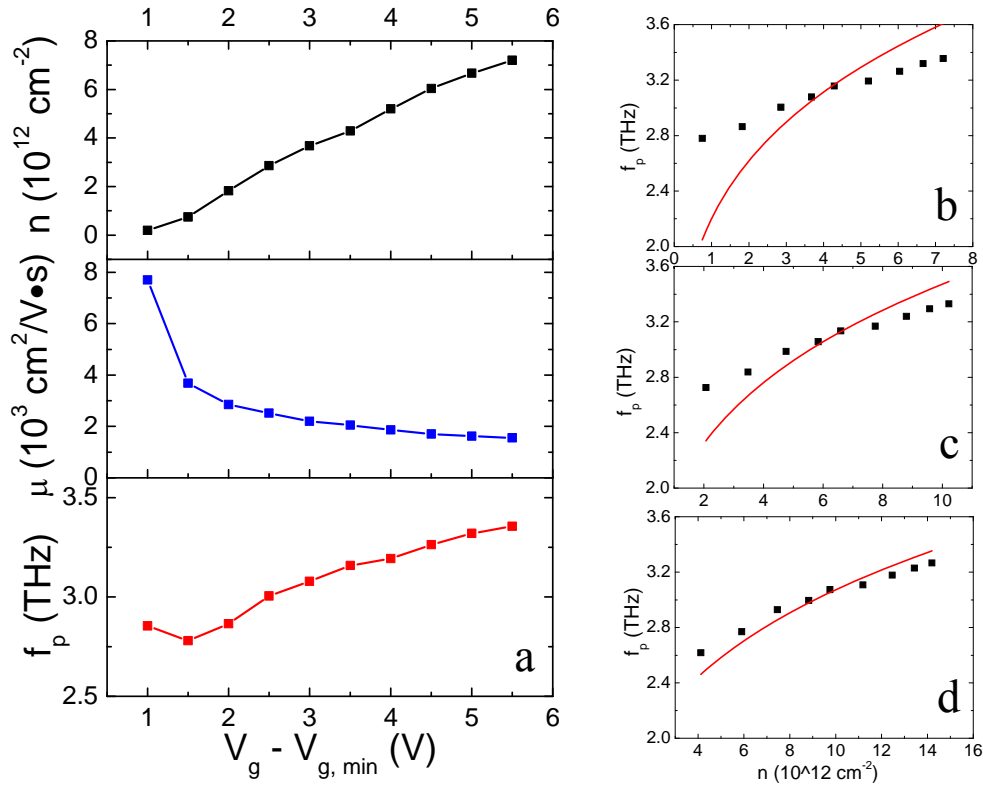


**Figure 7.3** (a) Carrier density  $n$ , mobility  $\mu$ , and plasmonic resonance frequency  $f_p$  extracted from fits as a function of the gate voltage for the device shown in Fig. 7.1. (b, c, d) Plasmonic resonance frequency  $f_p$  as a function of carrier density  $n$  for the device shown in Fig. 7.1. Black points are extracted from fits of the data in Fig. 7.1c by assuming  $n_{\text{puddle}} = 0 \text{ cm}^{-2}$  (b),  $n_{\text{puddle}} = 0.75 \times 10^{12} \text{ cm}^{-2}$  (c) and  $n_{\text{puddle}} = 1.75 \times 10^{12} \text{ cm}^{-2}$  (d). Red line: fit to Eqn. (7.3) in text.

I therefore tried to fit the attenuation spectra again using the same method introduced before but set  $\mu$  as the third fitting parameter. The results are shown in Fig. 7.3a. The carrier density, mobility, and the plasmon resonance frequency extracted from fits are shown at different top gate voltages, respectively. The best fits indicate a mobility which decreases as gate voltage (and carrier density) increase, which is consistent with the counter ions of the electrolyte contributing additional scattering



and reducing the mobility at high gate voltage. According to this,  $f_p$  can be plotted as a function of  $n$ , similarly to that shown in Fig. 7.2. However, I now observe that the data points are poorly described by Eqn. (7.3), as shown in Fig. 7.3b. One possible reason is that the carrier density  $n$  was assumed to be 0 at the charge neutral point, which is not true in the real device due to disorder-induced electron-hole puddles. To compensate for this, phenomenologically an additional fixed carrier density (corresponding to the puddle density) is added to the carrier density of the sample at all gate voltages. Fig 7.3c and 7.3d then show the plasmonic resonance frequency  $f_p$  as a function of carrier density  $n$  extracted from fits by assuming a puddle density of  $0.75 \times 10^{12} \text{ cm}^{-2}$  and  $1.75 \times 10^{12} \text{ cm}^{-2}$ , respectively. Fits of the data shown in Fig. 7.3c and 7.3d give  $f_p = 1.95 \text{ THz} \times [n (10^{12} \text{ cm}^{-2})]^{1/4}$  and  $f_p = 1.73 \text{ THz} \times [n (10^{12} \text{ cm}^{-2})]^{1/4}$ . It is noticed that the assumed puddle density is higher than previously reported [50] in exfoliated graphene. It is possible that the electrolyte covered epitaxial graphene is different from exfoliated samples, but this needs more experimental evidence to be confirmed.

In summary, both theoretical expectation and experimental demonstration of the plasmon mode in a graphene microribbon array on SiC are presented in this section, representing the first observation of the standing wave plasmons in monolayer epitaxial graphene on SiC substrates. The attenuation spectra can be well fitted by assuming graphene's mobility is independent of the carrier density. More evidence and analysis are needed to verify whether or not this assumption is reasonable.

## 7.2 Drude response and standing wave plasmons in graphene-metal microstructures

To be used as a photodetector, graphene elements need to be connected via some conductive material to form a closed electrical circuit. Additionally it is expected that detectors exploiting hot electron effects will require electrode spacings shorter than the diffusion length of electrons within the electron-phonon scattering time, which

depends on the mobility of the device. In the large area graphene samples presented in this work this number is expected to be less than few microns [83, 93], far smaller than the THz wavelength in free space ( $\sim 100 \mu\text{m}$ ). Therefore, next I will explore graphene microribbon arrays contacted by metal electrode arrays with few-micron spacing.

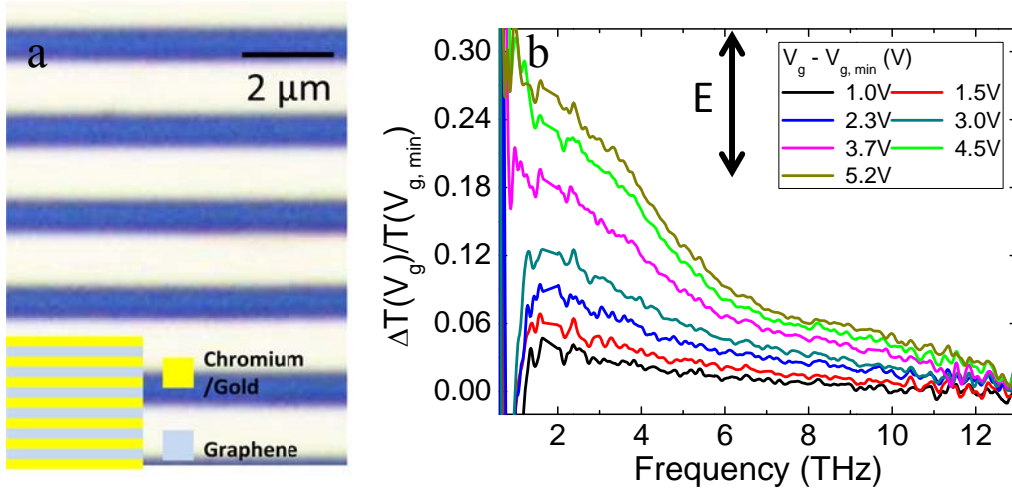
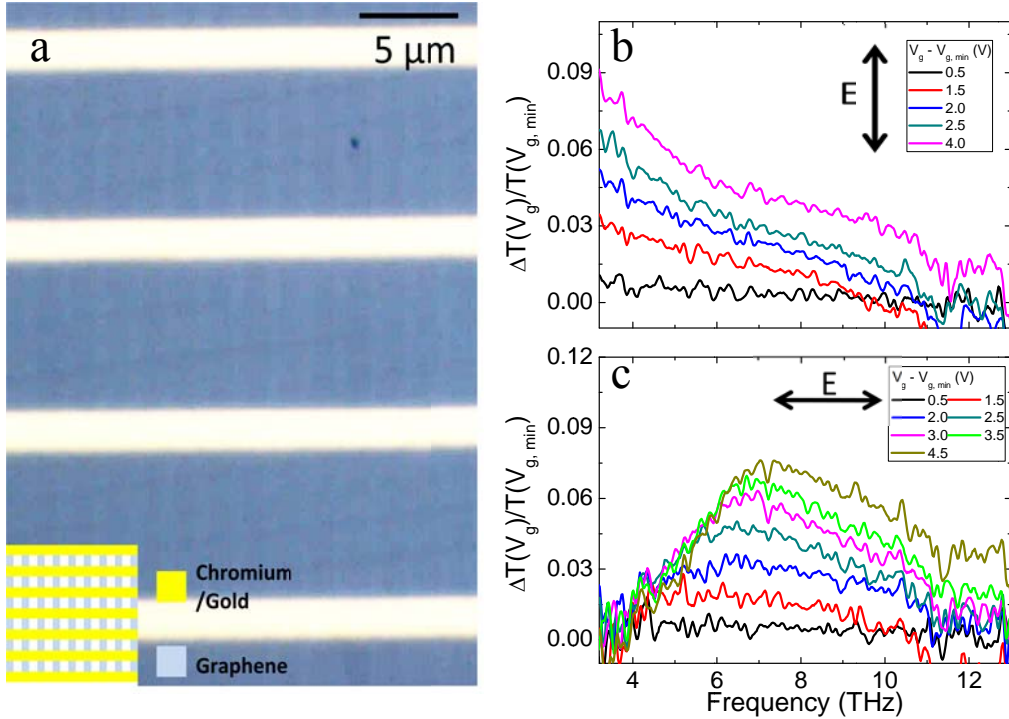


**Figure 7.4** (a) Optical micrograph of unpatterned graphene sheet on SiC substrate with metal grating on top. Inset: Schematic of the device. (b) Attenuation spectra at different gate voltages normalized by the spectrum at  $V_g = V_{g, \min}$  with incident electric field polarized vertical.

Fig. 7.4a shows an array of metal electrodes (4 nm chromium and 45 nm gold; deposited using standard e-beam lithography followed by thermal evaporation) on top of continuous graphene. The electrode width is  $1.3 \mu\text{m}$  and spacing is  $0.7 \mu\text{m}$ . The metal-grating-covered area is  $2 \text{ mm} \times 2 \text{ mm}$  (The optical micrograph of a similar device with zoomed-out view is shown in Fig. 3.6b). Fig. 7.4b shows the attenuation spectra at different gate voltages for excitation polarized perpendicular to the grating. Since graphene ribbon width here is about 3 times smaller than the device shown in Fig. 7.1a, the plasmon frequency is expected to be  $\sqrt{3}$  times higher. However, there is no well defined plasmon attenuation peak apparent in the spectrum. Instead, a Drude-like response is observed. This can be attributed to different boundary conditions in metal-contacted vs. dielectric-terminated graphene ribbons [134, 135]. The metal

contacts are, in effect, antennas, whose resonant frequency is far from matched to the plasmons in graphene. The plasma currents in the graphene are controlled by the currents induced in the contacts by the radiation field and these currents fall off like  $(W_m/\lambda)^2$  at long wavelengths, where  $W_m$  is the width of the metal. This leads to weak dipole strength even for the even modes, while the odd modes have zero dipole strength by symmetry. However, narrow contacts are required to maximize the fill factor of the graphene elements. It is hence expected the plasmon modes to be only weakly excited in this geometry. Indeed, the broad weak feature seen at in Fig. 7.4b probably corresponds to this weakly excited  $N = 2$  plasmon mode. More careful characterization is needed to confirm this and to understand better the plasmon mode excitation in metal contacted graphene ribbons. One promising way to study this is to use high mobility graphene to achieve sharper plasmon resonance and vary either the width of graphene ribbons or metal ribbons to systematically monitor the change of the attenuation spectra. The experimental result can be compared with simulated spectra, in order to collect more useful information. This work is currently being performed in Prof. Drew's group.

In a word, the above results indicate that metal termination of graphene to form finite-width ribbons is not sufficient to define a plasmon resonance that can be efficiently excited by light. However metal electrodes are necessary for electrical detection schemes. To circumvent this difficulty, I next investigated devices in which large area graphene is first patterned into a ribbon array using e-beam lithography and then a metal electrode grating is deposited on top of the array by repeating the standard e-beam lithography one more time followed by a thermal evaporation. Here the metal electrodes can be oriented at an angle to the ribbons. In the first case, I explore a device in which the metal electrodes are orthogonal to the graphene ribbons.



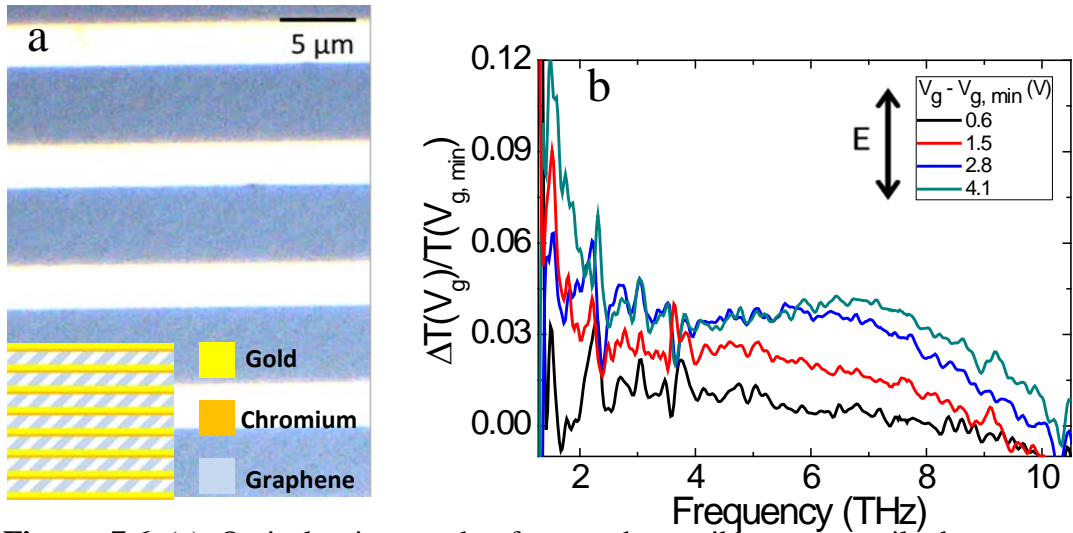
**Figure 7.5** (a) Optical micrograph of a graphene ribbon array oriented orthogonal to a metal electrode grating. The inset shows the corresponding schematics. Attenuation spectra at different gate voltages  $V_g$  are shown with incident electric field polarized vertical (b) and horizontal (c). Spectra are normalized by the spectrum at  $V_g = V_{g, min}$ .

Fig. 7.5a shows the optical micrograph of the device. The vertical graphene ribbons, faintly visible in Fig. 7.5a, are  $0.6 \mu\text{m}$  wide with a period of  $2 \mu\text{m}$ . The horizontal chromium/gold (4 nm/45 nm) electrodes were patterned on top of the graphene ribbons with an electrode width  $1.7 \mu\text{m}$  and period  $9 \mu\text{m}$ . Fig. 7.5b and 7.5c show the measured attenuation spectra for two polarization cases. When the incident terahertz signal is polarized parallel to the microribbons, a Drude-like response is shown in Fig. 7.5b similar to Fig. 7.4b. For polarization perpendicular to the ribbons, a plasmon resonance is observed in Fig. 7.5c similar to Fig. 7.1c. Because the ribbons are  $\sim 4\times$  narrower, the resonant frequency is higher by a factor of  $\sim 2$ . Additionally, comparing Fig. 7.1c and 7.5c, it is found that the strength of the plasmon resonance is reduced in the metal-contacted case and is smaller than the strength of the resonance for the uncontacted ribbons. This is a consequence of the sub-wavelength metal

grating, which strongly reflects for fields that are polarized parallel to the electrodes. The extinction coefficient of metal wire gratings scales in proportion to  $(d/\lambda)^2$  at long wavelengths, where  $d$  is defined as the electrode spacing. This is a significant disadvantage of this scheme, since it is expected that detectors will require even smaller electrode spacings on the micron scale limited by the diffusion length.

### 7.3 Transmission of graphene ribbon array tilted to metal electrodes

#### 7.3.1 Device with large electrode spacing



**Figure 7.6** (a) Optical micrograph of a graphene ribbon array tilted to a metal electrode grating. Inset: Schematic of the device. (b) Attenuation spectra at different gate voltages normalized by the spectrum at  $V_g = V_{g, min}$  with incident electric field polarized vertical.

To overcome the difficulties above, a new design is adopted with graphene ribbons tilted at an angle with respect to the metal grating, as shown in Fig. 7.6a. In this device, the period of the graphene ribbon array is  $2 \mu\text{m}$  and the ribbon width is  $0.6 \mu\text{m}$ , similar to the device in Fig. 7.5. Bi-metal electrodes (20 nm chromium + 25 nm gold) are deposited on graphene ribbons using the two-step shadow evaporation technique. The inter-electrode spacing is  $5.7 \mu\text{m}$ , and were inclined at an angle of  $\theta = 45$  degrees with respect to the metal contacts. Light polarized perpendicular to the

metal grid (which does not suffer from the polarizer effect) now has an electric field component perpendicular to the graphene ribbon axis and can therefore excite the transverse plasmon resonance. In this case, when the incident terahertz radiation is polarized perpendicular to the metallic grating, one can see evidence of gate-tunable plasmonic absorption in the attenuation spectrum, as shown in Fig. 7.6b. This is in contrast to Fig. 7.5b, where no plasmonic resonance can be seen for light polarized perpendicular to the metal electrode grating.

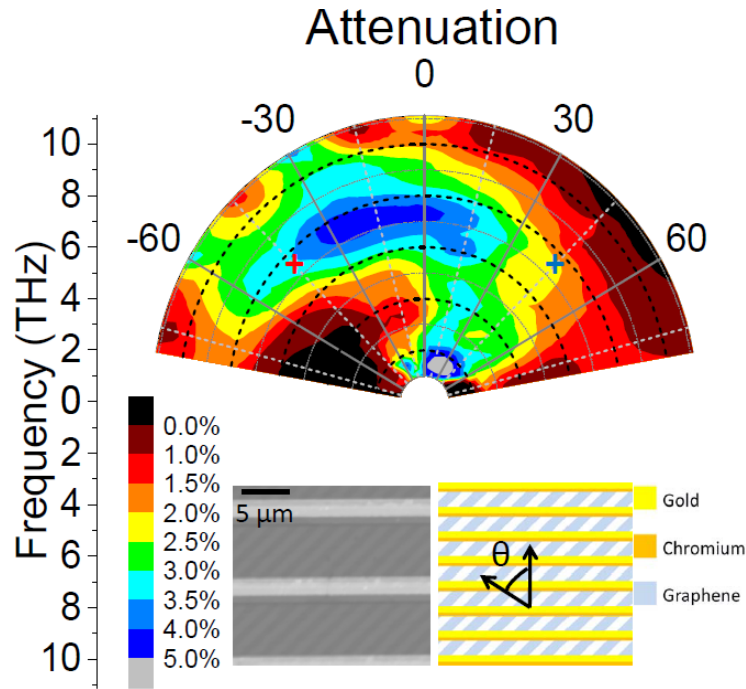


**Figure 7.7** The attenuation at  $V_g = V_{g, min} + 5.4$  V is shown as a function of the frequency (radial axis) and the incident polarization (azimuthal axis). Inset: A scanning electron micrograph of a similar device (left) and the schematic of the device with the defined polarized angle  $\theta$  of the incident light (right). Graphene ribbon is tilted  $45^\circ$  to the metal electrodes.

I further explore the polarization dependence of the tilted-ribbon array. Fig. 7.7 shows a color map of the polarization-dependent attenuation of the tilted ribbon array as described in Fig. 7.6 at  $V_g = V_{g, min} + 5.4$  V, which is the highest gate voltage (highest carrier density) achieved in this experiment. The color scale indicates the normalized attenuation defined as  $A = (1 - T_{high}/T_{low}) \cdot f(\omega, \theta)$ , where  $T_{high}$  is the

transmission at  $V_g = V_{g, \min} + 5.4 \text{ V}$ ,  $T_{\text{low}}$  is the transmission at  $V_g = V_{g, \min}$ , and  $f(\omega, \theta)$  is the experimentally determined extinction factor of the metal grating.  $f(\omega, \theta)$  is defined as  $f(\omega, \theta) = \cos^2(\theta) + \sin^2(\theta) \cdot \Phi(\omega)$ , where  $\Phi(\omega) \in [0,1]$  is the ratio of the measured transmission at  $\theta = 90^\circ$  and  $0^\circ$  when the device is at the charge neutral point. Here, the attenuation is plotted as a function of frequency (plotted along the radial direction) and polarization angle, as defined in the inset schematic. The left inset of Fig. 7.7 shows an SEM image of a similar device fabricated in the same way. Because the attenuation is multiplied by  $f(\omega, \theta)$ , the effect of the metal grating is included, and the polarization dependence is due to both the attenuation caused by graphene and metal grid. Additionally, the metal grid is symmetric with respect to polarizations at positive and negative angles  $\pm \theta$ , so asymmetry for  $\pm \theta$  is caused by the tilting of graphene with respect to the metal grid. Indeed, a highly asymmetric pattern of attenuation is observed. When the angle of polarization is inclined in the direction parallel to the graphene ribbons ( $\theta > 0$ ), a Drude-like absorption spectrum is observed, which decreases monotonically with frequency. By contrast, when the angle of polarization is inclined in the direction perpendicular to the ribbons ( $\theta < 0$ ), a peak in attenuation at  $\sim 7.4 \text{ THz}$  is observed, which is identified as the plasmon resonance frequency for these ribbons at this gate voltage.

Figs. 7.8a and 7.8b show the simulated charge density oscillations in the device structure at this frequency for two polarization angles  $\theta = \pm 45^\circ$  (parallel and perpendicular to the ribbons), respectively. The charge density oscillation at the plasmon resonance frequency was obtained using a finite element method frequency-domain simulation, carried about by M. Jadidi and Prof. Thomas Murphy. Plane-wave excitation (7.4 THz) was simulated with a polarization parallel and perpendicular to graphene ribbons. The geometrical parameters of the element are the same as the real device described above. The carrier density of graphene was taken to be  $2 \times 10^{13} \text{ cm}^{-2}$ . The mobility was taken to be  $5000 \text{ cm}^2 \cdot \text{V}^{-1} \cdot \text{s}^{-1}$ , which is possibly

higher than that of the real device, in order to illustrate the plasmon mode more clearly. The displayed figure shows the moment when the charge density oscillates to its maximized amplitude.

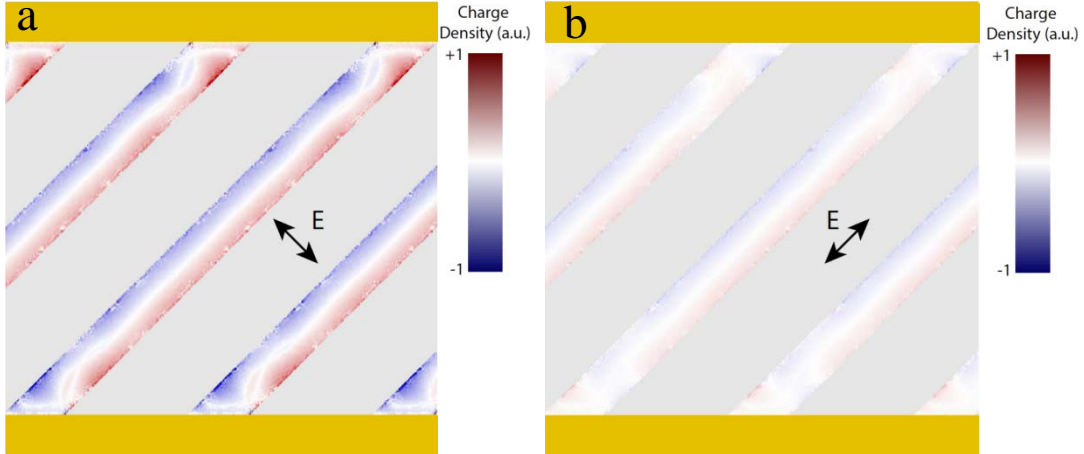


**Figure 7.8** Simulated charge density profile in the graphene/metal microstructure at the plasmon resonance frequency. The polarization of the incident plane-wave (7.4 THz) is perpendicular to the graphene ribbons in (a) and parallel in (b), corresponding to the points marked with red and blue “+” symbols in Fig. 7.7, respectively. The same color scale is used for both figures.

Compared to Fig. 7.8b, which shows a very weak charge density oscillation, Fig. 7.8a clearly displays a charge density wave excited by the incident electric field polarized perpendicular to the ribbons, which supports the identification of the observed attenuation peak at 7.4 THz and  $\theta < 0$  as the transverse plasmon in the graphene-metal microstructure.

### 7.3.2 Device with small electrode spacing

Next, I will discuss a similar device, but with a smaller electrode spacing more compatible with enhanced photothermoelectric detection. The device is fabricated using the same technique as the device shown in Fig. 7.6, but here the graphene ribbon width is  $1.1 \mu\text{m}$  and the inter-electrode spacing is  $3.8 \mu\text{m}$ . The two-step shadow evaporation technique for asymmetric metal electrodes deposition is used, so that each graphene channel (light sensitive part of the detector) has asymmetrical



contacts (gold contact on the bottom edge and chromium contact on the top edge), which helps to generate a net photothermoelectric signal when the device is uniformly illuminated.

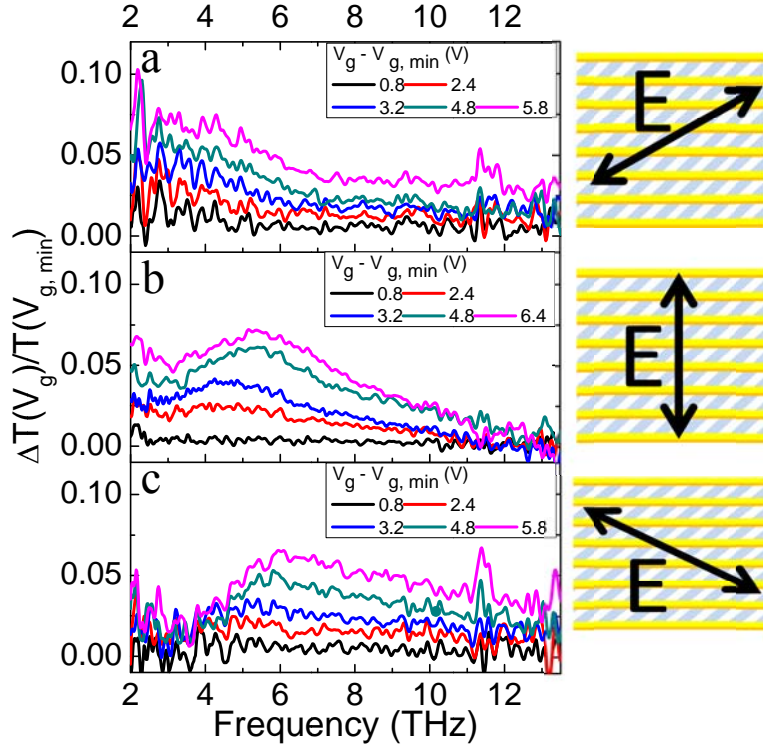


**Figure 7.9** The attenuation at different  $V_g$  normalized by the spectrum at  $V_{g, \min}$  as a function of frequency shown for the incident polarized angle:  $\theta = 60^\circ$  (Drude response) (a),  $0^\circ$  (combined response) (b),  $-60^\circ$  (Plasmon response) (c). The right column shows schematics of the device and the polarization of the incident light for each measurement, respectively.

Fig. 7.9 shows the attenuation spectra at different gate voltages for the incident light polarized with three typical angles. At  $\theta = 60^\circ$  (Fig. 7.9a) due to the polarizing effect of the metal grid which reduces the parallel component of the electric field, the effective electric field interacting with graphene is nearly parallel to the ribbons, resulting in a dominant Drude response. At  $\theta = -60^\circ$  (Fig. 7.9c), the effective electric

field is close to perpendicular to the graphene ribbons, which excites the transverse plasmons in the graphene ribbon, leading to increased attenuation at the plasmon resonant frequency which is in the range 4-6 THz. As expected, the resonant frequency increases with charge carrier density by applying a gate voltage. Interestingly, at  $\theta = 0^\circ$  (Fig. 7.9b), the angle at which the incident light is minimally absorbed by the metal grid, a combined response is observed, especially at high gate voltage. Here the components of the electric field parallel and perpendicular to graphene ribbons are nearly equal. At the highest gate voltage (magenta curve), the attenuation shows a local plasmonic peak at  $f \sim 5.3$  THz and also a Drude response at low frequency.

Next I will study the frequency and the polarization angle dependence of the attenuation at large positive gate voltage in more detail. Fig. 7.10a shows the attenuation of the same device studied in Fig. 7.9 at  $V_g = V_{g, min} + 6.5$  V, the highest gate voltage (carrier density) achieved. Similar to Fig. 7.7, the color scale indicates the normalized attenuation, corrected by the extinction factor  $f(\omega, \theta)$ , which is defined before for Fig. 7.7. As shown in Fig. 7.10a, the attenuation peaks near  $\theta = 0^\circ$ , because the metal grating reflects a large portion of the incident light polarized in other directions owing to the small spacing between metal electrodes. There is a local maximum at the frequency of  $\sim 5.3$  THz corresponding to plasmon-enhanced attenuation, which is clearly separated from the Drude response at  $f < 3$  THz. The plasmon peak is asymmetric in polarization angle with more weight at negative angle, while the Drude response occurs at positive angle.

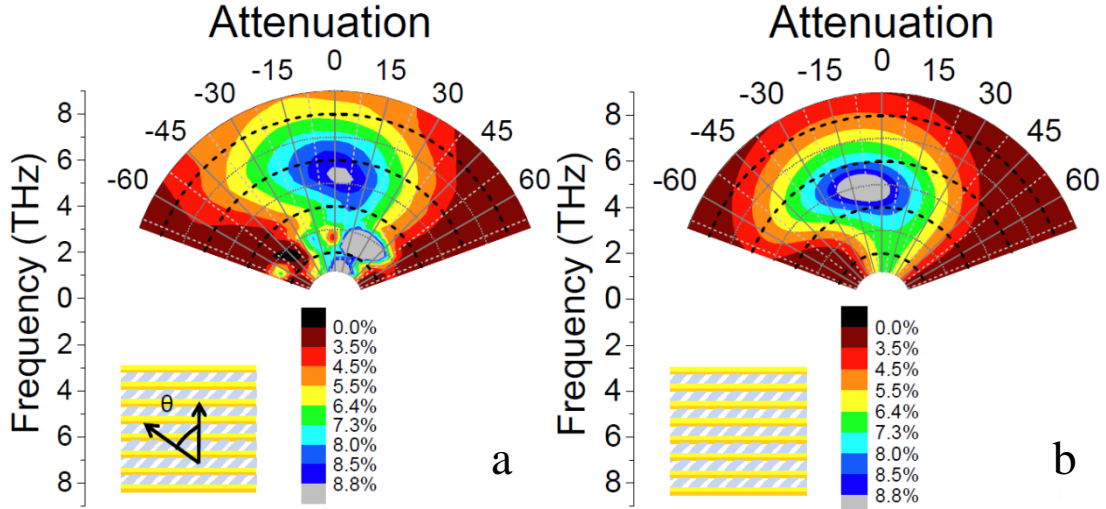


**Figure 7.10** (a) Experimental attenuation at  $V_g = V_{g, min} + 6.5$  V as a function of frequency (radial axis) and the incident polarization (azimuthal axis). (b) Simulated attenuation of the device shown in (a) using the model discussed in the text. The inset of (a) shows a schematic of the device and defines the polarization angle  $\theta$ .

To understand the relationship between plasmonic excitation and polarization, a simple plasmon conductivity model is developed to predict the expected absorption in the graphene ribbons. When modeling the spectra, I first project the effective electric field (the electric field of the incident light corrected by the factor  $f(\omega, \theta)$ ) to the axes parallel and perpendicular to graphene ribbons. The parallel and perpendicular components contribute to a Drude and plasmonic absorption, respectively. Considering the perturbation of metal electrodes, I assume that the plasmon mode does not extend over the full length of the strip. It is estimated that it covers  $\sim 80\%$  of the area of the strip. The transmission of the graphene ribbons is described by the same thin-film expression as explained before. In this device,  $\mu$  is taken to be  $800 \text{ cm}^2 \cdot \text{V}^{-1} \cdot \text{s}^{-1}$  and  $n$  is  $1.6 \times 10^{13} \text{ cm}^{-2}$ . The standing wave plasmon frequency  $\omega_p$  is given by Eqn. (7.3). The modeled attenuation is plotted in Fig. 7.10b in the same way as the experimental data shown in Fig. 7.10a. The only free parameters of the model are the carrier density  $n = 1.6 \times 10^{13} \text{ cm}^{-2}$  and the mobility of graphene  $\mu = 800 \text{ cm}^2 \cdot \text{V}^{-1} \cdot \text{s}^{-1}$  which determines  $\tau = 37 \text{ fs}$ . According to the model, the resistivity of the device at this gate voltage is  $\sim 500 \Omega$ , which is lower than the measured resistivity  $1.4 \text{ K}\Omega$ .

This difference is attributed to the contact resistance contribution, in the two-probe transport measurement across multiple graphene/metal junctions. The model reproduces the features of the experimental data: a stronger attenuation peak at finite frequency is both predicted and observed when the angle of polarization is inclined towards the direction perpendicular to the graphene ribbons, which signifies the excitation of a transverse plasmonic resonance.

#### 7.4 Plasmon enhanced THz photoresponse

Next we discuss the electrical response to THz radiation of the same device as in Figs. 7.9 and 7.10. Photoresponse measurements were performed using the continuous wave THz laser at 5.3 THz as the source shown in Fig. 3.8, similar to the set-up used in Chapter 4.2.2 for the THz photovoltage measurement. The open-circuit photovoltage signal is characterized using a voltage preamplifier and lock-in amplifier. The sample is mounted on the same copper plate as in the FTIR measurements (see Fig. 3.12b) and the beam illuminates the device through the SiC substrate to avoid the absorption by the electrolyte. A rotating polarizer (also see Chapter 3.6) is placed in front of the focusing parabolic mirror ( $D = F = 50$  mm). The photovoltage is continuously normalized by the signal of the pyroelectric reference detector. The sample is mounted on an x-y-z scanning stage together with another pyro-detector, which is used for the power calibration (including signal for rotating polarizer).

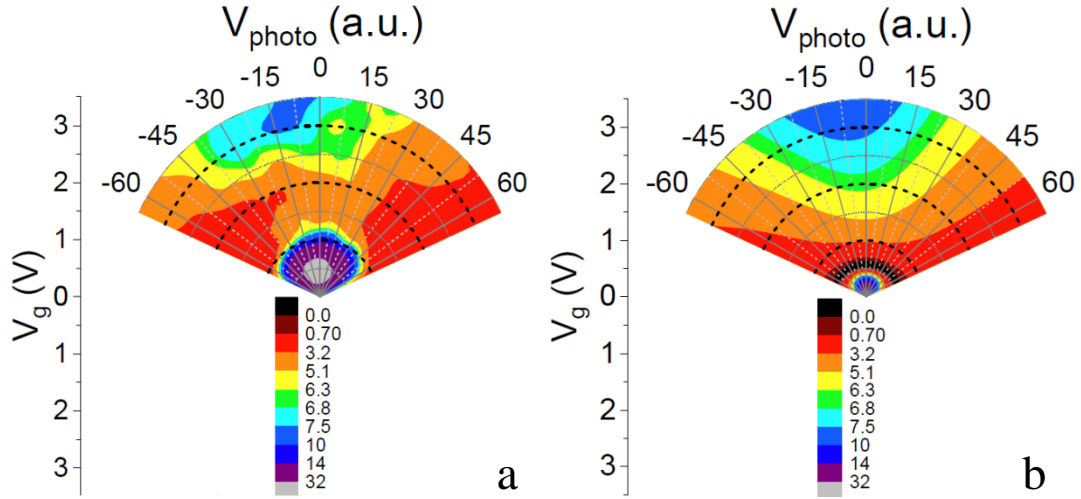


**Figure 7.11** (a) Measured magnitude of the photovoltage for a tilted graphene ribbon array photodetector as a function of  $V_g$  (radial axis) and the incident polarization (azimuthal axis). The device is the same as in Fig. 7.10a and the frequency of the laser excitation is 5.3 THz ( $175 \text{ cm}^{-1}$ ). (b) Simulated photoresponse of the same device using the model discussed in the text.

Fig. 7.11a shows the photovoltage as a function of the applied top gate voltage (radial axis, measured relative to the charge neutral point) and the polarization angle of the CW excitation (azimuth). As shown previously [129], the photovoltage is generated by the photothermoelectric effect [83] in graphene due to asymmetry of the electrodes. As reported in [129], this type of asymmetry leads to photothermoelectric voltage that is peaked near the Dirac point and monotonically decreases with the carrier density in highly doped sample. Fig. 7.11b shows the modeled photoresponse as function of gate voltage and polarization angle, using the same parameters as in Fig. 7.10b, and a photothermoelectric model described in Chapter 4.4. It is assumed that the electron temperature rise of each graphene ribbon element from the absorbed THz radiation is determined by the thermal conductance. Since metal contacts stay at room temperature, a temperature profile across the ribbon is generated. The thermoelectric voltage is calculated as  $V = \int dx S \cdot \nabla T$ , where  $\nabla T$  is the electron temperature gradient and  $S(x)$  is the Seebeck coefficient of graphene. The asymmetric metal contacts produce a net thermoelectric signal via (1) nonuniformity in  $S(x)$

across the device due to chemical potential pinning [115] at the graphene/metal interface and (2) asymmetric temperature profile due to different contact resistance [116]. Comparing the device here with the device shown in Chapter 4.4 (also see [129]), which is bi-metal contacted exfoliated graphene on SiO<sub>2</sub> substrate, the same value for metal work functions and a different value for contact resistance are assumed. The observed photoresponse is best described by an additional contact resistance  $R_c = 35 \Omega$  at the region from the gold contact extending 130 nm inside the graphene (the corresponding extra contact resistivity  $\rho_c = 300 \Omega$ ), somewhat less than was found for exfoliated graphene devices on SiO<sub>2</sub> substrates [129].

Both the experimental and modeled signals show maxima at small gate voltages where the photothermoelectric responsivity peaks [86, 87]. In addition, when the gate voltage is low, the photovoltage is symmetric around  $\theta = 0^\circ$  as the plasmon is only weakly excited in the low doped region. The signal for this device with a small metal spacing depends primarily on the polarizer effect of the metal electrodes and thus peaks with angle near  $\theta = 0^\circ$ . At larger gate voltages the photoresponse increases with increasing gate voltage. This rise is not due to increased responsivity; as observed earlier [129] and explained within the asymmetric metal electrodes model the responsivity decreases monotonically with increasing gate voltage at high gate voltage. Instead, the increase is explained by enhanced absorption in the device, which is due to (1) increase in dc conductivity with increased gate voltage, and (2) resonant plasmonic absorption. The shift of the peak in photoresponse with respect to angle to  $\theta < 0^\circ$  clearly indicates that the plasmonic effect is dominant in increasing the absorption, similar to Figs. 7.10a and 7.10b.

### 7.5 Conclusion and outlook

To conclude, the plasmon resonance absorption in large area arrays of epitaxial graphene microribbons contacted by metal electrodes is demonstrated. It is shown

that if the opposing edges of the microribbons are directly contacted by metal electrodes, the altered boundary conditions at the graphene-metal interface and associated currents in the metal [134, 135] make it difficult to directly excite plasmon resonances. In contrast, if the ribbons are oriented perpendicular to the metal electrodes, then the sub-wavelength metal electrode pattern reflects the incident wave with the necessary polarization perpendicular to the ribbons and parallel to the electrodes, greatly reducing the plasmonic excitation.

Therefore, a novel geometry of graphene microribbons tilted at an angle with respect to the electrode array is adopted, in which the plasmon mode associated with currents transverse to the ribbon can be efficiently excited by light polarized perpendicular to the metal electrodes. By using dissimilar metal electrodes a photothermoelectric detector is formed from the tilted graphene microribbon array. An enhanced photovoltage is observed when the carrier density of graphene is tuned such that the plasmon resonance frequency matches the THz continuous-wave excitation. The frequency and polarization-angle dependent absorption and the gate voltage and polarization-angle dependent photoresponse are well described by a simple plasmonic conductivity model for graphene.

The scheme demonstrated in this chapter enhances the absorption of radiation by graphene and therefore increases the external efficiency of graphene photothermoelectric detectors. Additionally the plasmon resonance is tunable through both geometry (ribbon width) and carrier density, enabling spectral resolution and tunability in graphene photothermoelectric detectors. However, in the device demonstrated here, the gains are modest; the attenuation for plasmonic excitation in Fig. 7.9c is barely greater than that for Drude absorption in Fig. 7.9a. One reason is that the spectral resolution quality factor is  $Q = \omega_p\tau = 1.2$ , limited by the fairly low mobility of epitaxial graphene. Low mobility also broadens the Drude response farther into the THz. The quality factor could be enhanced by etching graphene into

narrower ribbons, shifting the plasmon resonance to higher frequency. However, this neither increases the absorption at the resonance peak, nor reduces the bandwidth of the plasmon. Moreover, for extremely narrow graphene ribbons, the plasmon resonance broadens because of edge scattering, which makes the device even less efficient [136]. Increasing the carrier density will increase the spectral weight of the plasmon resonance and hence the absorption. The quality factor is also improved, since the resonance frequency shows a blue shift with increasing carrier density. However, the Seebeck coefficient decreases with carrier concentration, leading to a weaker thermoelectric response in highly doped graphene. This suggests that the best route to improved spectral sensitivity without loss of responsivity is to increase the mobility in graphene. Increased mobility means increased scattering time  $\tau$  which determines the width of both the Drude response and plasmon resonance, achieving a high quality factor  $Q = \omega_p \tau$  and large separation between Drude and plasmon responses. Furthermore, since the DC conductivity of graphene is  $\sigma_0 = ne\mu$ , high-mobility graphene would enable a strong plasmon resonance peak (which is proportional to the dc conductivity of the graphene sheet), making it possible to achieve very high absorption (on order unity) for highly conducting graphene (conductivity on order of the impedance of free space) at a plasmon resonance in the THz. This is almost impossible to achieve in THz with low-mobility graphene by using Drude absorption, since it requires low mobility to push the Drude response into THz, but simultaneously high conductivity.

In this chapter I also demonstrated that excitation of the standing wave plasmon in graphene ribbons also strongly depends on the boundary condition. In particular the lowest finite-frequency mode for metal-terminated graphene ribbons is the second harmonic mode which has currents antisymmetric about a node in the middle of the ribbon. In principle, other higher-order modes are possible in a two-dimensional electron channel with metallic boundaries as for example reported in Ref. [134, 135].



These modes are not observed (for example, the symmetric  $N = 3$  second mode [135]) in the experiment, possibly because (1) the integral  $\int \vec{j} \cdot \vec{E}$  is still small even for the symmetric mode, which reduces the coupling, and/or (2) the quality factor is simply too low to observe the weaker mode over the Drude response. However, it may be possible to use local gates to tailor the carrier density in regions of the device (for example, creating a  $pn$ -junction) such that  $\int \vec{j} \cdot \vec{E} \neq 0$  and light is coupled to the device even for an antisymmetric mode.

At the end of this chapter, I compare the responsivity and NEP of the large-area device to a single-element detector. The large-area device introduced in this chapter can be regarded as an  $n \times n$  array of single-element detectors: Each row of the array consists of  $n$  elements connected in parallel between metal electrodes and then  $n$  rows are connected in series to form the large-area device. I assume the resistance of each single-element detector is  $R_1$  and the photovoltage generated due to the incident radiation is  $V_1$ . Now I consider the array device: Suppose the power intensity of the excitation is kept as a constant, then the photovoltage from each element is still  $V_1$ . Since there are  $n$  rows connected in series, the total signal equals  $nV_1$ . The absorbed power is  $n^2$  times larger. Therefore, the photovoltage responsivity of the large-area device is  $n$  times less than the single-element detector. As about the NEP, since the resistance of the  $n \times n$  array ( $n \times 1/n \times R_1 = R_1$ ) is the same as a single element, the Johnson-Nyquist noise remains unchanged, thus, the NEP of the large-area device is  $n$  times larger than the single-element detector.

According to the analysis above, the NEP of a large-area device becomes worse because the signal generated from elements connected in parallel do not add up together and the device becomes less responsive. Taking this into account, one may consider connecting all  $n \times n$  elements in series to maximize the photovoltage. In this case, the total signal equals  $n^2V_1$ , whereas the absorbed power is  $n^2$  times larger, so the photovoltage responsivity remains unchanged. However, the resistance of this

hypothetic device will be  $n^2 R_1$ , resulting in an  $n$  times larger Johnson-Nyquist noise. Therefore, the NEP is not improved. The conclusion is that the devices demonstrated here are optimized in order to both detect the transmitted THz light to obtain the attenuation directly while also measuring the electrical signal produced by THz absorption. These large-area devices are necessarily less responsive and have higher NEP than a single-element detector. To optimize detection efficiency for the radiation with a large spot size, one should consider, for example, using an antenna to couple the radiation field to a single plasmonic element.

## Chapter 8: Conclusion and outlook

### 8.1 Conclusion

In this thesis I explored the optoelectronic properties of graphene, which is a novel two dimensional atomic thick crystal. Charge carrier transport and the light-matter interaction in graphene are reviewed in first two chapters, suggesting that the hot-electron photothermoelectric effect in graphene is important, which makes graphene as a promising material for room-temperature broadband photodetection with high sensitivity and extremely fast speed. In Chapter 3 to Chapter 7 I discussed my experimental efforts to fabricate and characterize graphene based broadband photodetectors, especially for the THz detection. I summarize below three main conclusions of this thesis.

1. Dissimilar metal contacted graphene devices were fabricated using standard electron beam lithography method and the tilted angle shadow evaporation technique, in order to achieve a photodetector capable of outputting an electrical signal at uniform light illumination. The photoresponse is characterized in optical, near infrared and THz range, and is compared with the thermoelectric response generated due to Joule heating. The photothermoelectric response is confirmed to persist in a broad range of the radiation frequency. Especially in the THz range, the best device shows responsivity exceeding 10 V/W (700 V/W) at room temperature referenced to the incident (absorbed) power, implying a performance which is competitive with the best room-temperature THz detectors [14] for an optimally coupled device. Further characterization shows that there is no limit to achieve the Johnson-Nyquist noise floor in such devices, resulting in an optimized noise equivalent power less than  $1100 \text{ pW/Hz}^{1/2}$  ( $20 \text{ pW/Hz}^{1/2}$ ), which compares favorably with commercially available room temperature THz detectors [16].

2. The response time of the graphene based photodetector presented in this work is characterized by ultrafast pulsed lasers. The intrinsic response time of the device to a near infrared excitation is measured using a pulse coincidence technique taking advantage of the nonlinear nature of the photovoltage signal below  $\sim 200$  K. The intrinsic response time is experimentally determined to be 10.5 ps at 150 K, which is eight to nine orders of magnitude faster than existing technologies. The extrinsic response times of actual detectors are characterized through direct time domain photoresponse measurements, which show response times of  $\sim 30$  ps for the optical excitation and  $\sim 110$  ps for the THz excitation. The extrinsic response times are slightly larger than the intrinsic response time due to the  $RC$  relaxation in the electrical circuit and the bandwidth of the detection electronics. However these measurements show that there is no technical barrier to achieving real devices operating near the intrinsic response time of graphene set by the thermal relaxation time.
3. To further increase the sensitivity of the detector in THz range and make the detection tunable (frequency selectable), large area terahertz detectors utilizing a tunable plasmonic resonance in sub-wavelength graphene micro-ribbons on SiC(0001) are fabricated. Unfortunately, most photodetection mechanisms in graphene require closely-spaced electrical contacts, which prohibit or interfere with the plasmonic excitation by screening or reflecting the incident terahertz field. In this work, by tailoring the orientation of the graphene ribbons with respect to an array of sub-wavelength bimetallic electrodes, I achieve a condition in which the plasmonic mode can be efficiently excited by an incident wave polarized perpendicular to the electrode array, while the resulting photothermal voltage can be observed between the outermost electrodes. The detector shows an enhanced photovoltage when the plasmon resonance is tuned to match the

frequency of the incident terahertz excitation.

Conclusions 1 and 2 have been published in Ref. [129]. Conclusion 3 has been submitted for publication.

### 8.2 Future outlook

The study of the photodetection in graphene based devices has developed very rapidly in recent few years. The results shown in this work contribute both to understanding the optoelectronic properties of monolayer graphene and to the potential application of utilizing graphene for sensitive and fast room temperature broadband photodetection. As discussed in the thesis, there is still opportunity for sensitivity improvement of the devices shown in this work. Next, I will propose three new designs, which could potentially enhance the responsivity of the graphene photodetector by orders of magnitude. Some of these designs have been tested preliminarily in our group.

#### **Graphene *pn*-junction photodetector**

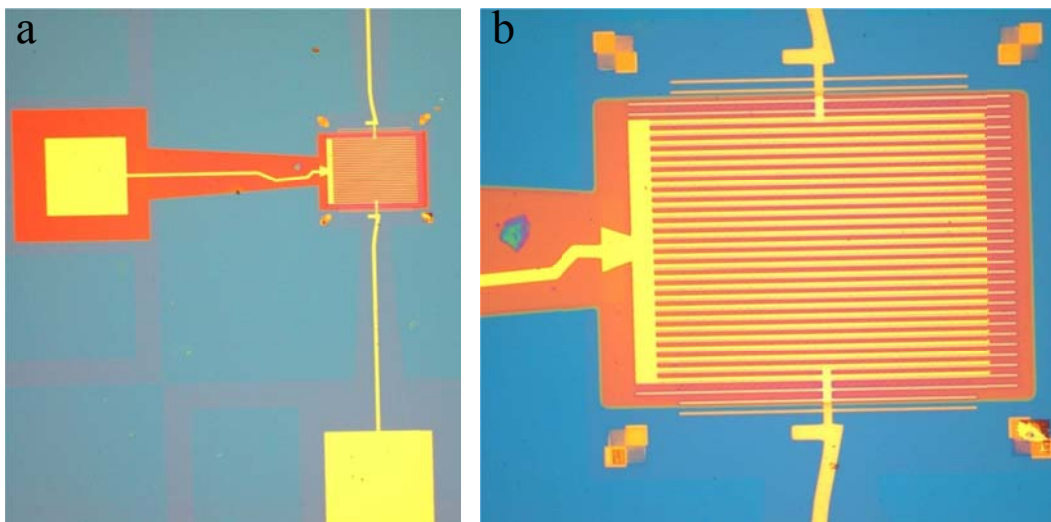


**Figure 8.1** Zoomed-out (a) and zoomed-in (b) optical micrograph of a graphene *pn*-junction photodetector.

As discussed in previous chapters, the disadvantage of a bi-metal contacted graphene detector is that only a narrow strip of the graphene flake close to the electrode contributes to the net signal due to the very symmetric temperature profile across the ribbon generated by the uniform illumination. Therefore, if a local gate can be applied to a graphene flake to tune the carrier density (thus the Seebeck coefficient) from one electrode to the center of the device, one will be able to take advantage of the whole light sensitive part to optimize the magnitude of the signal.

Fig. 8.1 shows an example of graphene *pn*-junction detector fabricated using large area CVD graphene. The light sensitive part of the device is similar to the one shown in Fig. 3.6a. Many graphene channels are connected in series with dissimilar metal contacts to enhance the response. As shown in Fig. 8.1a, the top and bottom pads (top pad not shown in the graph) serve as ground and the signal output, respectively. Then an Al<sub>2</sub>O<sub>3</sub> layer is deposited on top of the light sensitive part as the top gate dielectric, which extends to the left (red squares in Fig. 8.1a), followed by the top gate electrode evaporation. The top gate electrode is like a comb, which covers the bottom half of each graphene channel (as shown in Fig. 8.1b) to locally tune the carrier density of the channel.

I have characterized the THz photoresponse of this device in Prof. Drew's group with my colleague Dr. Sushkov. At this stage, only little improvement in sensitivity has been achieved, compared to the bi-metal contacted graphene detector. A possible reason is that the mobility of CVD graphene is low, resulting in a short diffusion length. The hot electrons generated at the center of the device are scattered by phonons before diffusing into the leads. Therefore, the effective area of the photodetector is still constrained within a narrow extension from the electrodes. Nevertheless, the idea of graphene *pn*-junction detector should work. I expect a significant improvement by using high mobility graphene samples, and I am pursuing

higher mobility graphene *pn*-junctions samples in collaboration with Prof. James Hone at Columbia University, as discussed below.

### Graphene nanoribbon photodetector

It is estimated in Chapter 2.3.2 that the thermoelectric responsivity for an ideal diffusive graphene device can be expressed as  $Responsivity = 2/\sigma E_F$ . In this case, one would expect to improve the sensitivity of the detector by solely increasing the resistivity of the graphene sheet. One way to achieve this is to etch graphene into nanoribbons. Both theory [137] and experiments [138, 139] show that the band diagram of graphene nanoribbon is different from that of two dimensional graphene sheet. A bandgap is opened in graphene nanoribbon, whose magnitude is determined by the width of the ribbon, giving a rise in the resistivity of the sample.

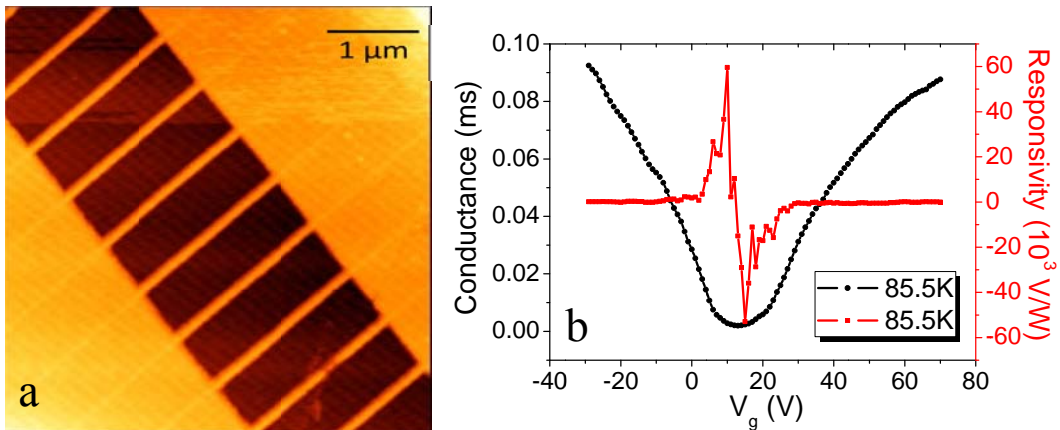


**Figure 8.2** (a) Atomic force micrograph of a graphene nanoribbon array device. (b) Conductance (black dotted line) and second harmonic responsivity (red dotted line) as a function of the gate voltage measured at  $T = 85.5$  K.

Fig. 8.2a shows the atomic force micrograph of a graphene nanoribbon array device. The yellow nanoribbon array shown in the figure is HSQ, which is a negative e-beam resist used here to pattern the graphene nanoribbon etch mask. Graphene nanoribbons are under each HSQ ribbon shown here. The ribbons are 55 nm in width and are connected with dissimilar metal electrodes on both sides in parallel. Fig. 8.2b

shows the transport characterization of this device. It is observed that the conductance of the device is close to zero in the gate range between  $V_g = 10$  V to  $V_g = 15$  V, indicating a transport bandgap of the device. The thermoelectric response of the device is characterized electrically through ac Joule heating using the second harmonic technique as introduced in previous chapters. The shape of the signal is similar to the gate dependent Seebeck coefficient of monolayer graphene. The peak responsivity appears near the charge neutral point, and the inferred responsivity exceeds 50000 V/W in this device, 2~3 orders of magnitude larger than devices shown before fabricated using 2D graphene sheet. The measurement shown in Fig. 8.2b is carried out at  $T = 85.5$  K. The transport bandgap of the device is a function of the temperature. By changing the temperature, both the resistivity and the magnitude of the second harmonic voltage change correspondingly. I have found that the peak of the second harmonic signal is linearly dependent on the resistivity of the device.

One question in this measurement is whether the second harmonic voltage accurately represents the magnitude of the thermoelectric response. As the current-voltage relationship of the bandgapped graphene nanoribbon could itself be intrinsically very nonlinear, the measured second harmonic voltage might contain artifacts due to the nonlinear effect, and not reflect the thermal response. Therefore, an optical characterization is needed to measure the real photothermoelectric signal and to calculate precisely the responsivity enhancement.

### **Ultrahigh mobility graphene plasmonic THz detector**

As discussed in the last section of Chapter 7, high quality factor of the plasmon resonance can be achieved in high mobility graphene samples due to the large scattering time, which helps to improve the spectral sensitivity of the detector in THz range. It is useful to experimentally study the plasmonic effect in graphene devices



with ultrahigh mobility, and I am collaborating with the group of Prof. James Hone at Columbia University to realize such devices.

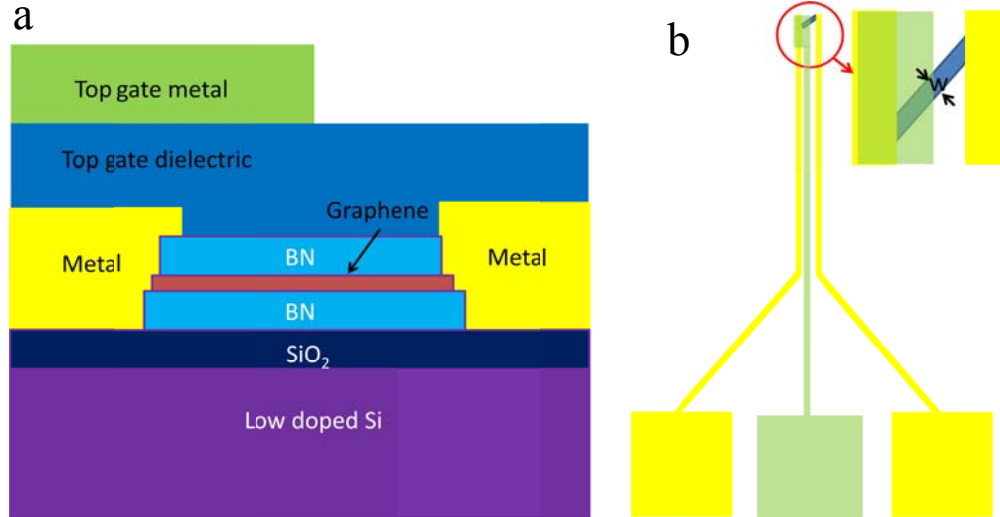








**Figure 8.3** Schematics of a graphene *pn*-junction device. (a) Side view of the device. The graphene flake is sandwiched between two boron nitride layers and connected to the metal electrodes through 1D side contacts. (b) Top view of the device. Yellow pads serve as the ground and the signal output. The green pad is connected to the top gate. The graphene flake is etched to a ribbon tilted to the electrodes.







Fig. 8.3 shows the schematics of a proposed graphene plasmonic THz detector with potentially ultrahigh mobility. An exfoliated monolayer graphene sheet is sandwiched between two thin layers of boron nitride [42] and one dimensional side contacts [140] are applied as shown in Fig. 8.3a, in order to optimize the mobility of the device. The top gate dielectric and metal are deposited to partly cover the graphene flake, so as to locally tune the carrier density of the sample, which, combined with the global back gate tuning, can make the graphene *pn*-junction having the same value of the carrier density in *p*-doped and *n*-doped region. As shown in Fig. 8.3b, the graphene flake is etched into a ribbon tilted to the metal contacts, in order to excite the plasmon mode as the incident radiation is polarized perpendicular to the electrodes. The device is designed to be symmetric, in order to reduce the pick-up noise from the background. Due to the ultrahigh carrier density of the graphene ribbon, one would expect that a plasmon enhanced photoresponse will

be observed when the carrier density of the device is tuned to match the plasmonic resonance frequency to the frequency of the incident beam.

## Appendix A: Summary of device fabrication recipes

Process	Equipment	Recipe
Alignment marker lithography	FEI XL-30 SEM 	Spin Coating: 1. MMA 2800 rpm, 60 sec 2. PMMA 3500 rpm, 50 sec Prebaking: 150°C, 8 ~ 10 min E-beam writing dosage: 190 $\mu\text{C}/\text{cm}^2$ Development: MIBK:IPA (1:3) 50 sec Rinse: IPA 30 sec
(optional) Alignment marker deposition	Thermal Evaporator 	Materials & deposition: 1. Cr: $2 \times 10^{-6}$ Torr, 4.5 nm ( $0^\circ$ tilted) 2. Au: $2 \times 10^{-6}$ Torr, 45 nm ( $0^\circ$ tilted) Lift-off: Acetone 2 hrs Rinse: Methanol (30 sec) and IPA (30 sec)
Electrode pattern lithography	FEI XL-30 SEM 	Spin Coating: 1. MMA 2800 rpm, 60 sec 2. PMMA 3500 rpm, 50 sec Prebaking: 150°C, 8 ~ 10 min E-beam writing dosage: 205 $\mu\text{C}/\text{cm}^2$ Development: MIBK:IPA (1:3) 50 sec Rinse: IPA 30 sec
Electrode metal deposition	Thermal Evaporator 	Materials & deposition: 1. Cr: $2 \times 10^{-6}$ Torr, 20 nm ( $10^\circ$ tilted) 2. Au: $2 \times 10^{-6}$ Torr, 20 nm ( $-10^\circ$ tilted) Lift-off: Acetone 4 hrs Rinse: Methanol (30 sec) and IPA (30 sec)
Graphene etch pattern lithography	FEI XL-30 SEM 	Spin Coating: 1. PMMA 2800 rpm, 60 sec 2. PMMA 3500 rpm, 50 sec Prebaking: 150°C, 8 ~ 10 min E-beam writing dosage: 190 $\mu\text{C}/\text{cm}^2$ Development: MIBK:IPA (1:3) 50 sec Rinse: IPA 30 sec
Graphene dry etching	Technics PE-II A etcher 	Chamber clean: $\text{O}_2$ ~ 300 mTorr, 300 W, 3 min Etching: $\text{O}_2$ ~ 300 mTorr, 100 W, 6 sec Remove mask: Acetone 20 min Rinse: Methanol (30 sec) and IPA (30 sec)

**Table A.1** Bi-metal contacted exfoliated graphene photodetector fabrication process

Process	Equipment	Recipe
(optional) Alignment marker lithography	FEI XL-30 SEM 	Spin Coating: 1. MMA 2800 rpm, 60 sec 2. PMMA 3500 rpm, 50 sec Prebaking: 150°C, 8 ~ 10 min E-beam writing dosage: 190 $\mu\text{C}/\text{cm}^2$ Development: MIBK:IPA (1:3) 50 sec Rinse: IPA 30 sec
(optional) Alignment marker deposition	Thermal Evaporator 	Materials & deposition: 1. Cr: $2 \times 10^{-6}$ Torr, 4.5 nm ( $0^\circ$ tilted) 2. Au: $2 \times 10^{-6}$ Torr, 45 nm ( $0^\circ$ tilted) Lift-off: Acetone 2 hrs Rinse: Methanol (30 sec) and IPA (30 sec)
Graphene* ribbon array & isolation pattern lithography	Raith e-Line 	Spin Coating: 1. PMMA 3000 rpm, 50 sec 2. PMMA 3500 rpm, 50 sec Prebaking: 150°C, 8 ~ 10 min E-beam writing dosage: 33 $\mu\text{C}/\text{cm}^2$ Development: MIBK:IPA (1:3) 45 sec Rinse: IPA 30 sec
Graphene ribbon array dry etching	Technics PE-II A etcher 	Chamber clean: $\text{O}_2$ ~ 300 mTorr, 300 W, 3 min Etching: $\text{O}_2$ ~ 300 mTorr, 100 W, 16 sec Remove mask: Acetone 20 min Rinse: Methanol (30 sec) and IPA (30 sec)
Electrode* grating lithography	FEI XL-30 SEM 	Spin Coating: 1. MMA 2800 rpm, 60 sec 2. PMMA 3500 rpm, 50 sec Prebaking: 150°C, 8 ~ 10 min E-beam writing dosage: 190 $\mu\text{C}/\text{cm}^2$ Development: MIBK:IPA (1:3) 50 sec Rinse: IPA 30 sec
Electrode** metal deposition	Thermal Evaporator 	Materials & deposition: 1. Cr: $2 \times 10^{-6}$ T, 15 ~ 20 nm ( $10^\circ$ tilted) 2. Au: $2 \times 10^{-6}$ T, 20 ~ 25 nm ( $-10^\circ$ tilted) Lift-off: Acetone 12 ~ 20 hrs Rinse: Methanol (30 sec) and IPA (30 sec)

**Table A.2** Bi-metal contacted large graphene photodetector fabrication process

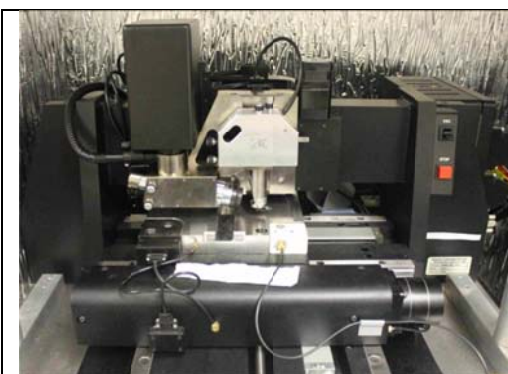
\*: Raith e-Line/FEI XL-30 SEM is used for gratings with the period below/above 4  $\mu\text{m}$ , which is generally true for graphene ribbon array/metal electrode array.

\*\* : For devices not used for the photoresponse characterization, metal electrodes were deposited like alignment markers (shadow evaporation technique not applied).

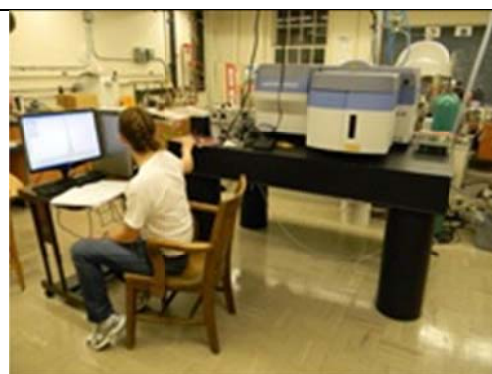
## Appendix B: Equipment list

 <p>A large, white, cylindrical spin coater with a flat top. The top surface is covered with a liquid. The side of the cylinder has several warning labels, including a high voltage symbol and text that reads "MODEL WS-400B-6NPP/LITE/IND".</p>	 <p>A laboratory workstation for a scanning electron microscope. It features a computer monitor displaying a blue screen, a keyboard, and a mouse on a white desk. In the background, the SEM instrument is visible.</p>
<p>Laurell Spin Coater (PHYS 1314)</p>	<p>FEI XL-30 SEM (PHYS 2219)</p>
 <p>A large, white, industrial-grade lithography machine with a blue vertical column. It is situated in a laboratory setting with a desk and chair nearby.</p>	 <p>A Technics PE-II A Plasma Etcher. It consists of a black control panel on the left and a main chamber with a glass viewing window on the right. The chamber has "TECHNICS PE-II A PLASMA SYSTEM" printed on it.</p>
<p>Raith e-Line (Fab lab, Kim Bldg.)</p>	<p>Technics PE-II A Etcher (PHYS 0219)</p>
 <p>A blue and white thermal evaporator. It has a large cylindrical chamber on top and a control panel with various dials and gauges on the front. It is located in a laboratory with other equipment visible in the background.</p>	 <p>An Olympus optical microscope with a black body and a white base. It has two eyepieces and a stage with a slide. The brand name "OLYMPUS" is visible on the base.</p>
<p>Thermal Evaporator (PHYS 0219)</p>	<p>Olympus Optical Microscope (PHYS 2301)</p>





DI-5000 Atomic Force Microscope  
(PHYS 2219)



HJY Raman Microscope (CHEM  
BO107)



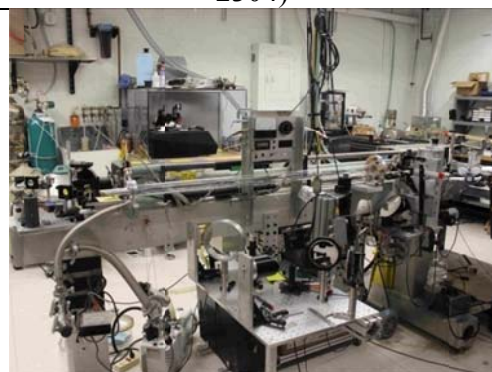
Lakeshore TT-Probe Station (PHYS  
2213)



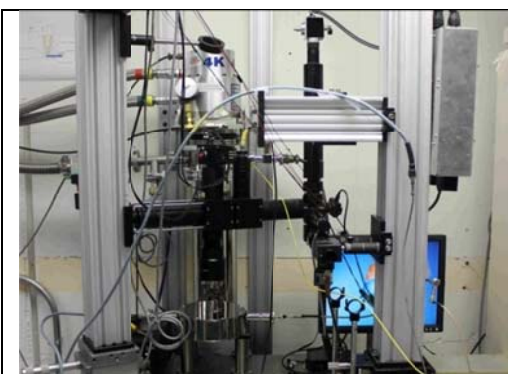
DA-8 Bomem FTIR System (PHYS  
2304)



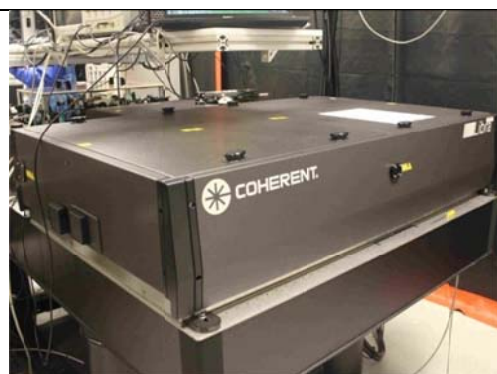
81663A Distributed Feedback Laser  
(PHYS 2304)



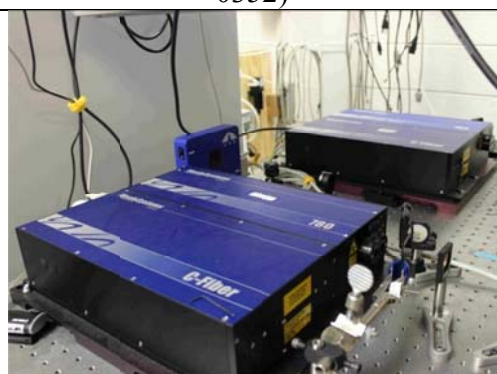
CO<sub>2</sub>-Laser Pumped Far Infrared Laser  
(PHYS 2304)



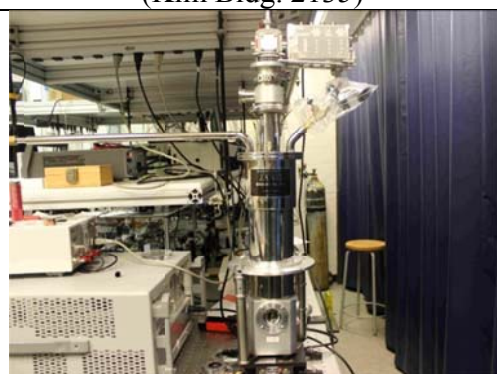
Laser Scanning Microscope (PHYS 0352)



Libra Amplified Ti: Sapphire Laser (Kim Bldg. 2135)



Menlo Systems C-Fiber 780 Fiber Lasers (ERF 0205A)



Janis Continuous Flow Cryostat System (ERF 0205A)

## Bibliography

- [1] M. Tonouchi, "Cutting-edge terahertz technology," *Nat Photon*, vol. 1, pp. 97-105, 2007.
- [2] M. Walther, B. M. Fischer, and P. Uhd Jepsen, "Noncovalent intermolecular forces in polycrystalline and amorphous saccharides in the far infrared," *Chemical Physics*, vol. 288, pp. 261-268, 2003.
- [3] N. Nagai, R. Kumazawa, and R. Fukasawa, "Direct evidence of intermolecular vibrations by THz spectroscopy," *Chemical Physics Letters*, vol. 413, pp. 495-500, 2005.
- [4] K. Kawase, Y. Ogawa, Y. Watanabe, and H. Inoue, "Non-destructive terahertz imaging of illicit drugs using spectral fingerprints," *Optics Express*, vol. 11, pp. 2549-2554, 2003.
- [5] C. Wai Lam, D. Jason, and M. M. Daniel, "Imaging with terahertz radiation," *Reports on Progress in Physics*, vol. 70, p. 1325, 2007.
- [6] W. S. Boyle and G. E. Smith, "Charge Coupled Semiconductor Devices," *Bell System Technical Journal*, vol. 49, pp. 587-593, 1970.
- [7] A. Rogalski, "Infrared detectors: status and trends," *Progress in Quantum Electronics*, vol. 27, pp. 59-210, 2003.
- [8] R. J. Keyes, P. W. Kruse, D. Long, A. F. Milton, E. H. Putley, M. C. Teich, *et al.*, "Optical and Infrared Detectors," 1980.
- [9] T. S. Moss, "Optical Properties of Semiconductors," 1959.
- [10] A. F. Gibson, M. F. Kimmitt, and A. C. Walker, "PHOTON DRAG IN GERMANIUM," *Applied Physics Letters*, vol. 17, pp. 75-77, 1970.
- [11] Electro-Optics Technology, "ET-2030-Silicon Photodetector," <http://www.eotech.com/cart/8/photodetectors/silicon-photodetectors/et-2030--silicon-photodetector>.
- [12] M. J. E. Golay, "A Pneumatic Infra - Red Detector," *Review of Scientific Instruments*, vol. 18, pp. 357-362, 1947.
- [13] D. Klocke, A. Schmitz, H. Soltner, H. Bousack, and H. Schmitz, "Infrared receptors in pyrophilous ("fire loving") insects as model for new un-cooled infrared sensors," *Beilstein Journal of Nanotechnology*, vol. 2, pp. 186-197, 2011.
- [14] F. Sizov and A. Rogalski, "THz detectors," *Progress in Quantum Electronics*, vol. 34, pp. 278-347, 2010.
- [15] J. G. Webster, "The measurement, instrumentation, and sensors handbook," pp. 32-113, 1999.
- [16] Microtech instruments, "THz detectors - Golay Cells," <http://www.mtinstruments.com/downloads/Golay%20Cell%20Datashet%20Revised.pdf>.
- [17] G. N. Gol'tsman, O. Okunev, G. Chulkova, A. Lipatov, A. Semenov, K. Smirnov, *et al.*, "Picosecond superconducting single-photon optical detector," *Applied Physics Letters*, vol. 79, pp. 705-707, 2001.
- [18] T. Damian, "Cryogenic particle detectors," *Reports on Progress in Physics*, vol. 59, p. 349, 1996.



- [19] G. Konstantatos and E. H. Sargent, "Nanostructured materials for photon detection," *Nat Nano*, vol. 5, pp. 391-400, 2010.
- [20] P. Peumans, A. Yakimov, and S. R. Forrest, "Small molecular weight organic thin-film photodetectors and solar cells," *Journal of Applied Physics*, vol. 93, pp. 3693-3723, 2003.
- [21] P. Avouris, M. Freitag, and V. Perebeinos, "Carbon-nanotube photonics and optoelectronics," *Nat Photon*, vol. 2, pp. 341-350, 2008.
- [22] M. S. Vitiello, D. Coquillat, L. Viti, D. Ercolani, F. Teppe, A. Pitanti, *et al.*, "Room-temperature terahertz detectors based on semiconductor nanowire field-effect transistors," *Nano Lett*, vol. 12, pp. 96-101, 2012.
- [23] K. S. Novoselov, A. K. Geim, S. V. Morozov, D. Jiang, Y. Zhang, S. V. Dubonos, *et al.*, "Electric Field Effect in Atomically Thin Carbon Films," *Science*, vol. 306, pp. 666-669, 2004.
- [24] K. I. Bolotin, K. J. Sikes, Z. Jiang, M. Klima, G. Fudenberg, J. Hone, *et al.*, "Ultrahigh electron mobility in suspended graphene," *Solid State Communications*, vol. 146, pp. 351-355, 2008.
- [25] A. A. Balandin, S. Ghosh, W. Bao, I. Calizo, D. Teweldebrhan, F. Miao, *et al.*, "Superior Thermal Conductivity of Single-Layer Graphene," *Nano Letters*, vol. 8, pp. 902-907, 2008.
- [26] C. Lee, X. Wei, J. W. Kysar, and J. Hone, "Measurement of the Elastic Properties and Intrinsic Strength of Monolayer Graphene," *Science*, vol. 321, pp. 385-388, 2008.
- [27] M. Engel, M. Steiner, A. Lombardo, A. C. Ferrari, H. v. Löhneysen, P. Avouris, *et al.*, "Light-matter interaction in a microcavity-controlled graphene transistor," *Nat Commun*, vol. 3, p. 906, 2012.
- [28] A. H. Castro Neto, N. M. R. Peres, K. S. Novoselov, and A. K. Geim, "The electronic properties of graphene," *Reviews of Modern Physics*, vol. 81, pp. 109-162, 2009.
- [29] S. Das Sarma, S. Adam, E. H. Hwang, and E. Rossi, "Electronic transport in two-dimensional graphene," *Reviews of Modern Physics*, vol. 83, pp. 407-470, 2011.
- [30] P. R. Wallace, "The Band Theory of Graphite," *Physical Review*, vol. 71, pp. 622-634, 1947.
- [31] M. Wilson, "Electrons in atomically thin carbon sheets behave like massless particles," *Physics Today*, vol. 59, pp. 21-23, 2006.
- [32] J.-H. Chen, C. Jang, S. Xiao, M. Ishigami, and M. S. Fuhrer, "Intrinsic and extrinsic performance limits of graphene devices on SiO<sub>2</sub>," *Nat Nano*, vol. 3, pp. 206-209, 2008.
- [33] T. Stauber, N. M. R. Peres, and F. Guinea, "Electronic transport in graphene: A semiclassical approach including midgap states," *Physical Review B*, vol. 76, p. 205423, 2007.
- [34] E. H. Hwang and S. Das Sarma, "Acoustic phonon scattering limited carrier mobility in two-dimensional extrinsic graphene," *Physical Review B*, vol. 77, p. 115449, 2008.
- [35] M. V. Fischetti, D. A. Neumayer, and E. A. Cartier, "Effective electron mobility in Si inversion layers in metal-oxide-semiconductor systems with a

- high- $\kappa$  insulator: The role of remote phonon scattering," *Journal of Applied Physics*, vol. 90, pp. 4587-4608, 2001.
- [36] S. Fratini and F. Guinea, "Substrate-limited electron dynamics in graphene," *Physical Review B*, vol. 77, p. 195415, 2008.
- [37] J. H. Chen, C. Jang, S. Adam, M. S. Fuhrer, E. D. Williams, and M. Ishigami, "Charged-impurity scattering in graphene," *Nat Phys*, vol. 4, pp. 377-381, 2008.
- [38] J.-H. Chen, W. G. Cullen, C. Jang, M. S. Fuhrer, and E. D. Williams, "Defect Scattering in Graphene," *Physical Review Letters*, vol. 102, p. 236805, 2009.
- [39] M. I. Katsnelson and A. K. Geim, *Electron scattering on microscopic corrugations in graphene* vol. 366, 2008.
- [40] J. C. Meyer, A. K. Geim, M. I. Katsnelson, K. S. Novoselov, T. J. Booth, and S. Roth, "The structure of suspended graphene sheets," *Nature*, vol. 446, pp. 60-63, 2007.
- [41] W. Bao, F. Miao, Z. Chen, H. Zhang, W. Jang, C. Dames, *et al.*, "Controlled ripple texturing of suspended graphene and ultrathin graphite membranes," *Nat Nano*, vol. 4, pp. 562-566, 2009.
- [42] C. R. Dean, A. F. Young, MericI, LeeC, WangL, SorgenfreiS, *et al.*, "Boron nitride substrates for high-quality graphene electronics," *Nat Nano*, vol. 5, pp. 722-726, 2010.
- [43] W.-K. Tse, E. H. Hwang, and S. Das Sarma, "Ballistic hot electron transport in graphene," *Applied Physics Letters*, vol. 93, p. 023128, 2008.
- [44] M. Breusing, C. Ropers, and T. Elsaesser, "Ultrafast Carrier Dynamics in Graphite," *Physical Review Letters*, vol. 102, p. 086809, 2009.
- [45] C. H. Lui, K. F. Mak, J. Shan, and T. F. Heinz, "Ultrafast Photoluminescence from Graphene," *Physical Review Letters*, vol. 105, p. 127404, 2010.
- [46] H. Wang, J. H. Strait, P. A. George, S. Shivaraman, V. B. Shields, M. Chandrashekhar, *et al.*, "Ultrafast relaxation dynamics of hot optical phonons in graphene," *Applied Physics Letters*, vol. 96, p. 081917, 2010.
- [47] P. J. Hale, S. M. Hornett, J. Moger, D. W. Horsell, and E. Hendry, "Hot phonon decay in supported and suspended exfoliated graphene," *Physical Review B*, vol. 83, p. 121404, 2011.
- [48] T. Winzer, A. Knorr, and E. Malic, "Carrier multiplication in graphene," *Nano Lett*, vol. 10, pp. 4839-43, 2010.
- [49] K. J. Tielrooij, J. C. W. Song, S. A. Jensen, A. Centeno, A. Pesquera, A. Zurutuza Elorza, *et al.*, "Photoexcitation cascade and multiple hot-carrier generation in graphene," *Nat Phys*, vol. 9, pp. 248-252, 2013.
- [50] J. Martin, N. Akerman, G. Ulbricht, T. Lohmann, J. H. Smet, K. von Klitzing, *et al.*, "Observation of electron-hole puddles in graphene using a scanning single-electron transistor," *Nat Phys*, vol. 4, pp. 144-148, 2008.
- [51] D. Kim, S. Cho, N. P. Butch, P. Syers, K. Kirshenbaum, S. Adam, *et al.*, "Surface conduction of topological Dirac electrons in bulk insulating Bi<sub>2</sub>Se<sub>3</sub>," *Nat Phys*, vol. 8, pp. 459-463, 2012.
- [52] T. Ando, Y. Zheng, and H. Suzuura, "Dynamical Conductivity and Zero-Mode Anomaly in Honeycomb Lattices," *Journal of the Physical Society of Japan*, vol. 71, pp. 1318-1324, 2002.

- [53] V. P. Gusynin, S. G. Sharapov, and J. P. Carbotte, "Unusual Microwave Response of Dirac Quasiparticles in Graphene," *Physical Review Letters*, vol. 96, p. 256802, 2006.
- [54] L. A. Falkovsky and S. S. Pershoguba, "Optical far-infrared properties of a graphene monolayer and multilayer," *Physical Review B*, vol. 76, p. 153410, 2007.
- [55] A. B. Kuzmenko, E. van Heumen, F. Carbone, and D. van der Marel, "Universal Optical Conductance of Graphite," *Physical Review Letters*, vol. 100, p. 117401, 2008.
- [56] R. R. Nair, P. Blake, A. N. Grigorenko, K. S. Novoselov, T. J. Booth, T. Stauber, *et al.*, "Fine Structure Constant Defines Visual Transparency of Graphene," *Science*, vol. 320, pp. 1308-1308, 2008.
- [57] S. Wu, S. G. Kaplan, H. T. S. Lihn, H. D. Drew, S. Y. Hou, J. M. Phillips, *et al.*, "Temperature dependence of the far-infrared magnetotransmission of  $\text{YBa}_2\text{Cu}_3\text{O}_{7-\delta}$  films," *Physical Review B*, vol. 54, pp. 13343-13347, 1996.
- [58] F. Wang, Y. Zhang, C. Tian, C. Girit, A. Zettl, M. Crommie, *et al.*, "Gate-Variable Optical Transitions in Graphene," *Science*, vol. 320, pp. 206-209, 2008.
- [59] K. F. Mak, L. Ju, F. Wang, and T. F. Heinz, "Optical spectroscopy of graphene: From the far infrared to the ultraviolet," *Solid State Communications*, vol. 152, pp. 1341-1349, 2012.
- [60] N. W. Ashcroft and N. D. Mermin, "Solid State Physics," p. 11, 1976.
- [61] J. Horng, C.-F. Chen, B. Geng, C. Girit, Y. Zhang, Z. Hao, *et al.*, "Drude conductivity of Dirac fermions in graphene," *Physical Review B*, vol. 83, p. 165113, 2011.
- [62] N. M. R. Peres, "Colloquium: The transport properties of graphene: An introduction," *Reviews of Modern Physics*, vol. 82, pp. 2673-2700, 2010.
- [63] N. M. R. Peres, T. Stauber, and A. H. C. Neto, "The infrared conductivity of graphene on top of silicon oxide," *EPL (Europhysics Letters)*, vol. 84, p. 38002, 2008.
- [64] Z. Q. Li, E. A. Henriksen, Z. Jiang, Z. Hao, M. C. Martin, P. Kim, *et al.*, "Dirac charge dynamics in graphene by infrared spectroscopy," *Nat Phys*, vol. 4, pp. 532-535, 2008.
- [65] T. W. Ebbesen, H. J. Lezec, H. F. Ghaemi, T. Thio, and P. A. Wolff, "Extraordinary optical transmission through sub-wavelength hole arrays," *Nature*, vol. 391, pp. 667-669, 1998.
- [66] R. F. Oulton, V. J. Sorger, T. Zentgraf, R.-M. Ma, C. Gladden, L. Dai, *et al.*, "Plasmon lasers at deep subwavelength scale," *Nature*, vol. 461, pp. 629-632, 2009.
- [67] K. H. Su, Q. H. Wei, X. Zhang, J. J. Mock, D. R. Smith, and S. Schultz, "Interparticle Coupling Effects on Plasmon Resonances of Nanogold Particles," *Nano Letters*, vol. 3, pp. 1087-1090, 2003.
- [68] L. Ju, B. Geng, J. Horng, C. Girit, M. Martin, Z. Hao, *et al.*, "Graphene plasmonics for tunable terahertz metamaterials," *Nat Nanotechnol*, vol. 6, pp. 630-634, 2011.

- [69] H. Yan, T. Low, W. Zhu, Y. Wu, M. Freitag, X. Li, *et al.*, "Damping pathways of mid-infrared plasmons in graphene nanostructures," *Nat Photon*, vol. 7, pp. 394-399, 2013.
- [70] E. H. Hwang and S. Das Sarma, "Dielectric function, screening, and plasmons in two-dimensional graphene," *Physical Review B*, vol. 75, 2007.
- [71] F. Rana, "Graphene Terahertz Plasmon Oscillators," *Nanotechnology, IEEE Transactions on*, vol. 7, pp. 91-99, 2008.
- [72] R. P. Leavitt and J. W. Little, "Absorption and emission of radiation by plasmons in two-dimensional electron-gas disks," *Physical Review B*, vol. 34, pp. 2450-2457, 1986.
- [73] H. Yan, X. Li, B. Chandra, G. Tulevski, Y. Wu, M. Freitag, *et al.*, "Tunable infrared plasmonic devices using graphene/insulator stacks," *Nat Nano*, vol. 7, pp. 330-334, 2012.
- [74] T. Ando, "Electronic properties of two-dimensional systems," *Reviews of Modern Physics*, vol. 54, pp. 437-672, 1982.
- [75] J. H. Lee Eduardo, K. Balasubramanian, R. T. Weitz, M. Burghard, and K. Kern, "Contact and edge effects in graphene devices," *Nat Nano*, vol. 3, pp. 486-490, 2008.
- [76] J. Park, Y. H. Ahn, and C. Ruiz-Vargas, "Imaging of Photocurrent Generation and Collection in Single-Layer Graphene," *Nano Letters*, vol. 9, pp. 1742-1746, 2009.
- [77] F. Xia, T. Mueller, R. Golizadeh-Mojarad, M. Freitag, Y.-m. Lin, J. Tsang, *et al.*, "Photocurrent Imaging and Efficient Photon Detection in a Graphene Transistor," *Nano Letters*, vol. 9, pp. 1039-1044, 2009.
- [78] J. R. Williams, L. DiCarlo, and C. M. Marcus, "Quantum Hall Effect in a Gate-Controlled p-n Junction of Graphene," *Science*, vol. 317, pp. 638-641, 2007.
- [79] M. Freitag, T. Low, F. Xia, and P. Avouris, "Photoconductivity of biased graphene," *Nat Photon*, vol. 7, pp. 53-59, 2013.
- [80] F. Rana, "Electron-hole generation and recombination rates for Coulomb scattering in graphene," *Physical Review B*, vol. 76, p. 155431, 2007.
- [81] F. Rana, P. A. George, J. H. Strait, J. Dawlaty, S. Shivaraman, M. Chandrashekar, *et al.*, "Carrier recombination and generation rates for intravalley and intervalley phonon scattering in graphene," *Physical Review B*, vol. 79, p. 115447, 2009.
- [82] X. Xu, N. M. Gabor, J. S. Alden, A. M. van der Zande, and P. L. McEuen, "Photo-thermoelectric effect at a graphene interface junction," *Nano Lett*, vol. 10, pp. 562-6, 2010.
- [83] J. C. Song, M. S. Rudner, C. M. Marcus, and L. S. Levitov, "Hot carrier transport and photocurrent response in graphene," *Nano Lett*, vol. 11, pp. 4688-92, 2011.
- [84] P. K. Herring, A. L. Hsu, N. M. Gabor, Y. C. Shin, J. Kong, T. Palacios, *et al.*, "Photoresponse of an electrically tunable ambipolar graphene infrared thermocouple," *Nano Lett*, vol. 14, pp. 901-7, 2014.
- [85] T. J. Echtermeyer, P. S. Nene, M. Trushin, R. V. Gorbachev, A. L. Eiden, S. Milana, *et al.*, "Photothermoelectric and photoelectric contributions to light

- detection in metal-graphene-metal photodetectors," *Nano Lett*, vol. 14, pp. 3733-42, 2014.
- [86] Y. Zuev, W. Chang, and P. Kim, "Thermoelectric and Magnetothermoelectric Transport Measurements of Graphene," *Physical Review Letters*, vol. 102, 2009.
- [87] P. Wei, W. Bao, Y. Pu, C. Lau, and J. Shi, "Anomalous Thermoelectric Transport of Dirac Particles in Graphene," *Physical Review Letters*, vol. 102, 2009.
- [88] S. Adam, E. H. Hwang, V. M. Galitski, and S. Das Sarma, "A self-consistent theory for graphene transport," *Proceedings of the National Academy of Sciences*, vol. 104, pp. 18392-18397, November 20, 2007.
- [89] T. Low, V. Perebeinos, R. Kim, M. Freitag, and P. Avouris, "Cooling of photoexcited carriers in graphene by internal and substrate phonons," *Physical Review B*, vol. 86, p. 045413, 2012.
- [90] J. K. Viljas and T. T. Heikkilä, "Electron-phonon heat transfer in monolayer and bilayer graphene," *Physical Review B*, vol. 81, p. 245404, 2010.
- [91] J. C. W. Song, M. Y. Reizer, and L. S. Levitov, "Disorder-Assisted Electron-Phonon Scattering and Cooling Pathways in Graphene," *Physical Review Letters*, vol. 109, p. 106602, 2012.
- [92] M. W. Graham, S.-F. Shi, D. C. Ralph, J. Park, and P. L. McEuen, "Photocurrent measurements of supercollision cooling in graphene," *Nat Phys*, vol. 9, pp. 103-108, 2013.
- [93] Q. Ma, N. M. Gabor, T. I. Andersen, N. L. Nair, K. Watanabe, T. Taniguchi, *et al.*, "Competing Channels for Hot-Electron Cooling in Graphene," *Physical Review Letters*, vol. 112, p. 247401, 2014.
- [94] J. Yan, M. H. Kim, J. A. Elle, A. B. Sushkov, G. S. Jenkins, H. M. Milchberg, *et al.*, "Dual-gated bilayer graphene hot-electron bolometer," *Nat Nano*, vol. 7, pp. 472-478, 2012.
- [95] J. B. Oostinga, H. B. Heersche, X. Liu, A. F. Morpurgo, and L. M. K. Vandersypen, "Gate-induced insulating state in bilayer graphene devices," *Nat Mater*, vol. 7, pp. 151-157, 2008.
- [96] Q. Han, T. Gao, R. Zhang, Y. Chen, J. Chen, G. Liu, *et al.*, "Highly sensitive hot electron bolometer based on disordered graphene," *Sci. Rep.*, vol. 3, 2013.
- [97] K. S. Novoselov, A. K. Geim, S. V. Morozov, D. Jiang, M. I. Katsnelson, I. V. Grigorieva, *et al.*, "Two-dimensional gas of massless Dirac fermions in graphene," *Nature*, vol. 438, pp. 197-200, 2005.
- [98] A. C. Ferrari, J. C. Meyer, V. Scardaci, C. Casiraghi, M. Lazzeri, F. Mauri, *et al.*, "Raman Spectrum of Graphene and Graphene Layers," *Physical Review Letters*, vol. 97, p. 187401, 2006.
- [99] X. Li, W. Cai, J. An, S. Kim, J. Nah, D. Yang, *et al.*, "Large-Area Synthesis of High-Quality and Uniform Graphene Films on Copper Foils," *Science*, vol. 324, pp. 1312-1314, June 5, 2009.
- [100] X. Li, Y. Zhu, W. Cai, M. Borysiak, B. Han, D. Chen, *et al.*, "Transfer of large-area graphene films for high-performance transparent conductive electrodes," *Nano Lett*, vol. 9, pp. 4359-63, 2009.

- [101] L. O. Nyakiti, V. D. Wheeler, N. Y. Garces, R. L. Myers-Ward, C. R. J. Eddy, and D. K. Gaskill, "Enabling graphene-based technologies: Toward wafer-scale production of epitaxial graphene," *MRS Bulletin*, vol. 37, pp. 1149-1157, 2012.
- [102] J. Röhrl, M. Hundhausen, K. V. Emtsev, T. Seyller, R. Graupner, and L. Ley, "Raman spectra of epitaxial graphene on SiC(0001)," *Applied Physics Letters*, vol. 92, p. 201918, 2008.
- [103] Z. H. Ni, W. Chen, X. F. Fan, J. L. Kuo, T. Yu, A. T. S. Wee, *et al.*, "Raman spectroscopy of epitaxial graphene on a SiC substrate," *Physical Review B*, vol. 77, p. 115416, 2008.
- [104] D. S. Lee, C. Riedl, B. Krauss, K. von Klitzing, U. Starke, and J. H. Smet, "Raman spectra of epitaxial graphene on SiC and of epitaxial graphene transferred to SiO<sub>2</sub>," *Nano Lett.*, vol. 8, pp. 4320-5, 2008.
- [105] J. Niemeyer and V. Kose, "Observation of large dc supercurrents at nonzero voltages in Josephson tunnel junctions," *Applied Physics Letters*, vol. 29, pp. 380-382, 1976.
- [106] A. Bartels, R. Cerna, C. Kistner, A. Thoma, F. Hudert, C. Janke, *et al.*, "Ultrafast time-domain spectroscopy based on high-speed asynchronous optical sampling," *Review of Scientific Instruments*, vol. 78, p. 035107, 2007.
- [107] J. Hebling, K.-L. Yeh, M. C. Hoffmann, B. Bartal, and K. A. Nelson, "Generation of high-power terahertz pulses by tilted-pulse-front excitation and their application possibilities," *Journal of the Optical Society of America B*, vol. 25, pp. B6-B19, 2008.
- [108] B. G. Ghamsari, J. Tosado, M. Yamamoto, M. S. Fuhrer, and S. M. Anlage, "Determination of the Optical Index for Few-Layer Graphene by Reflectivity Spectroscopy," *arXiv*, vol. 1210.0575, 2012.
- [109] P. Griffiths, "Fourier Transform Infrared Spectroscopy," 2007.
- [110] K. C. Fong and K. C. Schwab, "Ultrasensitive and Wide-Bandwidth Thermal Measurements of Graphene at Low Temperatures," *Physical Review X*, vol. 2, p. 031006, 2012.
- [111] N. M. Gabor, J. C. W. Song, Q. Ma, N. L. Nair, T. Taychatanapat, K. Watanabe, *et al.*, "Hot Carrier-Assisted Intrinsic Photoresponse in Graphene," *Science*, vol. 334, pp. 648-652, November 4, 2011.
- [112] P. L. Richards, "Bolometers for infrared and millimeter waves," *Journal of Applied Physics*, vol. 76, pp. 1-24, 1994.
- [113] E. Hecht and A. Zajac, "Optics," 1979.
- [114] C. D. Motchenbacher and J. A. Connelly, "Low-noise electronic system design," 1993.
- [115] P. A. Khomyakov, A. A. Starikov, G. Brocks, and P. J. Kelly, "Nonlinear screening of charges induced in graphene by metal contacts," *Physical Review B*, vol. 82, p. 115437, 2010.
- [116] B. Huard, N. Stander, J. A. Sulpizio, and D. Goldhaber-Gordon, "Evidence of the role of contacts on the observed electron-hole asymmetry in graphene," *Physical Review B*, vol. 78, p. 121402, 2008.

- [117] M. Liu, X. Yin, E. Ulin-Avila, B. Geng, T. Zentgraf, L. Ju, *et al.*, "A graphene-based broadband optical modulator," *Nature*, vol. 474, pp. 64-7, 2011.
- [118] T. Mueller, F. Xia, and P. Avouris, "Graphene photodetectors for high-speed optical communications," *Nature Photonics*, vol. 4, pp. 297-301, 2010.
- [119] M. Freitag, T. Low, and P. Avouris, "Increased Responsivity of Suspended Graphene Photodetectors," *Nano Letters*, vol. 13, pp. 1644-1648, 2013.
- [120] D. Spirito, D. Coquillat, S. L. De Bonis, A. Lombardo, M. Bruna, A. C. Ferrari, *et al.*, "High performance bilayer-graphene terahertz detectors," *Applied Physics Letters*, vol. 104, p. 061111, 2014.
- [121] M. Mittendorff, S. Winnerl, J. Kamann, J. Eroms, D. Weiss, H. Schneider, *et al.*, "Ultrafast graphene-based broadband THz detector," *Applied Physics Letters*, vol. 103, p. 021113, 2013.
- [122] A. V. Muraviev, S. L. Romyantsev, G. Liu, A. A. Balandin, W. Knap, and M. S. Shur, "Plasmonic and bolometric terahertz detection by graphene field-effect transistor," *Applied Physics Letters*, vol. 103, p. 181114, 2013.
- [123] V. G. Bozhkov, "Semiconductor Detectors, Mixers, and Frequency Multipliers for the Terahertz Band," *Radiophysics and Quantum Electronics*, vol. 46, pp. 631-656, 2003.
- [124] F. Klappenberger, A. A. Ignatov, S. Winnerl, E. Schomburg, W. Wegscheider, K. F. Renk, *et al.*, "Broadband semiconductor superlattice detector for THz radiation," *Applied Physics Letters*, vol. 78, pp. 1673-1675, 2001.
- [125] S. Preu, M. Mittendorff, S. Winnerl, H. Lu, A. C. Gossard, and H. B. Weber, "Ultra-fast transistor-based detectors for precise timing of near infrared and THz signals," *Optics Express*, vol. 21, pp. 17941-17950, 2013.
- [126] L. Vicarelli, M. S. Vitiello, D. Coquillat, A. Lombardo, A. C. Ferrari, W. Knap, *et al.*, "Graphene field-effect transistors as room-temperature terahertz detectors," *Nat Mater*, vol. 11, pp. 865-871, 2012.
- [127] A. D. Rakic, A. B. Djurusic, J. M. Elazar, and M. L. Majewski, "Optical properties of metallic films for vertical-cavity optoelectronic devices," *Applied Optics*, vol. 37, pp. 5271-5283, 1998.
- [128] M. Furchi, A. Urich, A. Pospischil, G. Lilley, K. Unterrainer, H. Detz, *et al.*, "Microcavity-Integrated Graphene Photodetector," *Nano Letters*, vol. 12, pp. 2773-2777, 2012.
- [129] X. Cai, A. B. Sushkov, R. J. Suess, M. M. Jadidi, G. S. Jenkins, L. O. Nyakiti, *et al.*, "Sensitive room-temperature terahertz detection via the photothermoelectric effect in graphene," *Nat Nano*, vol. 9, pp. 814-819, 2014.
- [130] D. N. Basov, M. M. Fogler, A. Lanzara, F. Wang, and Y. Zhang, "Colloquium: Graphene spectroscopy," *Reviews of Modern Physics*, vol. 86, pp. 959-994, 2014.
- [131] A. Y. Nikitin, T. Low, and L. Martin-Moreno, "Anomalous reflection phase of graphene plasmons and its influence on resonators," *Physical Review B*, vol. 90, p. 041407, 2014.
- [132] Z. Fei, G. O. Andreev, W. Bao, L. M. Zhang, S. M. A. C. Wang, *et al.*, "Infrared nanoscopy of dirac plasmons at the graphene-SiO(2) interface," *Nano Lett*, vol. 11, pp. 4701-5, 2011.

- [133] Z. Fei, A. S. Rodin, G. O. Andreev, W. Bao, A. S. McLeod, M. Wagner, *et al.*, "Gate-tuning of graphene plasmons revealed by infrared nano-imaging," *Nature*, vol. 487, pp. 82-85, 2012.
- [134] S. A. Mikhailov and N. A. Savostianova, "Influence of contacts on the microwave response of a two-dimensional electron stripe," *Physical Review B*, vol. 74, p. 045325, 2006.
- [135] A. Satou, V. Ryzhii, and A. Chaplik, "Plasma oscillations in two-dimensional electron channel with nonideally conducting side contacts," *Journal of Applied Physics*, vol. 98, p. 034502, 2005.
- [136] M. Freitag, T. Low, W. Zhu, H. Yan, F. Xia, and P. Avouris, "Photocurrent in graphene harnessed by tunable intrinsic plasmons," *Nat Commun*, vol. 4, 2013.
- [137] Y. W. Son, M. L. Cohen, and S. G. Louie, "Half-metallic graphene nanoribbons," *Nature*, vol. 444, pp. 347-9, 2006.
- [138] M. Han, B. Özyilmaz, Y. Zhang, and P. Kim, "Energy Band-Gap Engineering of Graphene Nanoribbons," *Physical Review Letters*, vol. 98, 2007.
- [139] M. Y. Han, J. C. Brant, and P. Kim, "Electron Transport in Disordered Graphene Nanoribbons," *Physical Review Letters*, vol. 104, 2010.
- [140] L. Wang, I. Meric, P. Y. Huang, Q. Gao, Y. Gao, H. Tran, *et al.*, "One-Dimensional Electrical Contact to a Two-Dimensional Material," *Science*, vol. 342, pp. 614-617, 2013.